RAM
ROBOTICS
AND
MECHATRONICS

EXPLORATIONS OF 3D PRINTED ELASTOMERIC SENSORS FOR FORCE AND POSITION MEASUREMENT

N.J. (Nina) Bhuva

MSC ASSIGNMENT

Committee:
prof. dr. ir. G.J.M. Krijnen
dr. ir. M. Schouten
dr. ir. D. Alveringh

August, 2024

058RaM2024
Robotics and Mechatronics
EEMCS
University of Twente
P.O. Box 217
7500 AE Enschede
The Netherlands

UNIVERSITY OF TWENTE. | TECHMED CENTRE
UNIVERSITY OF TWENTE. | DIGITAL SOCIETY INSTITUTE

Preface

> If you know exactly what you are going to do, what is the point of doing it?
>
> *Pablo Picasso*

This report is for everyone who was frustrated (and hopeful) for me to finish it. That includes all my friends, family, supervisors, and therapists. I am sincerely grateful to Dr. Ir. Gijs Krijnen and Dr. Ir. Martijn Schouten for being patient with me.

Martijn had been an amazing supervisor, always making me feel comfortable while he taught me about the research process and the project. I am grateful for all the guidance and all the discussions; and for being my go-to person for experiments and simulations-related information. I have learnt many perspectives on the topic from discussions with Gijs over this project's time. Just as Einstein proved time to be relative, I hope Gijs only judges this work based on its overall quality and not the amount of time and energy I was able to spend on this project. I gravitated around many spheres of developmental planes during the span of this project, and it has added unmounted value to my life's progression. Thanks to both of them, I was able to find my pace through time, space, energy, and work on this thesis.

I also want to thank Victor for telling me it was 'normal LaTeX behaviour' when I was afraid I made yet another 'Nina error' along with everything else. I am grateful to Krittika for giving me feedback on my report and for pushing me to be aspirational in life from time to time. I appreciate Minka for supervising my productive hours and for existing in my life. I am grateful to Samuel, Yuliya, and Martijn for helping me with the codes, along with Nirzary, Ishita, Sneha, Kanjashree, Aanshi, Jagrut, Anh, Vrunda, Shanti, Vitasta, Vedika, Aarjavee, Tithi, Viraj, Gabriel, Jaimil and Sabine for checking on my progress and caring about it. I also want to thank Chitvan for helping me conceptualize the narrator for my presentation and for making the poster for the invitation. I thank Ayush for bringing Big Printah to life.

I am grateful to my father for believing in me and for empowering me to pave my way in this world. Thanks to him, I have better insights into the workings of the materials used and the properties associated with them. My love for engineering is a learnt behaviour from him.

I would not have been myself if my mother wasn't who she is. She walks with me as she goes through her life- in a way that inspires me to be the kind of person I want to be.

I also appreciate my siblings for being the light of my life. I am extremely grateful for the existence of Nilay. It is my reason to keep going on bad days. Also thanks to Mira for lending me her shirt for that one meeting, and for adopting Candy and Skye. I can not imagine a world where I do not go back home to my galudiya.

I would have not been able to achieve this (or anything else) without the endless discussions I had with the late Ms Sonal Parikh. My life would have been very different if I was not introduced to Sonal Maa, and I would have probably never met myself. For this, I will forever be in debt.

I feel grateful for the constant support and strength I gained from Sarita Shah. She has been with me throughout this journey and constantly reminded me of where I place my values.

I thank all of you from the heart of my heart. I value you and appreciate your efforts. *sings Anti-Hero by Taylor Swift*

I also appreciate myself for existing, amidst everything. Commendable.

love,
Nina Bhuva

Contents

Acronyms

3DP 3D Printing. vi, 1–3, 6, 9, 11, 39, 47–49, 81, 92, 96, 97

AC Alternating Current. vi

BVOH Butenediol Vinyl Alcohol Copolymer. vi, 34, 35, 40, 41, 69, 71, 93

CAD Computer-Aided Design. vi, 34–37, 66

DC Direct Current. vi, 50

eTPU Expanded Thermoplastic Polyurethane. vi, 9, 11, 15, 16, 24, 27, 29, 35, 39–43, 92, 93, 97

FDM Fused Deposition Modeling. vi, 1, 3, 4, 6, 9, 16, 39, 40, 43, 66, 92, 94, 97

FEA Finite Element Analysis. vi, 1, 7, 23–26, 36, 59, 60, 63–67, 90, 91

FFF Fused Filament Fabrication. vi, 1, 3, 4, 6, 9, 10, 16, 39, 40, 43, 66, 92, 94

GUI Graphical User Interface. vi, 96

LCR Inductance Capacitance and Resistance meter. vi, 7, 45, 50–52

MMS Materials Management System. vi, 37

PDMS Polydimethylsiloxane. vi, 2, 3, 9, 10, 39, 97

PLA Polylactic Acid. vi, 10, 40, 41, 48, 49

PVA Polyvinyl Alcohol. vi

SLA Stereolithography. vi, 94

TPU Thermoplastic Polyurethane. vi, 6, 10, 21, 39, 43, 71, 92, 95, 97

Abstract

"If you can not measure it, you can not improve it."— Lord Kelvin

Improvements in robotic systems and diagnostic equipment for human aid, both depend on an accurate understanding of force and position. To identify mobility problems, create useful rehabilitation aids, and develop robotic prosthetics, accurate force and position sensing are critical, especially for gait analysis.

This thesis presents a step in the direction of the development and enhancement of a novel force and position sensor made with 3D Printing of elastomeric plastic. The primary focus of the research is to increase the sensitivity of capacitive and resistive sensing through the modifications like addition of extensions in the electrode layer of the capacitive sensor, as well as the addition of air gaps in the dielectric layer, using a multi-frequency readout.

The research process involved conceptualizing the design based on insights from existing studies, followed by mathematical modelling and Finite Element Analysis simulations. The models were used to understand the sensor's behaviour, and the sensor was fabricated using Fused Deposition Modeling/Fused Filament Fabrication 3D Printing techniques.

Experiments were conducted to evaluate the sensor's performance, focusing on its impedance response under varying force applications at varying positions, with multiple different frequencies simultaneously. The results indicated that the suggested design improvements have the potential to greatly enhance sensor sensitivity, especially with more research into the fabrication technique.

This thesis concludes by addressing the research objectives and proposing future work, including explorations in other fabrication methods and adding a layer of the sensor design to avoid drift in measurement, as well as segregating the sensor into smaller sections to have a better readout with the multi-frequency approach.

1 Introduction

This chapter introduces the operating principles and features of force, as well as position sensors, employed in the development of biomedical and robotic systems. Moreover, it highlights 3D printing as an upcoming technology in the field of biomedical and robotic applications. The objective of this thesis is to add sensitivity to a capacitive and resistive elastic sensor for simultaneous force-position measurements. This is elaborated further in the next part of this chapter. The organization of this thesis is detailed in the last section of this chapter.

1.1 Background

Measurement of force is vital for gauging indicators such as pressure, torque, and thrust that are needed to be derived for any mechatronic system. The position at which the force is measured gives information about the area of contact, helping to determine the structure of the object being interacted with. Force measurement has widespread applications, especially in the field of soft robotics and health monitoring using biomedical sensors. It has also seen increasing use in other fields such as remote operation, patient monitoring, prosthetic devices, and rehabilitation physical therapy [1].

Many robotic devices that are designed for monitoring and diagnostics, interact with human skin through a soft interface termed e-skin. Some of the most popular application fields that make use of e-skin technology are prosthetic limbs, wearable electronics, or medical robots for teleoperation [2, 3]. To fabricate a skin-like sensor, flexible and/or stretchable electronics featuring high resolution and rapid response rates are preferred [4]. Sanderson expresses her wonder at the positives that can be achieved by e-skin technology in the lives of volunteers (in vivo implants, [5], temporary transfer tattoos, [6]) at various clinics worldwide. Applications of e-skins now include monitoring vital signs in premature infants, hydration in athletes as well as giving robots a lighter, human-like texture. Irrespective of whether these skins are made for people or robots, they indicate a significant engineering challenge. Electronic components are typically brittle and inflexible, different from the human skin which is a malleable yet difficult canvas [7, 8].

The elasticity of electronics came to the foreground through research on conductive carbon-based polymers that could conduct electricity. These polymers were used for the development of flexible Light Emitting Diodes, Organic Field Effect Transistors, etc. The first successful research dates to the beginning of the 2000s. In 2004, Someya et al. developed a flexible 8 cm x 8 cm robot skin made from layers of pressure-sensing polyimide plastic spun into a net of individual strands. This stretched net was a successful iteration of a flexible pressure sensor that was upgraded by organic semiconductor diodes to measure temperature simultaneously, to mimic human skin. Fabricating sensitive skin with sensors in the order of thousands would require a flexible switching matrix. Present silicon-based electronics cured by Polydimethylsiloxane (PDMS) fall short of such capabilities [9]. In 2006, developments were made when submicrometre ribbons of single crystal silicon were bound to a rubber PDMS sheet, which allowed the silicon to withstand the large forces being applied to it [10]. Although many developments have been made in this area in the past decade [11–17], fabricating such sensors using 3D printing is rare [18]. 3D Printing (3DP) molds are made to cure an MEMS force sensor at [19] of the submicrometer level. Liu et al. reported the challenges of using 3D printing on piezoelectric, piezo-resistive, and capacitive characteristics for micro-scale, flexible tactile sensors [20].

3D printing has accelerated the pace of manufacturing and prototyping of flexible electronics, primarily due to the development of multi-extruder printers that are capable of printing multiple materials simultaneously [21]. This upcoming technology has various advantages, such as simplicity and flexibility in terms of design modifications and materials used [22]. In this thesis, the sensor is fabricated using Fused Deposition Modeling or Fused Filament Fabrication; melted material is extruded through a nozzle to stick to the bed or the previous layer of the object, repeating line by line, layer by layer [23]. Figure 1.1 schematically explains the working of a printer that uses the fused filament deposition technique. For such complex structures as sensors that include a combination of a few different materials, two different methods can be used to integrate different parts of the sensor. Each layer of polymer has to traditionally undergo plasma surface treatment that is lengthy and expensive. With the development of multi-extrusion systems like the one used in this project, it is possible to integrate these parts into the design. Multiple different thermoplastic filaments can be heated at temperatures higher than the melting points simultaneously and extruded using multiple nozzles, in the same print. They benefit from the high temperature of the bed to bond, thus making the fabrication process simpler than traditional techniques such as PDMS curing. Schouten mentions more about suitable technologies for 3DP sensors and different extrusion systems in his thesis and discusses the challenges present in the present material switching systems [21].

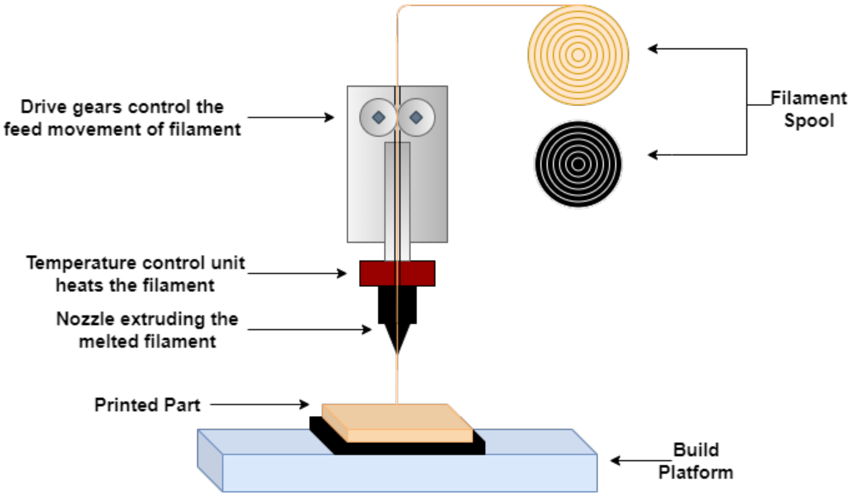

Figure 1.1: Schematic of FDM/FFF, courtesy [24].

Technology currently deployed in 3D printing soft robotic sensors has been bolstered by research in material science and 3D printing technologies. Many soft elastomer polymers, food particles as well as human tissue-based hydrogels have been used for such e-skin applications [7], Extrusion-based additive manufacturing technologies are still in the development phase for the fabrication of multi-material as well as other upcoming materials. A thorough comparison of the sustainability of materials used in extrusion-based additive manufacturing processes is presented in a detailed table within the paper [25], which evaluates various materials based on their environmental impact, resource efficiency, and overall sustainability metrics. Current limitations and future directions of such stretchable conductors and suitable materials are presented in detailed tables in paper [26] as well as in paper [27]. Conductive hydrogels are experimentally used for 3D printing and are reviewed by [28–30]. The benefits of hydrogel include its ability to preserve, replace or reinforce human tissues. They are capable of mimicking sophisticated natural architectures and imparting self-healing characteristics. Dr Agi Haines demonstrates the futuristic benefits of using new materials with 3D printing technologies using living tissues to 3D print modified skull designs to enhance human capabilities [31]. It has been showcased at many art and technology-related innovation forums, including GOGBOT, 2019 in Enschede, The Netherlands. The trend of 3D printing in alternative flexible and thin materials is also explored heavily by KRIZIA, also known as Sew Printed, which tries to print patterns with soft elastic plastic to make fabrics out of them. She made laces for her wedding dress, and it was presented as 'LACED' at Dutch Design Week in 2022 [32]. These kinds of expressions prove the versatile nature of 3D printing, redefining traditional methods creating new paradigms, and redefining normalcy [33]. Alternative materials, especially textiles, have been increasingly used as flexible pressure sensors. Lou et al. developed such a sensor with applications of plantar pressure measurement and gait analysis using a conductive textile called graphene [34]. Conductive plastics are increasingly used for electrical sensors fabricated using FDM/FFF. A review of the printing properties of commercially available conductive filaments for such medical applications is presented in [35]. In addition to textiles and plastics, Jia et al. propose the development of a capacitive, paper-based pressure sensor for gait detection [36].

Current advancements in gait and foot plantar pressure measurement are led by the company Tekscan. This includes both in-shoe and mat-like applications of capacitive force sensing, which are widely used [37, 38]. Applications like foot function analysis, gait analysis, postural stability, sway analysis, fall risk assessments, and pressure off-loading for neuropathic feet have been explored by the Centre for Biomechanics and Rehabilitation Technologies, Staffordshire University using products from Tekscan's product portfolio [39]. Out of this range of products, the most sensitive measurement tool in terms of active sensing area, an array of such Sensels (individual sensing units), and pressure range is the HR Mat 7101E. Table 1.1 provides data on the same.

Features	**Details**
Integration	VersaTek Cuff and VersaTek 2-Port Hub
Connection	USB 2.0
Number of 'Sensels'	8448
'Sensels' per 1 cm	4
Active sensing area	48.8*44.7 cm
Platform thickness	0.6 cm
Sensing platform weight	3.5 kg
Sensing range	345 to 1103 $\mathrm{kN\,m^{-2}}$

Table 1.1: Tekscan HR Mat 7101E [37]

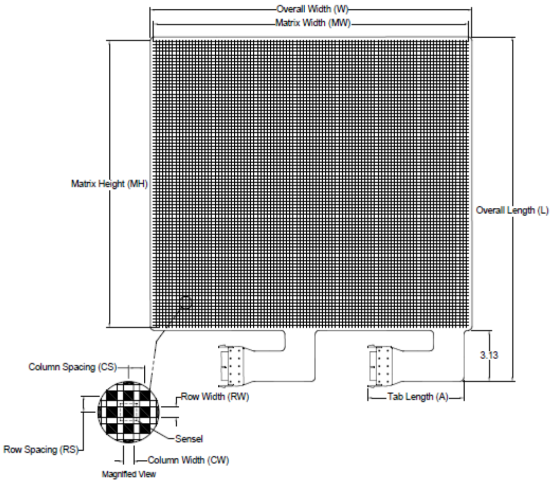

Figure 1.2: Tekscan HR Mat 7101E [37].

Many methods are used for gait and foot plantar measurements apart from such a grid of 'Sensels'. Most of them use multiple force sensors in a complex array of force and pressure sensors. Foot pressure distribution occurs due to pronation of the foot. An example of the pressure distribution of the foot during the gait cycle is shown in Figure 1.3. Key pressure points shown in Figure 1.4 have been used for medical diagnosis. Hessert et al. explore the relationship between pressure distribution during foot plantar flexion/extension and the health of the participants [40]. Many in-shoe devices have been developed to measure force at multiple such locations of the foot connected with complex circuitry, as shown in Figure 1.5 [41–46]. Various similar devices are compared and reviewed in [47] and [48]. International standards have been established for regularising plantar pressure measurement devices. The Italian public health journal published the 'International Scientific Consensus on Medical Plantar Pressure Measurement Devices: Technical Requirements and Performance' in 2012 to regulate the technology [49].

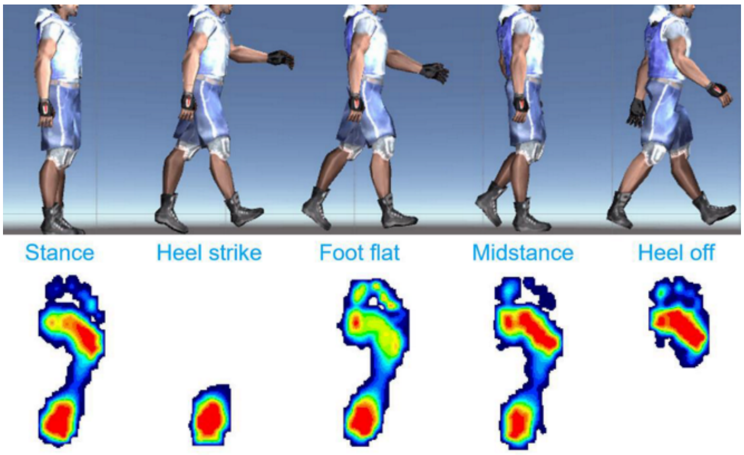

Figure 1.3: Visualisation of gait pressure distribution with different poses with reference images by commercial pressure measurement devices, [50].

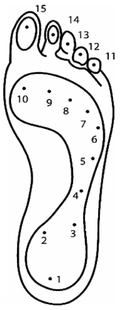

Figure 1.4: Important measurement points, [51].

The main potential advantage of using the method proposed in this report over the present technologies is the ability to use only one attachment cable and efficient computation since an infinitely large array of sensing elements of 2 mm x 2 mm can be used for similar applications using additive manufacturing exploiting conductive polymers. It meets practised standards mentioned in [49] and it is also possible to make a single sensor for all foot sizes. Its resolution and its capability to be reproduced on a larger scale make it possible for the sensor to be used for broader applications. General force measurement applications like gait analysis for animals and even machines, in addition to their usage in exoskeleton devices or as flexible touchpads, could also be beneficial.

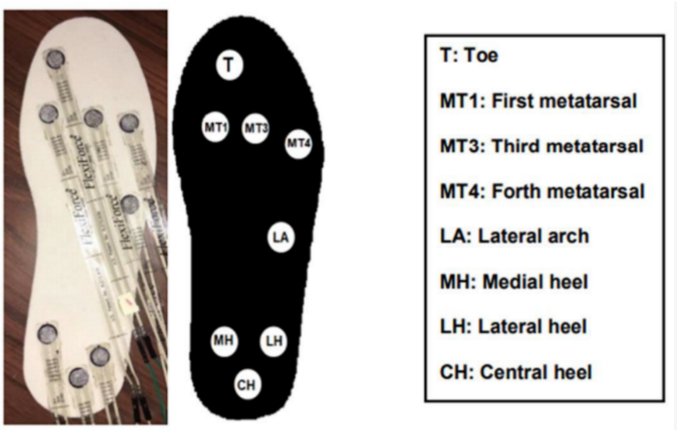

(a) Location of sensor placement, [50].

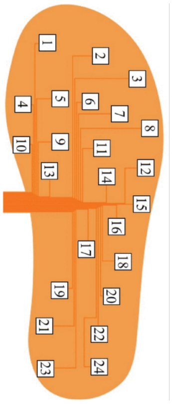

(b) High precision sensor, [52].

Figure 1.5: Different sensors used for gait analysis. (a) Fewer sensing points are used, measurement optimized using Artificial Intelligence, (b) Many sensors are connected using the Internet of Things.

1.2 Motivation

Schouten et al. developed a flexible force sensor consisting of a parallel plate capacitor [53]. It was 3DP using regular and conductive Thermoplastic Polyurethane (TPU) using FDM/FFF. This sensor is based on the change in capacitance between two flexible conductive layers of TPU and produces a capacitance change of 160 fF for a change in the force of 6.6 N.

To continue the project, Patel et al. used FDM/FFF to print TPU as a lossy transmission line [54] and one of the sensors thus designed is set as a basis for the sensor design modifications made in this assignment. Like the sensor defined above, the force applied to the sensor changes the shape of the sensor at the place of its application. Since the sensor works like a parallel plate capacitor, its resistance and capacitance change due to the displacement of the elastic structure, changing its impedance. It was possible to achieve 114 pF of capacitance change and change in resistance of 237 Ω for an applied compressive force of 11 N. This thin and elastic sensor was designed to have low complexity with only 3 electrical connections.

1.3 Research Questions

Since the umbrella goal of this project is to make an in-shoe measurement device for applications similar to gait analysis, it was interesting to optimize the sensor further. For this reason, sensitivity was added as a measure to improve the sensor's performance. After thorough research, the addition of micro-level structures to the dielectric as well as the addition of multiple frequencies for measurement was chosen to be the area of investigation. The pertinent research questions which will be answered in this thesis are:

- How does adding different micro-structures like electrode material or air gaps in the dielectric layer modify the sensitivity of force and position sensing in 3D printing of a resistive and capacitive sensor made with elastomers?
- How does multi-frequency readout affect the performance of the sensor?

1.4 Approach

For this master's thesis, engineering, and research approaches are combined, and an experimental structure is designed. This structure was tested to understand the behaviour and characteristics induced by the selected design features. Since the project is an extension of past work in this direction, most of the fabrication and model parameters are unmodified. Initially, a literature review was conducted to understand the present developments and trials in solving the problem. The mathematical model was modified to characterize the desired performance of the sensor by exploring strategies like adding air gaps or adding electrode materials in the structure of dielectrics of the sensor design. To simulate the principals in the mathematical model, Finite Element Analysis (FEA) was performed, and tested with an analytical model. An experiment was set up using a 3D printer and a force actuator. This actuator was manipulated to apply different force values at varying positions on the sensor by the 3D printer. The resistance and capacitance measurements were recorded by an LCR meter, using a multiple-frequency approach. These results are analysed and discussed.

1.5 Report Structure

This report is structured into seven chapters, each dedicated to a specific aspect of the research and development of the proposed force and position sensor design.

1.5.1 Chapter 1: Introduction

The first chapter introduces the research problem, the objectives of the project, and the significance of the proposed sensor in biomedical and robotic applications. The chapter also outlines the motivations and background information that led to the development of this project.

1.5.2 Chapter 2: Conceptual Design

Chapter 2 discusses the conceptual design of the sensor, including the inspiration derived from existing studies. The chapter elaborates on the modifications made to previous sensor designs, focusing on the feasibility of 3D printing and the introduction of a multi-frequency readout approach. It serves as a foundation for the roadmap outlined in the Future Perspectives section.

1.5.3 Chapter 3: Modelling and Design

This chapter details the mathematical modelling and Finite Element Analysis (FEA) simulations performed to understand the physics within the sensor design. It includes the development of a new sensor model in MATLAB and an analytical model in Python. The results of these simulations are used to understand the behaviour experienced by the addition of the new artefacts in the design structure, which is subsequently fabricated and tested.

1.5.4 Chapter 4: Materials and Fabrication

Chapter 4 provides an in-depth discussion of the materials used in sensor fabrication, with a focus on conductive plastics and the 3D printing process. The chapter outlines the design iterations and modifications based on material properties, such as Poisson's ratio and Young's modulus, and the challenges associated with fabricating complex designs in the sub-millimetre range.

1.5.5 Chapter 5: Experimentation

This chapter describes the experimental setup used to test the sensor prototypes. It includes a detailed explanation of the components involved, modifications made to a 3D printer for experimentation, and the methods used for data visualization and filtering. The chapter also covers the testing procedures and the comparison of results from different models and simulations.

1.5.6 Chapter 6: Results and Analysis

Chapter 6 presents and analyses the results of the new sensor design. It begins with an evaluation of the simulation outcomes, followed by a discussion of the fabrication process results and the experimental findings. The chapter examines the effectiveness of the multi-frequency approach and the impact of design modifications on sensor performance.

1.5.7 Chapter 7: Conclusions and Future Considerations

The final chapter concludes the thesis by summarizing the key findings and addressing the research questions posed in the introduction. It reflects on the achievements of the project and proposes future directions for enhancing the sensor's design and application in real-world scenarios.

2 Conceptual Design

In the first part of this chapter, some studies are introduced that inspired the designs, and later, changes to the previously fabricated sensor's mathematical model are explained. The finalization of the design was done based on its feasibility of being fabricated using 3DP, and the conceptual design was further modified for the same. A multi-frequency approach is also introduced for the readout. The goal of making these changes is to give the sensor appropriate dimensions in the later stages of the project. A road map for it is laid down in the Future Perspectives section of this report.

2.1 Modifications Explored

A force sensor is used to measure applied forces. It converts the displacement or strain of its component into a measurable change in electrical quantities such as potential, charge, current, resistance, and capacitance-converting work in the mechanical domain into an electrical signal. Most of the force sensors are fabricated by curing PDMS in moulds and using an array of capacitive cell-like structures that are connected in series, and such series are connected in parallel. Each cell forms an individual sensing unit. This mechanism was explored further, and Schouten et al. developed a flexible force sensor that was fabricated using 3DP using FDM/FFF with conductive plastics [53]. The design of this new sensor was equivalent to a capacitor, with electrodes printed using conductive Expanded Thermoplastic Polyurethane (eTPU) and dielectric printed using X60 ultra-flexible filament. On loading, the measured change in capacitance was 160 fF for 6.6 N force applied, at the operating frequency of 25 kHz.

Elongated fabricated using 3DP capacitive sensors were designed to behave like a lossy transmission line [54]. This is due to the major limitation of the 3D printing fabrication method. Fibres in organic compounds such as plastic are printed in single layers, causing anisotropic characteristics [21]. A flexible force sensor was designed and modelled based on such anisotropy for fabricated using 3DP structures that used FDM/FFF [55]. This characterization method is used by Patel in [24], which is further developed in this project, to better suit it for two-dimensional sensing.

To ensure a smooth addition of a second geometric dimension to such a sensor, an important concept to be explored is its sensitivity. In this project, different approaches are to manufacture microstructures that are either extensions of the electrode or a way of creating an air gap between the two electrodes, as explained in later parts of this chapter.

Li et al. conducted a study on techniques used to enhance the sensitivity of a given sensor [4]. These methods involve the creation of microstructures within the dielectric or electrodes, the addition of conductive fillers to polymer elastomers to form a composite dielectric, and the inclusion of micro-holes into the layer. These approaches have been explored in previous research and were reviewed in this study [4]. Quin et al. conducted a comparative analysis of five prevalent microstructures utilized in the dielectric layer of capacitive sensors, examining their impact on sensitivity, response and recovery time, cyclic stability, and pressure range. These methods are compared in Table 3 of reference [56]. Inspired by that research, modifications are explored in this project and described in the following sections.

2.2 Reference Designs

In this section, to increase the sensitivity of the previously designed sensor, two methods are explored.

2.2.1 Adding Cog-Like Structures to the Top Layer

Hao et al. conducted an investigation on various shapes for their dielectric elastomer-based capacitive pressure sensor and concluded that cubic structures were the most suitable for their application. The cubic shape enhances the sensor's ability to deform uniformly under pressure, leading to more consistent changes in capacitance and, therefore, higher sensitivity [19].

Ruth et al. examined sensors on silicon wafers, finding that specific microstructures improved performance by optimizing the contact area and deformation pattern under pressure [57, 58]. Similarly, Li et al. explored cone-like structures, discovering that varying the distances and sizes of these structures significantly affected the sensitivity. The conical shapes help focus the force, enhancing the local deformation and increasing the capacitance change [59].

Cho et al. used micro-patterned pyramidal ionic gels, which increased the sensor's flexibility and responsiveness. The pyramidal structures provided a larger surface area for deformation, improving the overall sensitivity by allowing more significant capacitance changes per unit pressure [60]. Zhang et al.'s icicle-shaped extensions on liquid-metal film electrodes created highly responsive and flexible sensors by facilitating substantial deformation, which causes more precise pressure measurements [61].

Guo et al. combined carbon nanotubes with PDMS in a composite dielectric layer, enhancing the sensor's sensitivity by leveraging the high mechanical strength and electrical conductivity of CNTs, which improved the overall deformation response [62]. Choong et al. used micro-pyramid PDMS arrays in resistive sensors to create compressible platforms, enhancing pressure sensitivity by allowing more pronounced resistance changes under pressure [63].

Luo et al. introduced a tilted micropillar array, which enhanced sensitivity by bending rather than compressing, thus increasing the effective capacitance change due to a more significant alteration in the distance between electrodes [64]. Li et al. further improved sensitivity by incorporating elastic pyramidal microstructures, which increased the sensor's responsiveness through enhanced deformation properties [59].

Mannsfeld et al. mimicked tactile sensing with flexible arrays of microstructured thin films of PDMS, enhancing sensitivity by creating a bio-inspired design that better translated mechanical stimuli into electrical signals [65]. Tee et al. made finite element models that showed that specific spatial arrangements of PDMS microstructures could maximize mechanical sensitivity by optimizing compressibility and deformation patterns [66].

Xiong et al. developed sensors with convex micro-arrays on both electrodes, finding that changes in the contact area and distance between electrodes were crucial for sensitivity. Their finite-element analysis supported that these microstructures significantly improved the sensor's performance [67]. Schwartz et al. compared different designs of PDMS pyramids, concluding that specific spacing and arrangements could dramatically enhance sensitivity by optimizing deformation behaviour under pressure [68].

The rationale behind these exotic shapes lies in their ability to optimize deformation, contact area, and distance changes under pressure, thereby significantly improving the sensitivity of capacitive force sensors. Each shape and structure introduces unique advantages, contributing to a more precise and responsive sensing capability.

2.2.2 Adding Air Gaps in the Dielectric Layer

Kim et al. found that the addition of precisely aligned air gap structures significantly improved the sensitivity of a flexible capacitive pressure sensor with porous Ecoflex, manufactured using a mould and micro-needle [69]. Stano et al. used an assembly-free multi-material Fused Filament Fabrication technique to produce a capacitive force sensor with soft TPU and soft conductive PLA. The authors examined various infill patterns in the dielectric layer to determine the effect of air gap incorporation on capacitance. The Cross 3D infill pattern was found to be the most effective in enhancing sensitivity [70]. Kwon et al. discovered that incorporating micro-pores into the dielectric layer of a flexible pressure sensor resulted in an increase in sensitivity due to the piezo-dielectric effect, and they attributed this enhancement to the impact of micro-pores on the dielectric constant and Young's modulus of the elastic dielectric, as well as due to a greater change in the distance between the electrodes [71].

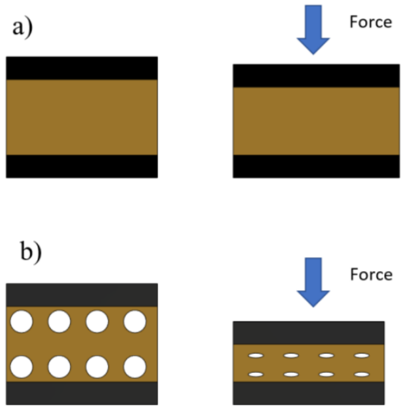

Figure 2.1: Figure from [70], comparing the difference in displacements of the top electrode for given force a) without, and b) with added air-gap to the structure.

As shown in Figure 2.1, it is intuitive to think of air gaps in the dielectric layer of a capacitive sensor to add a parallel plate capacitor to the structure without the added division of dielectric constant. Patel, in his report, also found a significant increase in the sensitivity of the sensor performance when reducing the infill density in the dielectric layer. To test the capabilities of this fabrication method, 100% infill density was used and multiple different designs were tested with different sizes and distances between air gaps. Tests were made with lower infill percentages for the dielectric to ensure an additional increase in sensitivity by reducing the infill percentage as a reliable strategy.

2.3 Considerations for Modelling

In this section, the previous work on this sensor is introduced as a starting point for modelling. Two new additions are explored based on the previously mentioned strategies, and alterations in the transmission line model are introduced for the same.

2.3.1 Previous Work

Patel [24] made a parallel plate capacitor that was fabricated using 3DP using different combinations of materials. Of all the designs that were explored in the report, the SX60 sensor design was used. It was formed by a layer of dielectric of thickness d printed using X60, sandwiched between two conductive layers of eTPU that act as electrodes for the capacitor. The sensor has connections on one of its edges, as shown in Figure 2.2 and gives information about the magnitude of force applied, as well as the position at which the force is applied along the direction of its length.

The mathematical model of the sensor can be defined by using a set of differential equations with boundary conditions, taken from Patel's MSc report. They are described in Appendix B. The RC transmission line model is used to characterize the dielectric elastomer sandwiched between electrodes. It is inspired by the field of radio and telecommunications engineering and used to analyze the effects of internal changes in the capacitance of the sensor [72–77].

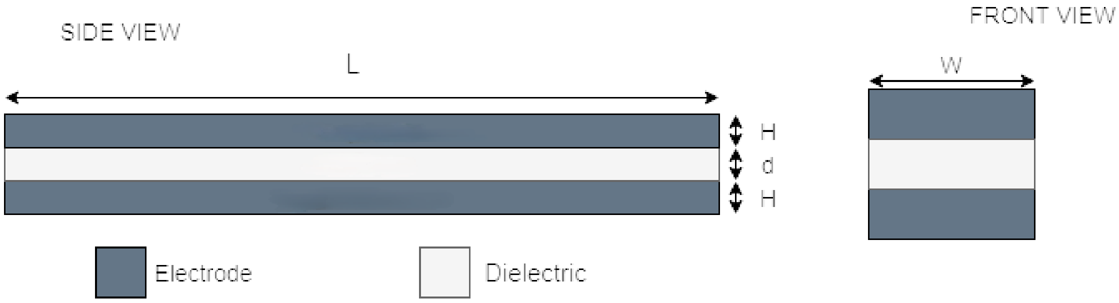

Figure 2.2: Schematic diagram of the sensor designed by Patel, reused from [24].

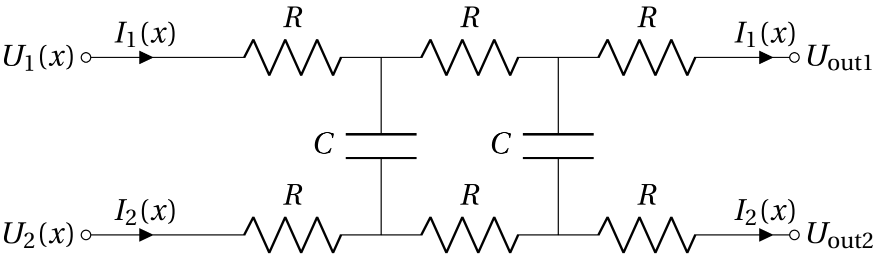

Figure 2.3: Lumped element circuit diagram of the transmission line model used by Patel [24].

The circuit diagram of such a structure would look like Figure 2.3.

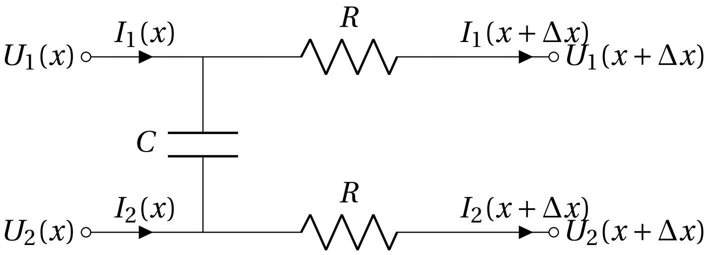

Figure 2.4: Circuit diagram for the infinitesimal part of the sensor used by Patel [24].

This model is modified by adding microstructures inspired by the literature above. For that, strategies that are explored are mentioned in the next section.

From the sensors designed by Patel in [24], the sensor design called 'SX60' was selected for making modifications. Although it exhibits disadvantages like drift and non-linearity, he demonstrates the possibility of creating a differential sensor design with two layers of the same structure stacked on top of each other to eliminate such disadvantages. This also helps in increasing its sensitivity. For adding a second geometric dimension for position measurement, the sensor needs to be more sensitive than the one referred to. To achieve this, strategies like adding a cog-like structure to the top layer and/or adding air gaps to the dielectric layer are explored. The next section visualizes the sensor's behaviour as an RC circuit for such additions to increase sensitivity and to achieve expansion of the geometric dimensions for position measurement on the sensor.

2.3.2 Adding Cog-Like Structures to the Top Electrode

The addition of an array of cog-like structures is explored here as an extension of the top layer of the sensor. These cogs can be designed as diverse as their namesake - the teeth of gears. Like in gears, these structures can be circular (like a bump), triangular (like cones), or rectangular (like teeth). Although none of the studies introduced in the previous section used the structures as an extension of the top electrode like the new proposed design intends to, they establish the importance of researching the exact shape, distance, and size of the cog-like structures.

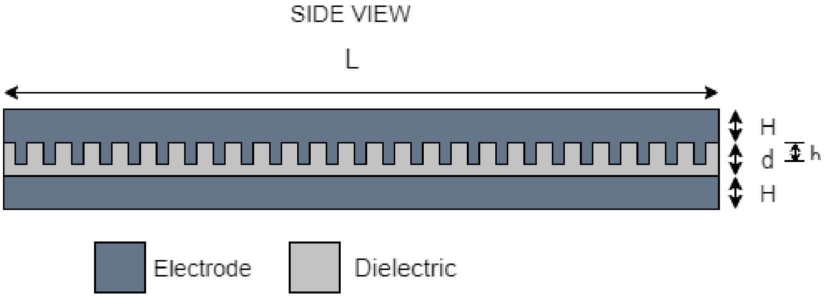

Figure 2.5: Cross section of the sensor with the extension of the top electrode with cog-like structure, and width W.

The circuit diagram of such a structure would look like Figure 2.6, using transmission line modelling.

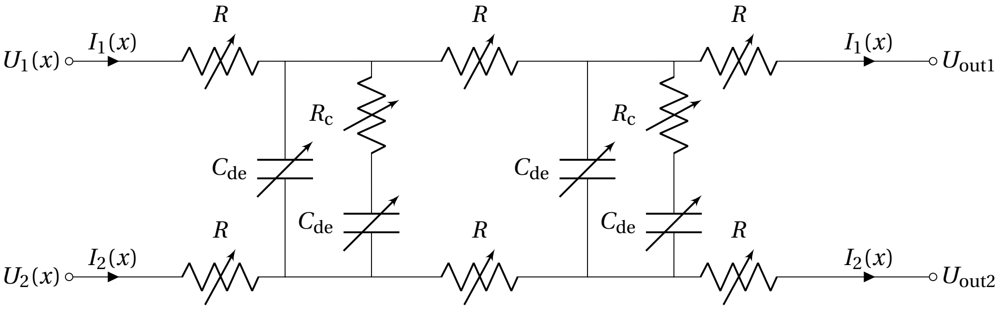

Figure 2.6: Circuit diagram for transmission line model of the structure with added cogs. The variable capacitors and resistors signify changes in resistance and capacitance values due to added force.

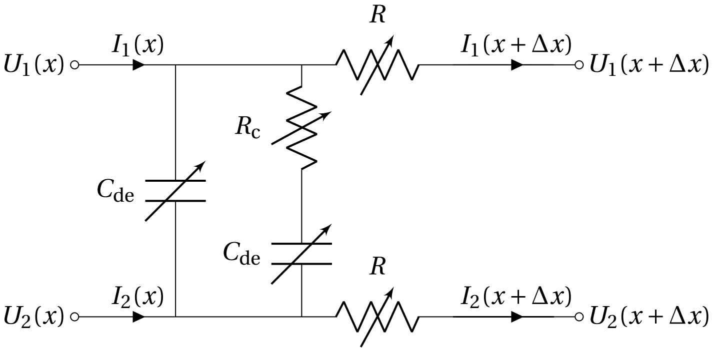

Figure 2.7: Circuit diagram for the infinitesimal part of the sensor design with added cogs.

2.3.3 Adding Air Gaps to the Structure

The dielectric shown in Figure 2.5 could be substituted with regularly spaced air gaps, as illustrated in Figure 2.8, to increase conduction at the electrodes during the application of force to the sensor.

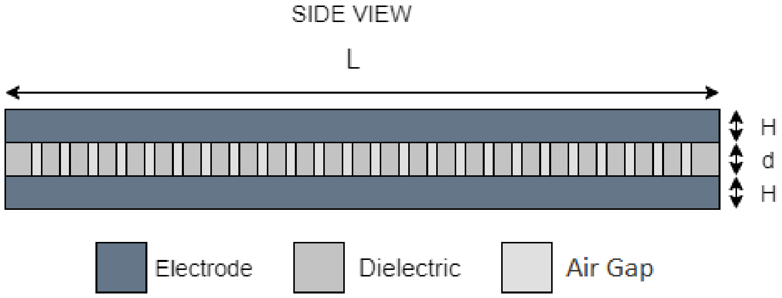

Figure 2.8: Cross section of the sensor with an air gap in the dielectric layer, with width W.

The circuit diagram of such a structure would look like Figure 2.9, using transmission line modelling.

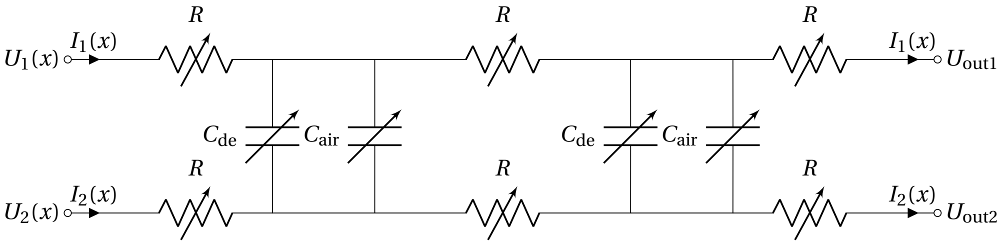

Figure 2.9: Circuit diagram for transmission line model of the structure with an added air gap in the dielectric layer.

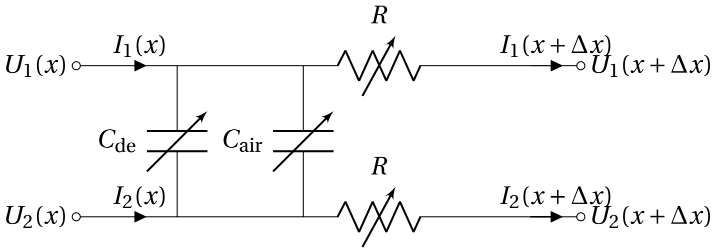

Figure 2.10: Circuit diagram for the infinitesimal part of the sensor design with an added air gap in the dielectric layer.

Since this is modelled as capacitors in parallel, the equivalent capacitance due to this circuit looks like the scalar sum of capacitance in the sensor due to the dielectric and the capacitance due to the air gap. Thus, the model in Figure 2.10 can be modelled as shown in Figure 2.11. Apart from this, the capacitance changes because of the expansion of dielectric material when external force is applied to this RC chain. An analytical model is derived in Chapter 3 to explain the effects of bulging experienced by our elastic material under force.

Adding such alterations to the structure is an advantage of additive manufacturing. Multi-extrusion for fused deposition makes it possible to design such complex structures of the sensor, without the additional steps of assembling different parts of the sensors post-printing. The

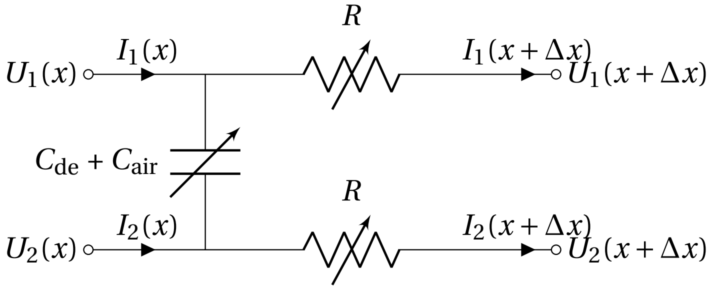

Figure 2.11: Reduced circuit diagram for the infinitesimal part of the sensor design with an added air gap.

final designs mentioned in the next section are modifications to the initial structure that the fabrication process can allow.

2.4 Proposed Designs

Both the strategies mentioned above are used in the final design, inspired by the paper by Li et al. [4]. Based on the previously described exploration, two structures, as explained below, were designed.

2.4.1 Triangular Design

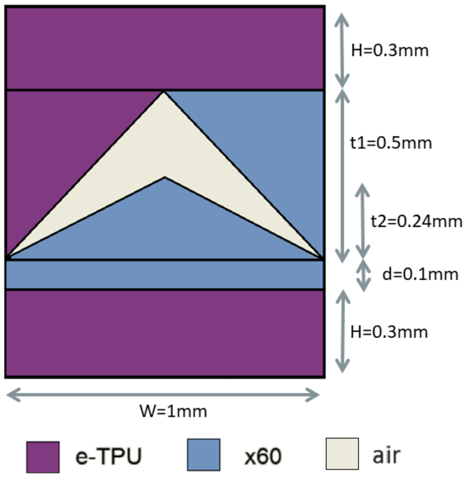

Figure 2.12: Cross-section of a unit cell of the final design with extension of electrode and air gap in the dielectric, with width W.

Keeping the volume of all the materials constant in both these structures, this cell is made with depositing lines of eTPU and X60 in 0.5*1 mm inverse triangles alternatively. The space for air was created by the gap between these and the bottom dielectric X60 triangles of 0.24*1 mm. One side of this design is shown in figure 2.12. Like in the rectangular design, the short-circuiting in the structure is avoided by introducing a layer of 0.1 mm of X60 on top of the bottom electrode. The design of the circuit for transmission line modelling of such a structure is shown in figure 2.15.

Because of the line-by-line deposition of material in FDM/FFF, the size of this air gap can be bigger. Thus, the change in sensitivity can be higher. The circuit diagram of its transmission line model is shown in figure 2.13.

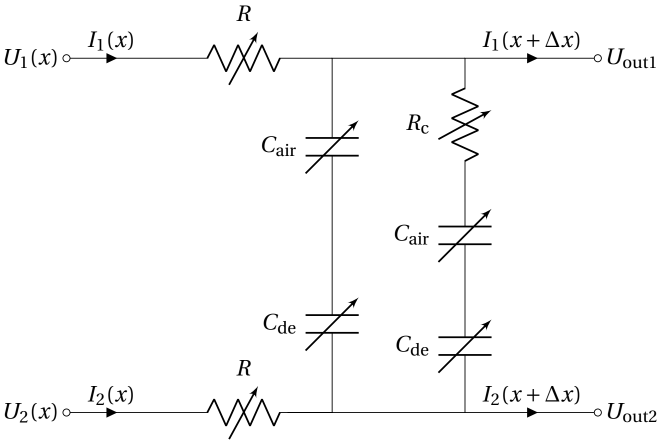

Figure 2.13: Circuit diagram for transmission line model of the final design with triangle extension of the electrode and added air gaps.

2.4.2 Rectangular Design

This cell is made with depositing lines of eTPU and X60 in 0.3 mm x 0.7 mm blocks alternatively with space of 0.3 mm x 0.3 mm between them for air, orthogonal to each other. One side of this design is shown in Figure 2.14, and the mesh denotes the repetition of the same structure transverse to the plane of this paper. This connects the extension of the top electrode to the extension in another direction, which causes the top and bottom electrodes to touch each other, causing a short circuit. To avoid this, a layer of 0.1 mm of X60 is added on top of the bottom electrode.

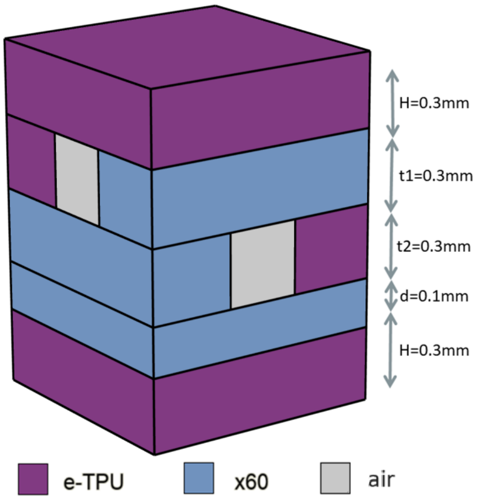

Figure 2.14: A unit cell of the final design with the extension of electrode and air gap in the dielectric. The width of this entire cell is W x W.

The dimensions of each of these components are versatile. The reason for using these specific values is explained in the next chapter. The circuit design for transmission line modelling of such a structure is shown in figure 2.15.

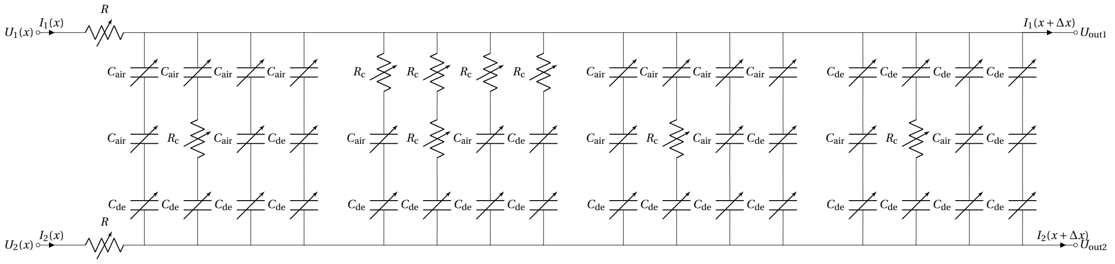

Figure 2.15: Circuit diagram for transmission line model of the final design with such a rectangular extended electrode and added air gaps.

Since all the variable components are dependent on the same parameters, it is possible to merge similar components in each parallel rung as a single variable component. Apart from this, it is also possible to merge identical rungs to further simplify the model, and assume its calculation in a single varying rung. Thus, the complex model of figure 2.15 can be reduced to a simpler version as shown in figure 2.16.

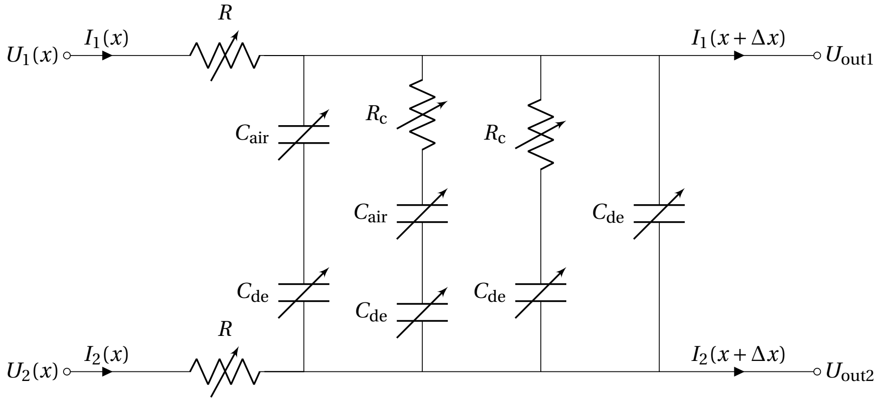

Figure 2.16: Simplified circuit diagram of the final design with the rectangular extension of the electrode and added air gaps.

The versatile nature of the components of these designs is an advantage of the fabrication process of 3D printing, It is easily possible to change the dimensions of the design parameters, such as the height, the width as well as the distance between each cog or each air gap.

2.5 Mathematical Model Calculations

The new sensor designs can be represented by their equivalent circuit diagram as a lossy transmission line, as shown in figures 2.16, and 2.13. This is similar to 2.3, reduced as 2.4, as seen in the Appendix B. We assume that the electrodes of these new sensor designs are also purely resistive [78]. Again, all the parameters are the same - the resistance of the sensor of Δx [m] width is defined as $R = \frac{\rho \Delta x}{HW}$ [Ω] and ρ [Ωm] is the volume resistivity of the electrode material. Given an infinitely small part of the sensor in figures 2.16 and 2.13, the current flows from left to right because of the potential difference in track U_1. Dimensions H, $t1$, $t2$, d, W, $w1$, $w2$, and L in these equations are taken from the sensor designs, as shown in figures 2.14, 2.12, and 2.2.

$$I_1(x,t) = \frac{\Delta U_1(x,t)}{R_n} = \frac{-HW}{\rho} \frac{\Delta U_1(x,t)}{\Delta x} \tag{2.1}$$

The limit on $\Delta x \to 0$:

$$I_1(x,t) = \frac{-HW}{\rho}\frac{\partial U_1(x,t)}{\partial x} \tag{2.2}$$

We get this equation in the time domain. Since we want impedance in the frequency domain, the Fourier transform gives us:

$$\hat{I}_1(x,\omega) = \frac{-HW}{\rho}\frac{\partial \hat{U}_1(x,\omega)}{\partial x} \tag{2.3}$$

We differentiate the equation for x to get a second-order term of voltage.

$$\frac{\partial \hat{I}_1(x,\omega)}{\partial x} = \frac{-HW}{\rho}\frac{\partial^2 \hat{U}_1(x,\omega)}{\partial x^2} \tag{2.4}$$

The capacitance in the design is due to two different structures, acting in parallel for our circuit. Thus, the resulting capacitance should be an addition of both effects. The first effect is the capacitance of the dielectric C_{de}, given by parallel plate approximation:

$$\begin{aligned} C_{\mathrm{de}} &= \frac{\varepsilon_0 \varepsilon_{\mathrm{r}} A_{\mathrm{de}}}{d_{\mathrm{de}}} \\ &= \frac{\varepsilon_0 \varepsilon_{\mathrm{r}} W_{\mathrm{de}} \Delta x_{\mathrm{de}}}{d_{\mathrm{de}}} \end{aligned} \tag{2.5}$$

with area A_{de} [mm^2] of the plates, distance between the plates d_{de}, permittivity of vacuum ε_0[F m^{-1}], and relative permittivity and ε_{r}. The area under the plate A_{de} is a scalar multiplication of the width W_{de} and the component of change in the width Δx_{de} that is added because of X60.

The reactance component because of this capacitance C_{de}, is given as:

$$\begin{aligned} X_{\mathrm{de}} &= \frac{1}{\omega C_{\mathrm{de}}} \\ &= \frac{d_{\mathrm{de}}}{\omega \varepsilon_0 \varepsilon_{\mathrm{r}} W_{\mathrm{de}} \Delta x_{\mathrm{de}}} \end{aligned} \tag{2.6}$$

The second effect is the capacitance of the air gap C_{air}, given by parallel plate approximation:

$$\begin{aligned} C_{\mathrm{air}} &= \frac{\varepsilon_0 A_{\mathrm{air}}}{d_{\mathrm{air}}} \\ &= \frac{\varepsilon_0 W_{\mathrm{air}} \Delta x_{\mathrm{air}}}{d_{\mathrm{air}}} \end{aligned} \tag{2.7}$$

with area A_{air} of the plates, distance between the plates d_{air}, permittivity of vacuum ε_0 [F m^{-1}]. It is possible to ignore the relative permittivity $\varepsilon_{\mathrm{air}}$ because we assume the relative permittivity of air to be 1. The area under the plate A_{air} is a scalar multiplication of the width W_{air} and the component of change in the width Δx_{air} that is added because of the air gap. The reactance component because of this capacitance C_{air}, is given as:

$$\begin{aligned} X_{\mathrm{air}} &= \frac{1}{\omega C_{\mathrm{air}}} \\ &= \frac{d_{\mathrm{air}}}{\omega \varepsilon_0 W_{\mathrm{air}} \Delta x_{\mathrm{air}}} \end{aligned} \tag{2.8}$$

Apart from these, we have the resistive component introduced due to the addition of the top electrode can be given as:

$$\begin{aligned} R_\mathrm{c} &= \frac{\rho d_\mathrm{c}}{A_\mathrm{c}} \\ &= \frac{\rho d_\mathrm{c}}{W_\mathrm{c}\Delta x_\mathrm{c}} \end{aligned} \tag{2.9}$$

R_c is in [Ω]. The cross-sectional area of the added cog is A_c, which is a scalar multiplication of the width W_c and the component of change in the width Δx_c that is added because of the cog. The length of this resistor is the height of the cog.

2.5.1 Triangular Design

For the rectangular design, the unit cell of the circuit shown in figure 2.12 is used. To find the equivalent impedance for this lumped model, first, we need to find impedance due to the dielectric layer artefacts in the circuit of figure 2.13. This is because of the first two rungs seen in the rectangular design, and thus is possible to compute:

These parallel impedances can be calculated as an equivalent impedance.

$$Z_\mathrm{t} = \frac{Z_1 Z_2}{Z_1 + Z_2} \tag{2.10}$$

The current passes through both these impedances Z_r and Z_t respectively (here denoted as Z), due to the potential difference between U_2 and U_1. This current $\hat{I}_\mathrm{c}$ is expressed in Fourier transform while assuming harmonic function.

$$\hat{I}_1(x+\Delta x,\omega) - \hat{I}_1(x,\omega) = -\hat{I}_c(\omega) \tag{2.11}$$

$$\hat{I}_1(x+\Delta x,\omega) - \hat{I}_1(x,\omega) = \frac{-\left(\hat{U}_2(x,\omega) - \hat{U}_1(x,\omega)\right)}{Z(\omega)} \tag{2.12}$$

For a unit part of the sensor, it is possible to derive the equation as a partial derivative.

$$\frac{\partial \hat{I}_1(x,\omega)}{\partial x} \rightarrow \frac{-HW}{\rho}\frac{\partial^2 \hat{U}_1(x,\omega)}{\partial x^2} = jZ\left(\hat{U}_1(x,\omega) - \hat{U}_2(x,\omega)\right) \tag{2.13}$$

$$\frac{\partial^2 \hat{U}_1(x,\omega)}{\partial x^2} = \frac{j\rho Z\left(\hat{U}_{2,}(x,\omega) - \hat{U}_1(x,\omega)\right)}{H} \tag{2.14}$$

Introducing the conduction parameter:

$$\Gamma = \frac{j\rho Z}{H} \tag{2.15}$$

For the top track, a second-order differential equation is given by:

$$\frac{\partial^2 \hat{U}_1(x,\omega)}{\partial x^2} - \Gamma\left(\hat{U}_2(x,\omega) - \hat{U}_1(x,\omega)\right) = 0 \tag{2.16}$$

And for the bottom track, the differential equation:

$$\frac{\partial^2 \hat{U}_2(x,\omega)}{\partial x^2} - \Gamma\left(\hat{U}_1(x,\omega) - \hat{U}_2(x,\omega)\right) = 0 \tag{2.17}$$

Using this conduction parameter Γ in equation B.18 in appendix B, and following all the steps, we get equation B.53 for the total impedance:

$$\begin{aligned} Z_{\text{total}} &= \frac{\hat{U}_1(0,\omega) - \hat{U}_2(0,\omega)}{\hat{I}_1(0,\omega)} \\ &= \frac{\sqrt{2}\rho\left(1 + e^{2\sqrt{2\Gamma}L}\right)}{H\sqrt{\Gamma}W\left(-1 + e^{2\sqrt{2\Gamma}L}\right)} \end{aligned} \tag{2.18}$$

2.5.2 Rectangular Design

For the rectangular design, the unit cell of the circuit shown in figure 2.14 is used. To find the equivalent impedance for this lumped model, first, we need to find impedance due to the dielectric layer artefacts in the circuit of figure 2.16.

In the first parallel rung, we have variable capacitance due to air as dielectric, in series with the variable capacitance due to the dielectric layer. So the impedance is a scalar sum of both these reactances.

$$\begin{aligned} Z_1 &= X_{\text{air}} + X_{\text{de}} \\ &= \frac{d_{\text{air}}}{\omega\varepsilon_0 W_{\text{air}}\Delta x_{\text{air}}} + \frac{d_{\text{de}}}{\omega\varepsilon_0\varepsilon_{\text{r}} W_{\text{de}}\Delta x_{\text{de}}} \end{aligned} \tag{2.19}$$

In the second parallel rung, a resistive part and two capacitive parts are present. To find the equivalent impedance, we add both the reactance with the resistance due to the cog+

$$\begin{aligned} Z_2 &= X_{\text{air}} + X_{\text{de}} + R_{\text{c}} \\ &= \frac{d_{\text{air}}}{\omega\varepsilon_0 W_{\text{air}}\Delta x_{\text{air}}} + \frac{d_{\text{de}}}{\omega\varepsilon_0\varepsilon_{\text{r}} W_{\text{de}}\Delta x_{\text{de}}} + \frac{\rho d_{\text{c}}}{W_{\text{c}}\Delta x_{\text{c}}} \end{aligned} \tag{2.20}$$

The impedance of the third parallel rung consists of the reactance due to the variable height of the dielectric. It can be approximated as the following.

$$\begin{aligned} Z_3 &= X_{\text{de}} \\ &= \frac{d_{\text{de}}}{\omega\varepsilon_0\varepsilon_{\text{r}} W_{\text{de}}\Delta x_{\text{de}}} \end{aligned} \tag{2.21}$$

The estimate of impedance due to the fourth rung is shown below.

$$\begin{aligned} Z_4 &= X_{\text{de}} + R_{\text{c}} \\ &= \frac{d_{\text{de}}}{\omega\varepsilon_0\varepsilon_{\text{r}} W_{\text{de}}\Delta x_{\text{de}}} + \frac{\rho d_{\text{c}}}{W_{\text{c}}\Delta x_{\text{c}}} \end{aligned} \tag{2.22}$$

These parallel impedance can be calculated as an equivalent impedance.

$$Z_{\text{r}} = \frac{Z_1 Z_2 Z_3 Z_4}{Z_1 Z_2 Z_3 + Z_2 Z_3 Z_4 + Z_1 Z_2 Z_4 + Z_1 Z_3 Z_4} \tag{2.23}$$

Finally, for both designs, this lumped impedance is divided into its real and imaginary components. The phase shift in the measurement of the impedance is characterised by this imaginary component, and denoted with a scaling of $-j$. ω is the frequency of excitation for the dielectric since the Fourier transform helps to visualize the response of the sensor.

$$\begin{aligned} Z_{\text{total}}(\omega) &= \Re\{Z(\omega)\} + j\Im\{Z(\omega)\} \\ &= R + jX \\ &= R + \frac{1}{j\omega C} \\ &= R - j\frac{1}{\omega C} \end{aligned} \tag{2.24}$$

$\Re\{Z(\omega)\}$ is the real part of the impedance, the resistance (R), and $\Im\{Z(\omega)\}$ is the imaginary part of the impedance, the reactance (X). Because of the complex nature of the polymers used in the sensor design, it is possible to assume the imaginary part of the impedance, the reactance as purely capacitive, and assume the polymers have negligible inductive components.

From the equation 2.24, the dependence of the frequency is visible on the impedance response. The reactive component is also inversely proportional to the frequency, and this effect can be used to segregate the sensor into multiple parts when simultaneous frequencies are used together. For the addition of dimension in the sensor, it is valuable to increase its sensitivity, for which the above-mentioned strategies are implemented. In the next section, a multi-frequency approach is introduced for this design.

2.6 Multi-Frequency Approach

Conduction in a mixed resistive-capacitive sensor is determined by Γ. This parameter is directly proportional to the frequency ($\Gamma \propto \omega$ and $\omega = 2\pi f$). At lower frequencies, the impedance of the circuit will be higher, due to a larger value of the capacitive reactance X_C concerning the resistance R. Thus, very little current flows through the sensor, giving a predominantly capacitive response. Similarly, at higher frequencies, the value of resistance is higher and the conduction becomes predominantly resistive. This change creates two different conduction modes that are related to the cut-off frequency f_c. For an RC low-pass filter, the theoretical cut-off frequency at (−3 dB) is experienced when the resistance's magnitude is equal to the magnitude of capacitive reactance in the circuit, given by:

$$f_c = \frac{1}{2\pi RC} \tag{2.25}$$

Since the lumped model of this sensor behaves as an RC low-pass filter, the behaviour differs at higher frequencies. It is possible to use this because of the frequency-dependent behaviour of the dielectric polymer with a complex permittivity. As seen in equation 2.24, the polymers exhibit a frequency dependence when subjected to alternating electric fields. The molecular structure of TPU is affected by the relaxation processes occurring within the material's composition since it has alternating soft and hard segments. When an external electric field is applied, these segments and dipoles undergo relaxation. It is easier for the polymer chains and the dipoles to unwind and align with the electric field when the frequency is low, improving the material's capacity to polarize, and increasing the capacitive permittivity. Thus, the electric susceptibility of the material is directly dependent on the frequency, polarizing the material. This polarization occurs by induction of dipole moments in the individual molecules, causing the rotation of molecules in the medium. Since this susceptibility in the materials fabricated in this project is not linear, anisotropic behaviour can exist, as explained later in this report. At higher frequencies, the relaxation time shortens for these segments, preventing the polymer chains and the dipoles from perfectly aligning with the changing electric field. This reduces the polarization response and thus the capacitive permittivity.

This mechanism makes it possible to use multiple different frequencies in various ranges and get easily distinguishable signals at specific points in the geometry of the 2D sensor. The addition of dimension in this way can be formed by various strategies, explained in 7.2.6.

2.7 Conclusions

This chapter introduced various research for increasing sensitivity in a force and a pressure sensor, especially the likes explored in this project. The basic concept behind the strategies used was explained in the initial sections, that is addition of a cog-like structure of the electrode layer, and the addition of air gaps in the dielectric layer. The preceding chapter introduced previous work in this project as a starting point for the modelling of the new sensor design. A transmission line model was made for the added structural changes, and the mathematical model was calculated. Finally, the principle behind the multi-frequency approach was introduced. The modelling explained in the next chapter is based on these mathematical calculations.

3 Modelling and Design

A mathematical model was created to extend the dimension from previous work using MATLAB. A model was made for the new sensor, and an inverse fit was made for it for the multi-frequency approach explained earlier. Finite Element Analysis (FEA) simulations were conducted in COMSOL multiphysics to understand the sensor mechanism and were made before designing as well as after testing the prototype. The steps taken to make the simulation are explained in this section. Further, an analytical model is derived and implemented in Python to understand the workings of these designs.

3.1 Simulation Design

Two different software are used to implement simulations: A mathematical model using MATLAB to understand the behaviour of the entire sensor and get force and position spectra at seven different frequencies, and an FEA simulation using COMSOL Multiphysics to understand the displacement and electric field variations on the structure of the sensor at different forces.

3.1.1 Mathematical Model

The parameters used to simulate the model of the sensors are calculated from the printed sensor using MATLAB, as shown in table 3.1. The impedance spectrum was modelled using seven different frequencies. The impedance is calculated as a function of the force and the position of the force applied.

Table 3.1: Sensor parameters for MATLAB

Parameter Name	**Value (electrodes, dielectric)**
Sensor length (L)	100 mm
Sensor width (W)	10 mm
Relative permittivity (ε_r)	(4.68, 5.73)
Layer height (h)	(300 µm,600 µm)
Young's modulus (E)	(22 MPa,6 MPa)
Frequencies	1.1, 2.3, 5.3, 10.1, 19.9, 49.9 and 99.7 kHz

The impedance values are calculated as a function of position and force. From previous models and experiments [24, 79], it is expected that the imaginary part of the impedance depends merely on the force applied, and the real part of the impedance depends on both—the force and the position where the force is applied.

3.1.2 FEA Simulation

To understand the multi-physics coupling between electrostatics and physical displacement due to force, Finite Element Analysis (FEA) was performed with the help of COMSOL multiphysics. For this, two different models were made, explained below. These models were made to understand the change in sensitivity because of the added structures.

For all the designs, the materials used are described in subsection 4.2. A parametric sweep is performed for forces ranging from $0\,\mathrm{kN\,m^{-2}}$ to $100\,\mathrm{kN\,m^{-2}}$ stepping at every $10\,\mathrm{kN\,m^{-2}}$. The force is applied on the top layer of the design, and in z direction, and a prescribed displacement of 0 mm is given to the bottom face of the sensor in all three directions. The top layer is given a terminal potential of 1 V and the bottom plate is given a voltage of 0 V. This potential difference creates a potential distribution in the dielectric, and the corresponding charge is calculated, along with displacement created due to the force.

Table 3.2: Material Properties used in COMSOL Multiphysics

Property	**Air**	**PI-eTPU**	**Flexion X60**
Relative Permittivity (ϵ_r)	1.00059	5.73	4.68
Poisson's Ratio (ν)	0.0	0.4999	0.4999
Young's Modulus (E) Pa	1.01×10^{-5}	2.2×10^{7} [79]	6×10^{6} [79]
Density (ρ) $\mathrm{kg\,m^{-3}}$	1.225	1100	1000
Electrical Conductivity (σ) $\mathrm{S\,m^{-1}}$	0.0	1.2	1.3

Each model is explained further in the next part of this report, and the results are shared in section 6.

Triangular Design

Because of its complicated design as explained in section 3.3, and the unavailability of triangles and pyramids as geometry in the software, it was decided to make a 2D simulation for this design. This reduced the computational time, which allowed to obtain the analysis with finer element sizes. A depth of 20 mm was used out of the plane and the periodic continuity condition was applied to both sides. The force was applied on the top plate of Expanded Thermoplastic Polyurethane (eTPU) using the 'Solid Mechanics' physics. Additionally, a layer of 2 mm is added as the dielectric layer, shown in Figure 2.12.

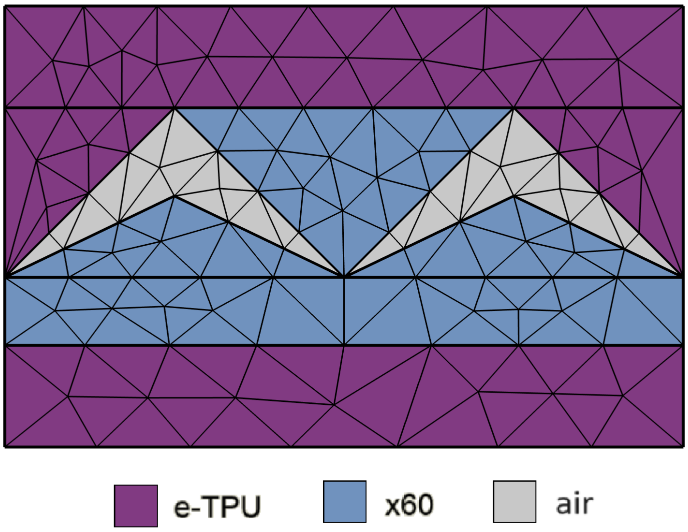

Figure 3.1: 2D FEA simulation of triangular design using COMSOL Multiphysics with the manually designed mesh setting, with the purple colour as electrodes made of Expanded Thermoplastic Polyurethane (eTPU), the blue colour as dielectric material X60, and the grey colour as deforming domain, air. The top terminal is at 1 V and the top boundary has a force applied to it. The bottom terminal is grounded, and the bottom boundary is mechanically restricted.

The mesh in Figure 3.1 is manually set, with parameters shown in Table 3.3.

The physics added to this model are Solid Mechanics and Electrostatics. For Solid Mechanics physics, the software automatically assumes all the parts of the component to have linear elastic properties. The initial values of Voltage for each component are also assumed to be 0 V and the dielectric layers are assumed to follow the charge conservation laws by the software while adding the Electrostatics physics.

Element Size Parameters	**Value**
Maximum element size:	1 mm
Minimum element size:	0.5 mm
Maximum element growth rate:	1.1
Curvature factor:	0.5
Resolution of narrow regions:	1

Table 3.3: Mesh manually created, shown in Figure 3.1

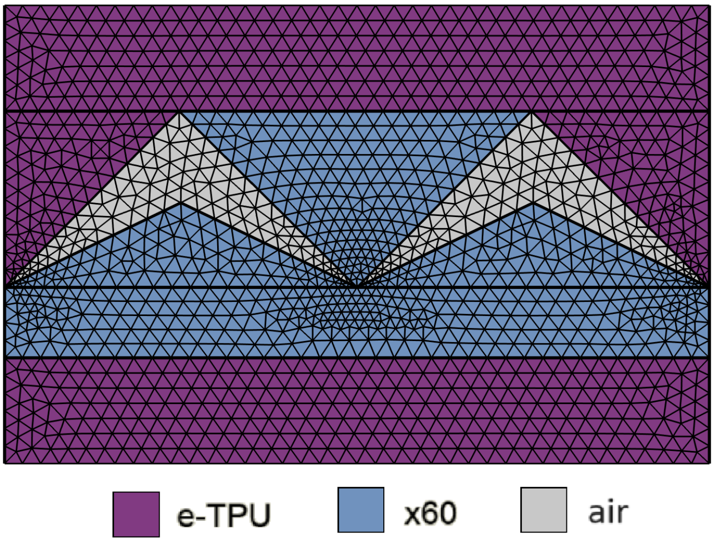

Figure 3.2: 2D FEA simulation of triangular design using COMSOL Multiphysics with the 'extremely fine' mesh setting, with the top terminal at 1 V and the top boundary has a force applied to it. The bottom terminal is grounded, and the bottom boundary is mechanically restricted.

Another model was made with the same parameters, but instead of adding physics using 'Solid Mechanics', the geometry of the components was dependent on a variable, that was swept manually to simulate air leaving from the air gaps as the force was applied on top of the structure. A function of cos of the angle 45° is used with a variable that is swept over the constant radius of 0.7 mm, to calculate the change in height of the dielectric layer. Compression because of the elastic materials is omitted here for simplicity and added later while calculating the Analytic model, which is explained in the next section.

A simple capacitive 2D model was also made in COMSOL, without any artefacts, to understand the change in sensitivity due to the triangular design.

Rectangular Design

As shown in Figure 3.3, a 3D model is created to simulate the second design. Half of the design explained till now is used in this to make the simulation run faster.

Similar to the triangular design, another file was made in the rectangular design where instead of using Solid Mechanics as physics, the dimensions of the component were dependent on a variable, that was swept in such a way that the air gap purges out air and the volume of all materials stays constant. Elasticity of the materials is omitted for simplicity and added later while

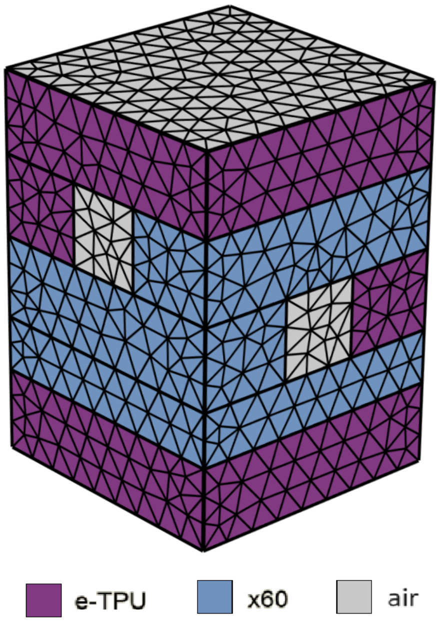

Figure 3.3: 3D FEA simulation of rectangular design using COMSOL Multiphysics with the 'extra fine' mesh setting, with the top terminal at 1 V and the top boundary has a force applied to it. The bottom terminal is grounded, and the bottom boundary is mechanically restricted.

calculating the Analytic model. A simple capacitive model was also made in 3D to understand the change in sensitivity due to the added rectangular artefacts. Results are discussed in the next chapter 6.

3.2 Analytical Model

A simple Python code was used to understand the effect of displacement on the capacitance since it was not possible to analyse it with COMSOL Multiphysics as seen in the above section. This section explains two different models were created to study the physics of these effects. The results are discussed in Chapter 6.

3.2.1 Triangular Design

For this model, it is important to understand how the electric field interacts with the electric charges that produce capacitive effects in the model. For this, Maxwell's equations are used. The generalized form of this relationship is described in the following equations.

Maxwell's Equations

Gauss's Law for Electricity expresses the divergence of the electric field E in terms of the electric charge density ρ:

$$\nabla \cdot E = \frac{\rho}{\varepsilon_0} \tag{3.1}$$

Gauss's Law for Magnetism expresses the divergence of the magnetic field B and indicates that there are no magnetic mono-poles:

$$\nabla \cdot B = 0 \tag{3.2}$$

Faraday's Law of Electromagnetic Induction relates the curl of the electric field E to the time rate of change of the magnetic field B:

$$\nabla \times E = -\frac{\partial B}{\partial t} \tag{3.3}$$

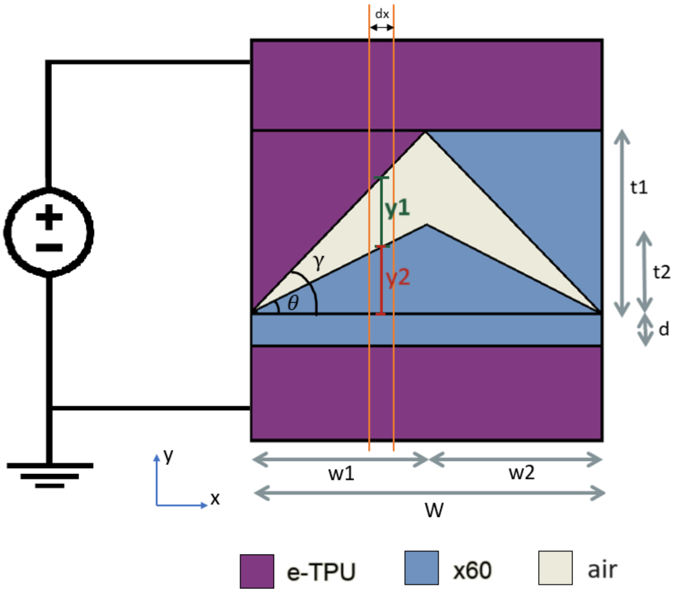

Figure 3.4: Cross-section of a unit cell of the final design triangles, extended L mm out of the plane.

Ampere's Circuital Law relates the curl of the magnetic field B to the current density J and the time rate of change of the electric field E:

$$\nabla \times B = \mu_0 J + \mu_0 \varepsilon_0 \frac{\partial E}{\partial t} \tag{3.4}$$

Gauss's electrical equation 3.1 is in the divergence form, and thus, true for every point in the space. It can be expanded as follows for the two-dimensional sensor:

$$\frac{\partial E_{\mathrm{x}}}{\partial x} + \frac{\partial E_{\mathrm{y}}}{\partial y} = \frac{\rho}{\varepsilon} \tag{3.5}$$

For wd, this equation can be rewritten in the integral form:

$$\oiint_{\mathrm{s}} D \cdot ds = \iiint_{V_{\mathrm{s}}} \rho_{\mathrm{free}}\, dV \tag{3.6}$$

It shows the relationship between the electric field E with the closed surface s denoted by $\oiint_{\mathrm{s}}$ and the distribution of the electric charge density ρ within the closed volume V_{s}.

To find the capacitance of a slice of dx length, as shown in figure 3.4, the following assumptions are considered:

- The Expanded Thermoplastic Polyurethane (eTPU) is conductive and therefore acts as equipotential plates at 0 and V volts, respectively.
- This makes the electric field to be developed primarily along the y axis. Along the x axis, E_{x} is eliminated:
$$\iiint_{V} \rho\, dV = 0 \tag{3.7}$$
- Since the charge is conserved over the entire surface, the net flux of the electric field through a closed surface is zero. The electric field lines are confined to the y-direction

due to the boundary conditions set by the equipotential plates. Thus, the interference between air and the dielectric layer becomes:

$$\oiint_s D \cdot ds = 0 \tag{3.8}$$

Thus, for $E_{y,1}$ and $E_{y,2}$:

$$\varepsilon_1 E_{y,1} = \varepsilon_2 E_{y,2} \tag{3.9}$$

Also, from figure 3.4, y_1:

$$\begin{aligned} \tan(\gamma) &= \frac{y_1}{x} \\ y_1 &= x \tan(\gamma) \end{aligned} \tag{3.10}$$

and, y_2:

$$\begin{aligned} \tan(\theta) &= \frac{y_2}{x} \\ y_2 &= x \tan(\theta) \end{aligned} \tag{3.11}$$

Noting that $E = -\nabla V$ the voltage drop ΔV across the region $r : r_1 \rightarrow r_2$:

$$\Delta V = -\int_{r_1}^{r_2} E(r) \cdot dr \tag{3.12}$$

$$E_{y,1}(t1 - y_1) + E_{y,2}(y_1 - y_2) + E_{y,3}(y_2 + d) = V \tag{3.13}$$

From figure 3.4 and equation 3.9, and taking $\varepsilon_{X60} = \varepsilon_x$:

$$E_{y,1} = E_{y,3} = E_{air}/\varepsilon_x \tag{3.14}$$

Using equation 3.14 in equation 3.13 and dropping the y-subscript since we only consider the fields in the y-direction:

$$\begin{aligned} V &= E_{air} \left\{ \frac{(t - y_1)}{\varepsilon_x} + (y_1 - y_2) + \frac{(y_2 + d)}{\varepsilon_x} \right\} \\ E_{air} &= \frac{V \varepsilon_x}{(t - y_1) + \varepsilon_x (y_1 - y_2) + (y_2 + d)} \end{aligned} \tag{3.15}$$

and for the dielectric displacement:

$$\begin{aligned} D_k &= \varepsilon_0 \varepsilon_x E_k \\ &= \frac{\varepsilon_0 \varepsilon_x E_{air}}{\varepsilon_x} \\ &= \frac{\varepsilon_0 \varepsilon_x V}{(t - y_1) + \varepsilon_x (y_1 - y_2) + (y_2 + d)} \\ &= \frac{\varepsilon_0 \varepsilon_x V}{(t + d) + (\varepsilon_x - 1)(y_1 - y_2)} \end{aligned} \tag{3.16}$$

where k is an integer indicating the layer number ($k = 1, 3$).

The interface of Expanded Thermoplastic Polyurethane (eTPU) and x has a free surface charge density σ. From equation 3.6, the free charge density, ρ_{free}, can be derived and related to the surface charge density σ according to:

$$\begin{aligned} \oiint_{S} D \cdot ds &= \iiint_{V_s} \rho_{\text{free}}\, dV \\ D_1 \cdot A &= \sigma A \\ \sigma &= D_1 \end{aligned} \tag{3.17}$$

The capacitance measured in a slice of width dx can be derived by the charge q on either conductor per the voltage between the conductors:

$$\begin{aligned} C(x)dx &= \frac{q}{V} = \frac{\sigma A}{V} = \frac{\sigma L}{V} dx \\ &= \frac{\varepsilon_0 \varepsilon_{\text{x}} L}{(t+d) + (\varepsilon_{\text{x}} - 1)(y_1(x) - y_2(x))} dx \end{aligned} \tag{3.18}$$

where L is the length of the structure in z-direction, perpendicular to the plane of the drawing as in Figure 3.4.

Total capacitance C_{wd} can be derived by the integration of this capacitance $C(x)dx$ in the entire width of wd:

$$C_{\text{wd}} = \int_0^{wd} \frac{\varepsilon_0 \varepsilon_{\text{x}} L}{(t+d) + (\varepsilon_{\text{x}} - 1)(y_1 - y_2)}\, dx \tag{3.19}$$

To simplify this equation 3.19, the following substitutions are made:

$$(y_1 - y_2) = x\big(\tan(\gamma) - \tan(\theta)\big) \tag{3.20}$$

$$(\varepsilon_{\text{x}} - 1)\big(\tan(\gamma) - \tan(\theta)\big) = \alpha(t_1) \tag{3.21}$$

$$t_1 + d = \beta \tag{3.22}$$

Note that $\alpha = \alpha(t1)$, i.e. a function of the thickness of the upper X60 layer. Replacing them in the equation 3.19:

$$\begin{aligned} C_{\text{wd}} &= \int_0^{wd} \frac{\varepsilon_0 \varepsilon_{\text{x}} L}{\beta + \alpha(t_1)x}\, dx \\ &= \frac{\varepsilon_0 \varepsilon_{\text{x}} L}{\alpha(t_1)} \ln\big(\beta + x\alpha(t_1)\big)\Big|_0^{wd} \end{aligned} \tag{3.23}$$

This gives the final expression for the total capacitance in the region with width wd:

$$C_{\text{wd}} = \frac{\varepsilon_0 \varepsilon_{\text{x}} L}{\alpha(t_1)} \ln\left(\frac{\beta + wd\alpha(t_1)}{\beta}\right) \tag{3.24}$$

Similarly, for the area under the width we, the voltage can be derived as:

$$E_2(y_1 - y_2) + E_3(y_2 + d) = V \tag{3.25}$$

Here, like in Equation 3.14

$$E_2 = \frac{E_{\text{air}}}{\varepsilon_{\text{x}}} \tag{3.26}$$

Replacing the new E_x in equation 3.26 and replacing the values of y_1 and y_2 from equation 3.10 and 3.11, respectively:

$$\begin{aligned}
D_1 &= \varepsilon_0\varepsilon_\mathrm{x}E_1 \\
&= \frac{\varepsilon_0\varepsilon_\mathrm{x}V}{\varepsilon_\mathrm{x}y_1 + d + (1-\varepsilon_\mathrm{x})y_2} \\
&= \frac{\varepsilon_0\varepsilon_\mathrm{x}V}{\varepsilon_\mathrm{x}x\tan(\gamma) + d - (\varepsilon_\mathrm{x}-1)x\tan(\theta)} && (3.27) \\
&= \frac{\varepsilon_0\varepsilon_\mathrm{x}V}{x\left\{\varepsilon_\mathrm{x}\tan(\gamma) - (\varepsilon_\mathrm{x}-1)\tan(\theta)\right\} + d} && (3.28) \\
&= \frac{\varepsilon_0\varepsilon_\mathrm{x}V}{x\alpha(t1) + \beta} && (3.29)
\end{aligned}$$

The substitutions that are replaced in the equation for simplification are as follows:

$$\varepsilon_\mathrm{x}\tan(\gamma) - (\varepsilon_\mathrm{x}-1)\tan(\theta) = \alpha(t1) \tag{3.30}$$

$$d = \beta \tag{3.31}$$

Similarly, total capacitance C_wd can be derived by the integration of this capacitance $C(x)dx$ in the entire width of we:

$$\begin{aligned}
C_\mathrm{we} &= \int_0^{we} \frac{\varepsilon_0\varepsilon_\mathrm{x}L}{x\alpha(t1)+\beta}\,dx && (3.32) \\
&= \frac{\varepsilon_0\varepsilon_\mathrm{x}L}{\alpha(t1)}\ln\left(\frac{\beta + we\alpha(t1)}{\alpha(t1)}\right)\bigg|_0^{we} && (3.33) \\
&= \frac{\varepsilon_0\varepsilon_\mathrm{x}L}{\alpha(t1)}\ln\left(\frac{\beta + we\alpha(t1)}{\alpha(t1)}\right) && (3.34)
\end{aligned}$$

This gives the final expression for the total capacitance in the region with width we.

In figure 3.4, it is visible that both these regions with length we and wd, act in parallel to each other. Thus, total capacitance C_tot can be derived by the scalar sum of both these capacitors.

$$C_\mathrm{tot} = C_\mathrm{we} + C_\mathrm{wd} \tag{3.35}$$

3.2.2 Rectangular Design

As explained in section 2, the second design can be assumed as a chain of parallel rungs of different capacitors and resistors in series. The change in capacitance is observed due to two major mechanisms: 1) the effect of force on the top electrode, which changes the distance between the electrode plates in the capacitive sensor, and 2) the bulging effect seen in the dielectric material because of the air gaps around it.

For figure 3.6, the geometry can be one of the three cases, based on the slicing position.

For the case where no force is applied on the top layer, the capacitance is given by equation 3.36:

$$C_\mathrm{eq} = (2C_\mathrm{we}) + C_\mathrm{wd} + C_\mathrm{wa} \tag{3.36}$$

For dielectrics stacked on each other between the electrodes, the capacitance acts like two capacitors where both dielectrics are in series. Thus, we can derive

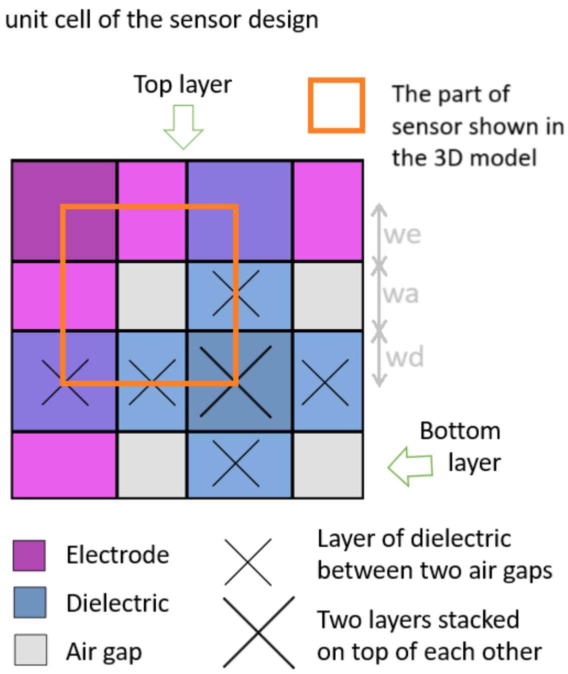

Figure 3.5: Top view of the structural design of the rectangular design. For the later calculations, the part inside the orange box is considered a unit cell.

$$\begin{aligned}\frac{1}{C} &= \frac{1}{C_1} + \frac{1}{C_2} \\ &= \frac{h_1}{\varepsilon_1 A_1} + \frac{h_2}{\varepsilon_2 A_2}\end{aligned} \tag{3.37}$$

Since the area under the electrode surface is the same for both dielectrics, $A_1 = A_2 = A$:

$$C = \frac{\varepsilon_1 \varepsilon_2 A}{\varepsilon_1 h_2 + \varepsilon_2 h_1} \tag{3.38}$$

For we in figure 3.6, for the case where the pattern is an electrode extension,

$$C_{\mathrm{w_1 c_1}} = \frac{\varepsilon_0 \varepsilon_\mathrm{r} weL}{\varepsilon_\mathrm{r}\, t2 + d} \tag{3.39}$$

In the case where the pattern is dielectric,

$$C_{\mathrm{wec2}} = \frac{\varepsilon_0 \varepsilon_\mathrm{r} weL}{\varepsilon_\mathrm{r}\, t2 + t1 + d} \tag{3.40}$$

and for the case where the pattern is an air gap,

$$C_{\mathrm{we\ c3}} = \frac{\varepsilon_0 \varepsilon_\mathrm{r} weL}{\varepsilon_\mathrm{r}(t1 + t2) + d} \tag{3.41}$$

This case is added twice in the final equation of C_{we} as we have two air gaps in our design.

Thus, we obtain the expression for C_{we} in equation 3.36, as

$$\begin{aligned}C_{\mathrm{we}} &= C_{\mathrm{wec1}} + C_{\mathrm{wec2}} + 2C_{\mathrm{wec3}} \\ &= \frac{\varepsilon_0 \varepsilon_\mathrm{r} weL}{\varepsilon_\mathrm{r}(t2) + d} + \frac{\varepsilon_0 \varepsilon_\mathrm{r} weL}{\varepsilon_\mathrm{r}(t2) + t1 + d} + \frac{2\varepsilon_0 \varepsilon_\mathrm{r} weL}{\varepsilon_\mathrm{r}(t1 + t2) + d}\end{aligned} \tag{3.42}$$

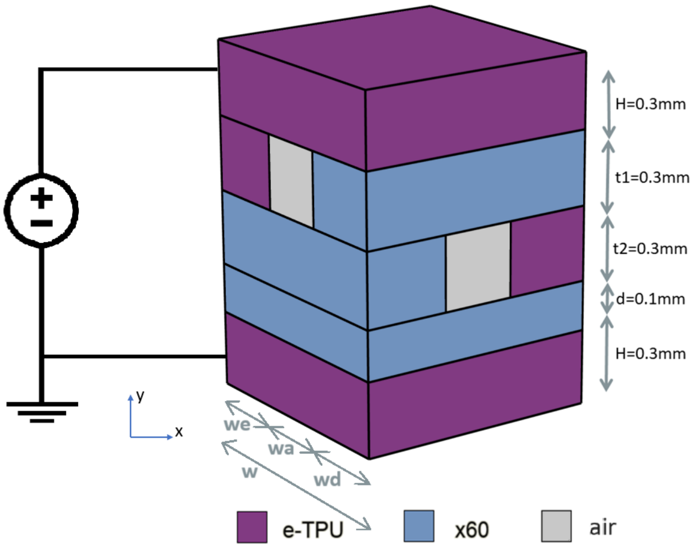

Figure 3.6: Cross-section of a unit cell of the final rectangular design. This structure is repeated for Lmm in the direction transverse to w.

For wd in figure 3.6, for the case where the pattern is an electrode extension,

$$C_{\mathrm{wdc1}} = \frac{\varepsilon_0 \varepsilon_\mathrm{r} wdL}{t2 + d} \tag{3.43}$$

In the case where the pattern is dielectric,

$$C_{\mathrm{wdc2}} = \frac{\varepsilon_0 \varepsilon_\mathrm{r} wdL}{t1 + t2 + d} \tag{3.44}$$

and for the case where the pattern is an air gap,

$$C_{\mathrm{wdc3}} = \frac{\varepsilon_0 \varepsilon_\mathrm{r} wdL}{\varepsilon_\mathrm{r}(t1) + t2 + d} \tag{3.45}$$

Similarly, we obtain the expression for C_{wd} in equation 3.36, as

$$\begin{aligned} C_{\mathrm{wd}} &= C_{\mathrm{wdc1}} + C_{\mathrm{wdc2}} + 2C_{\mathrm{wdc3}} \\ &= \frac{\varepsilon_0 \varepsilon_\mathrm{r} wdL}{t2 + d} + \frac{\varepsilon_0 \varepsilon_\mathrm{r} wdL}{t1 + t2 + d} + \frac{2\varepsilon_0 \varepsilon_\mathrm{r} wdL}{\varepsilon_\mathrm{r}(t1) + t2 + d} \end{aligned} \tag{3.46}$$

And for wa in figure 3.6, the expression is similar to

$$C_{\mathrm{wac}} = \frac{\varepsilon_0 \varepsilon_\mathrm{r} waL}{d} \tag{3.47}$$

and thus we get the total of

$$C_{\mathrm{wa}} = \frac{4\varepsilon_0 \varepsilon_\mathrm{r} waL}{d} \tag{3.48}$$

Applying the values of C_{we}, C_{wd} and C_{wa} in equation 3.36, we get

$$\begin{aligned} C_{\mathrm{eq}} &= (2C_{\mathrm{we}}) + C_{\mathrm{wd}} + C_{\mathrm{wa}} \\ &= \frac{2\varepsilon_0 \varepsilon_\mathrm{r} weL}{\varepsilon_\mathrm{r}(t2) + d} + \frac{2\varepsilon_0 \varepsilon_\mathrm{r} weL}{\varepsilon_\mathrm{r}(t2) + t1 + d} + \frac{4\varepsilon_0 \varepsilon_\mathrm{r} weL}{\varepsilon_\mathrm{r}(t1 + t2) + d} + \frac{\varepsilon_0 \varepsilon_\mathrm{r} wdL}{t2 + d} \\ &+ \frac{\varepsilon_0 \varepsilon_\mathrm{r} wdL}{t1 + t2 + d} + \frac{2\varepsilon_0 \varepsilon_\mathrm{r} wdL}{\varepsilon_\mathrm{r}(t1) + t2 + d} + \frac{4\varepsilon_0 \varepsilon_\mathrm{r} waL}{d} \end{aligned} \tag{3.49}$$

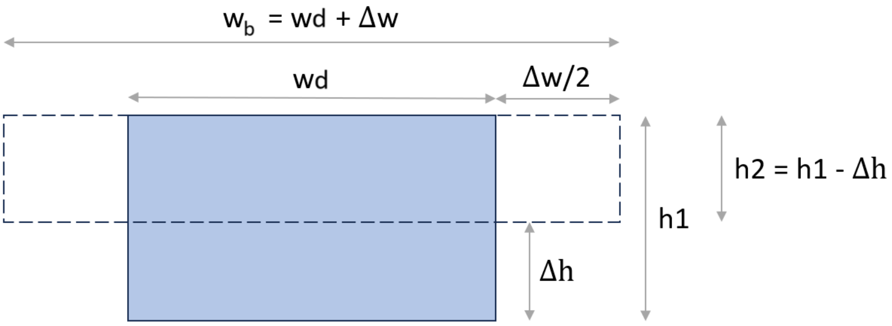

Figure 3.7: Effect of bulging in the dielectric layer between two air gap layers.

Apart from this effect, the dielectric layer has an additional effect of bulging when force is applied to the sensor. ΔC can be characterized by the change in dimensions of the dielectric as it spreads to the layer with air gaps. Thus, it is seen in both the layers, in both x and y dimensions, for every cell of X60 between two air gaps. X60 is an in-compressible material with Poison's ratio of ≈ 0.4999, which causes the bulging of material as its density remains constant as the material is compressed.

$$\begin{aligned} weh1 &= wdh2 = \text{constant} \\ &= (we+\Delta w)(h1-\Delta h) \\ &= weh1+\Delta wh1-\Delta hwe-\Delta h\Delta w \end{aligned} \tag{3.50}$$

which gives

$$\Delta w = \frac{\Delta hwe}{h1-\Delta h} \tag{3.51}$$

This effect is characterized in the code by sweeping the dimension of the structure. Additional change in capacitance due to applied force ΔC is given by

$$\begin{aligned} \Delta C &= \frac{\varepsilon_0\varepsilon_\mathrm{r}\cdot\ \text{area}}{\text{distance}} \\ &= \frac{\varepsilon_0\varepsilon_\mathrm{r} wd}{h2} \\ &= \frac{\varepsilon_0\varepsilon_\mathrm{r}(we+\Delta w)}{h1-\Delta h} \end{aligned} \tag{3.52}$$

Replacing values of Δw from 3.51,

$$\begin{aligned} &= \frac{\varepsilon_0\varepsilon_\mathrm{r}(we+\frac{\Delta hwe}{h1-\Delta h})}{h1-\Delta h} \\ &= \frac{\varepsilon_0\varepsilon_\mathrm{r}\frac{(we+h1+\Delta hwe-\Delta hwe}{h1-\Delta h})}{h1-\Delta h} \\ &= \frac{\varepsilon_0\varepsilon_\mathrm{r} weh1}{h1-\Delta h^2} \end{aligned} \tag{3.53}$$

As seen in figure 3.5, this pattern is repeated twice when both dielectric layers are stacked on top of each other, and once in all the other dielectric layers, except when the electrode is below the dielectric layer, for 8/16. Replacing $h1 = t1 + t2 + d$ gives us the final expression of capacitance.

$$C_r = C_{eq} + \frac{8}{16}\Delta C \tag{3.54}$$

$$\tag{3.55}$$

3.3 CAD models

To test the reproducibility of the design and fabrication process, the sensors were printed multiple times in the same print setting, once individually and once in a column of 5 sensors per print.

More information about these sensors can be found in Appendix D.

These design iterations were modified to suit the printing capabilities of the printer. Apart from the printer, the properties of the materials were also considered while the prints were made.

3.3.1 Triangular Design

Figure 3.8 and Figure 3.9 show the CAD model of the triangular design, with the artefacts of the dielectric layer added in x and y directions, respectively.

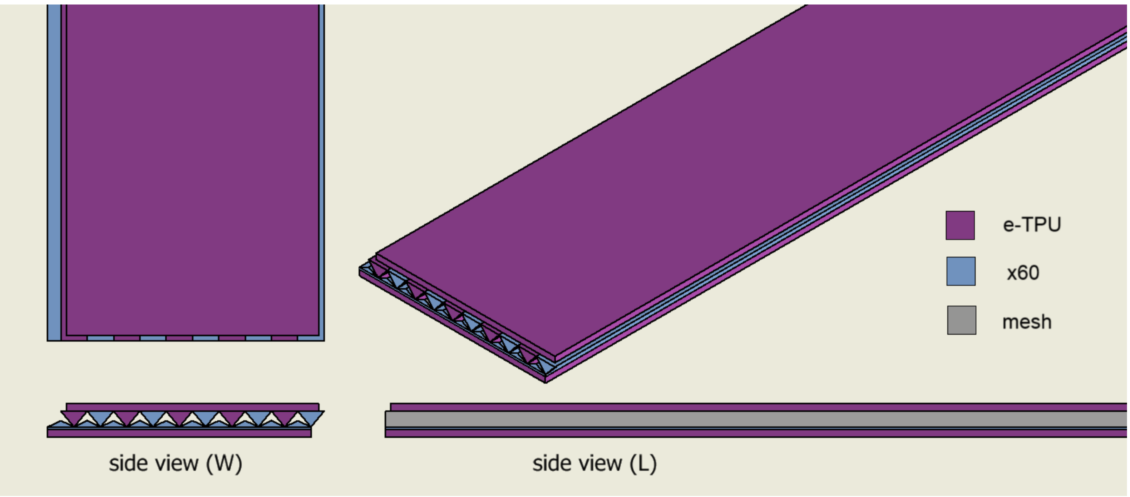

Figure 3.8: CAD model of design with triangular artefacts along the X direction.

There is empty space in the design, where the next material pointing on top of it has no support. Initially, BVOH was used here, and the entire printed sensor was submerged in water for a few hours. Post that, the printed sensors were put in the oven to be baked, as explained in section 4.2.7. The resulting sensor design was tearing along the places where the top electrode did not have support while being baked. To avoid such problems, the air gap was reduced, and the print was done upside down, with the top layer printed first on the printer bed. After all these modifications, in the last iterations, the use of support material BVOH was omitted.

3.3.2 Rectangular Design

Figure 3.10 and Figure 3.11 show the rectangular design's CAD model, with the dielectric layer artefacts added in X and Y directions, respectively.

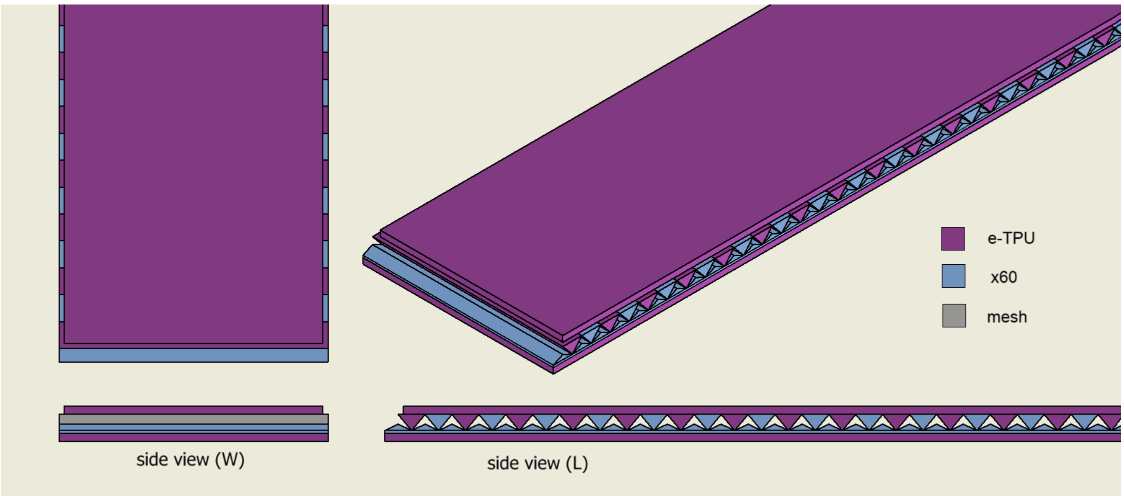

Figure 3.9: CAD model of design with triangular artefacts along the Y direction.

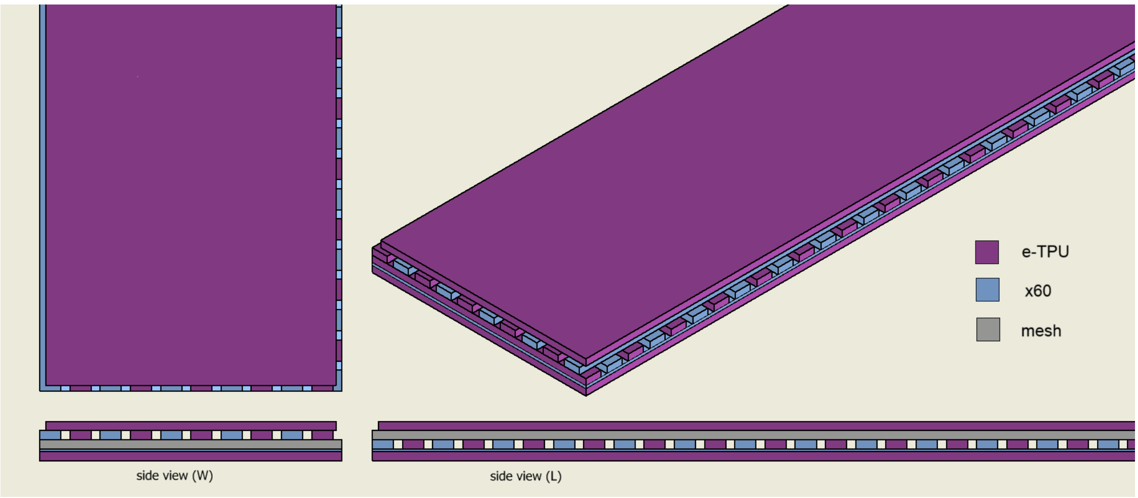

Figure 3.10: CAD model of design with rectangular artefacts along the X direction on the top layer, and along the Y direction on the bottom layer.

Like in the triangular design, there is empty space in this design too, where the next material pointing on top of it has no support. This space, characterised as air gaps, is cuboidal. Initially, BVOH was used here as well, and the entire printed sensor was submerged in water for a few hours. The use of BVOH was omitted in the newer prints, like in the previous design. The width of the air gap was reduced majorly, and the width of the dielectric as well as the cogs were increased on both sides. It was tough to have the Expanded Thermoplastic Polyurethane (eTPU) top layer adhere to the previous layer of printed X60. To avoid issues as shown in Figure 4.1, the width of the Expanded Thermoplastic Polyurethane (eTPU) layers in the dielectric layer was increased.

Design-related decisions were motivated due to these effects experienced during the fabrication process. These motivations and changes in the design process are expanded in chapter 6.

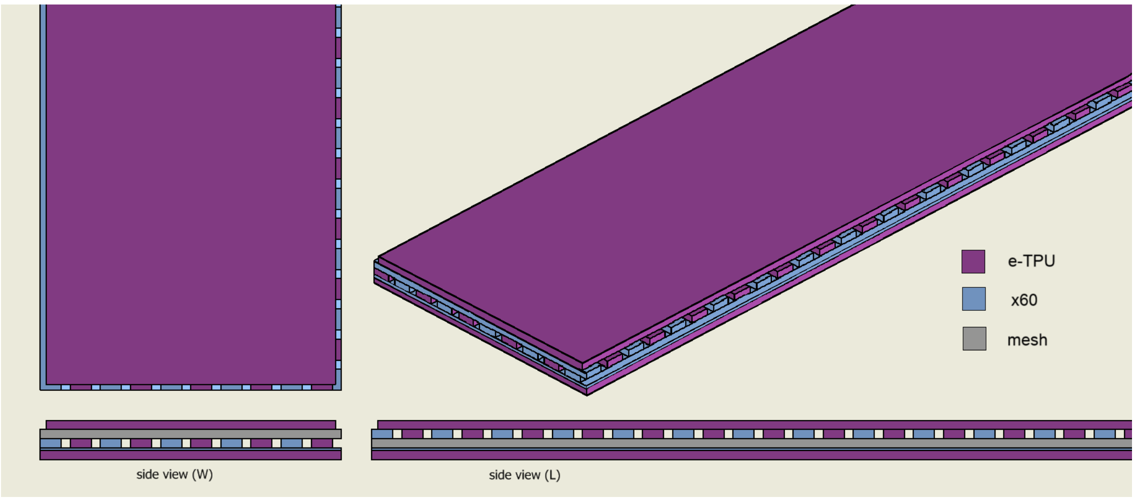

Figure 3.11: CAD model of design with rectangular artefacts along the Y direction on the top layer, and along the X direction on the bottom layer.

3.4 Conclusions

This chapter introduced the mathematical as well as the FEA models of the sensor designs. An analytical model was also presented to compare the simulation results and further understand and test the concept on which the new and improved design is based. CAD models were introduced for the new designs and the motivation to choose its dimensions was discussed. These CAD models were fabricated and tested in an experiment designed to test these simulated results in practice.

4 Materials and Fabrication Method

In this chapter, the choices made for the design and fabrication of the sensor are explained. The first part describes the requirements for the design, which is followed by introducing the materials used, with the help of material properties such as Poisson's ratio and Young's modulus. The later part explains the design iterations and modifications. Most of the design decisions are based on the possibility of fabricating the design, as the research was mostly focused on the fabrication possibilities of such complex designs in the sub-millimetre range.

Wehner et al. demonstrated the operation of an entirely soft, autonomous robot using a multimaterial, embedded 3D printing technique. The robot's elastomeric architecture and rapid fabrication approach enable the programmable assembly of multiple materials [80]. Morrow et al. devised a method for fabricating pneumatic structures using 3D printing. Soft robotic applications can benefit from these structures. They offer a way to produce actuators and sensors with intricate geometries previously unattainable [81]. Bartlett et al. investigated the creation of pneumatic networks embedded in soft materials using 3D printing. These networks show how 3D printing may improve the adaptability and usefulness of soft robotic systems by enabling fine control over movement and shape-changing capabilities [82]. Hiller and Lipson created soft actuators using 3D printing, which made it possible to create intricate and flexible robotic parts. Their research showed how soft robots might be quickly prototyped and customized, facilitating design iterations and functional improvements [83]. Truby et al. used 3D printing to develop bio-inspired robots by focusing on inserting soft materials to replicate the flexibility and mobility observed in nature. Their creations demonstrate their ability to construct intricately functioning structures with lifelike movements [84]. Somireddy et al. investigate novel structural designs to incorporate air gaps, fabricated using 3D printing. This manufacturing approach is quite adaptable. It is possible to adjust the design to achieve desired attributes like strength and flexibility by controlling the dimensions, distribution, and form of the artefacts comprised in each print layer. In this way, it is possible to test several prototypes that qualify the structures as components suitable for specific applications [85].

The creative application of various conductive plastics and 3D printing as a fabrication process for various patterned structures can help to produce flexible, adaptable, and autonomous systems. Raguz et al. discovered that the actuation of electrically powered soft robots depends on the material characteristics and interacting Coulomb forces in their study on dielectric elastomeric actuators [86]. These researches demonstrate the wide potential of applications of 3D printing in the construction of soft, functioning robots, ranging from bio-inspired robots and printable pneumatics to soft actuators and pneumatic networks. The fabrication technique, 3D printing, is introduced in the next section.

4.1 3D Printing

3D printing of a part comprises the following steps:

- **Design:** The first step, the design, involves creating a 3D model of the part using Computer-Aided Design software, such as Inventor [87] or SolidWorks [88].

- **Pre-processing:** Subsequently, the model is converted into an STL file and sliced into G-code using specialized software such as CURA [89], which determines the path for the printer's extruder to follow. Each slice of the part corresponds to a layer of a certain height printed on top of the previous layer. Pre-processing also involves preparing and drying the filament material using a Materials Management System (MMS).

- **Fabrication:** The second step, known as fabrication, involves loading the filament into the printer and initiating the print job. The printer adds each slice of the part on top of the previous layer, starting with the first layer, which is deposited on a heated build plate to ensure proper bonding. The printed part and any printed support structures are removed from the build platform after printing is completed.
- **Post-processing:**The third and final step, called post-processing, involves removing any support materials that were printed along with the part and cleaning the part if necessary. This step may also include annealing the part by baking it to achieve certain material properties.

In this project, multiple parts were printed together in an assembly that consisted of different parts snapped to each other. It was possible to print this way because of the 3D printer employed for this assignment. The Diabase H series printer is manufactured by Diabase Engineering and is equipped with five extruders. All extruders are integrated into an automated tool changer, enabling the sequential printing of up to five distinct materials within the same print. The printer is equipped with a Flexion Direct Drive Extruder [90], which can facilitate high-speed printing of ultra-flexible filament materials, as required for the current designs. The cam dial and cam follower screw system of the printer include four settings that are designed to compress the filament to varying degrees before extrusion, depending on the material being printed. The printer also features an enclosure that prevents contamination and maintains the temperature while printing.

In the next sections, the materials used are introduced and subsequently, their properties are discussed.

4.2 Materials

Since the sensor previously designed by Patel is a capacitor, it is important to understand the workings of a basic capacitor to design it.

$$C = \frac{q}{V} = \frac{\epsilon_r \epsilon_0 A}{d} \tag{4.1}$$

C is the total capacitance of the sensor, q is the charge on the plates, A is the total area of the plates, d is the thickness of the dielectric layer, ϵ_r is the relative permittivity of the dielectric material, and ϵ_0 is the permittivity of vacuum.

The previously designed sensor had a good capacitive response but was lacking in sensitivity. For better sensitivity, the new sensor should be a better capacitor - the structure should be more flexible, and the dielectric should be more susceptible. Since the sensor will be made using 3D printing, the material has to be flexible, conductive, and commercially available filament.

It is important to understand the role of mechanical properties like Poisson's ratio and Young's modulus, as they influence the structural integrity and functionality of stretchable materials.

Young's Modulus

Young's modulus (E) is a measure of the stiffness of a material. It quantifies the material's ability to deform elastically under force. Materials with a low Young's modulus are more flexible, adding sensitivity. However, excessive deformation might lead to a variety of non-linearities, affecting the sensor's structural collapse.

Poisson's Ratio

Poisson's ratio (ν) is the ratio of the transverse strain to the axial strain in a material. High Poisson's ratio (≈0.5) indicates the material's ability to conserve volume under axial stress. The uniform thickness of the dielectric layer is maintained during stretching or compression, stabilizing capacitance changes in the layer. A material with a low Poisson's ratio exhibits less lateral expansion when stretched, giving a higher capacitance change.

Poisson's ratio and Young's modulus are vital in the design and use of flexible capacitive sensors to ensure physical stress while producing clear and consistent readings. The balance of durability, sensitivity, and flexibility are the deciding factors for determining the right materials.

In this regard, materials like Thermoplastic Polyurethane (TPU) and Polydimethylsiloxane (PDMS) are frequently employed in flexible sensors. These characteristics support the sensors' ability to withstand a variety of mechanical deformations while maintaining the inner structure and functionality.

Rogers et al. present creative approaches for combining circuits with elastomeric substrates, enabling such materials to undergo deformation while retaining electrical properties. This facilitates developing flexible electrical devices possible with alternative materials [8]. Yu et al. emphasize the importance of patterning techniques and the mechanical properties to preserve conductivity despite extreme deformations such as bending, twisting, and stretching [26].

4.2.1 Materials used

For fabrication using FDM/FFF, both the dielectric layer and the conductive electrode layer need to be made out of soft and flexible materials that are already available in filament form in the market. For a relatively large difference in the height of the dielectric layer, high elasticity as well as high mechanical compliance are required. In previous work by Patel, a few materials are tested. eTPU and X60 were chosen based on the results [24].

4.2.2 PI-eTPU 85-700+

Thermoplastic Polyurethane (TPU) is widely used to make waterproof or watertight parts, such as sports equipment or footwear. The material in itself is hygroscopic, absorbing moisture from the air. When fabricated using 3DP, the material bonds with itself and undergoes the process of thermosetting, making the parts to be waterproof.

Because of its exceptional elasticity and durability, TPU is used in applications that require frequent loading and unloading cycles. It also exhibits viscoelastic characteristics demonstrating hysteresis, which results in non-linearities and energy dissipation in the capacitance response.

To design the sensor, PI-eTPU 85-700+ filament from Palmiga Innovations [91] was used for printing electrodes. It is an electrically conductive variant of this elastic TPU material. Carbon black is incorporated into the TPU matrix during the filament's manufacturing process, adding conductive qualities without sacrificing the TPU material's characteristic elasticity and flexibility. The shore hardness as reported by the manufacturer is 85 A and the maximum extension is more than 700 %. It has a Poisson ratio of 0.45 and a Young's Modulus of 22 MPa. Since this material is discontinued by the manufacturer, it is not possible to find the datasheet on their official website. This information is taken from the MSc report of Schouten [79]. Table-4.1 shows the mechanical and electrical properties of the material.

4.2.3 X60

Diabase Engineering's X60 is regarded as one of the softer 3D printing filaments available. It has inherent strength, elasticity, and flexibility, as TPU is the main foundation material. X60 is an ultra-flexible filament with a shore hardness of 60A and a high relative dielectric constant of around 5 [92], used to print the dielectric for the sensor. It has a Poisson ratio close to 0.5. The value of 0.4999 and a Young's Modulus of 6 MPa is taken for simulations [79]. X60 also can withstand a large electric field and is compatible with eTPU in a way that avoids chemical reactions that degrade the materials.

Table 4.1: Material Properties of Filament

Property	**PI-eTPU**	**Flexion X60**
Density	1.3 $\mathrm{g\,cm^{-3}}$	1.2 $\mathrm{g\,cm^{-3}}$
Tensile Strength	17 MPa	6 MPa
Tensile Modulus	12 MPa	1 MPa
Hardness	85 shore A	60 shore A
Relative Permittivity	60	4.79
Recommended Printing Temperature	200 °C – 230 °C	220 °C – 240 °C
Decomposition Temperature	250 °C	300 °C
Self-Ignition Temperature	> 340 °C	> 350 °C

Figure 4.1: Fabrication problems faced while printing the top layer of the sensor.

The dielectric layer of the elastic capacitor has a prominent impact on the performance of an elastomeric capacitive sensor [53]. Certain materials have different dielectric constants depending on how frequently an electric field is applied. When doing dynamic or high-speed tests, such frequency dependency is crucial. The frequency dependence of X60 makes it possible to employ the sensor for a multi-frequency approach, as discussed in Section 2.6. As seen in eq 4.1, capacitance is dependent largely on the ϵ_r, the relative permittivity of the dielectric material of the layer in between the electrodes as well as the electric field applied. The relative permittivity of these parameters is determined by both, the material's dielectric strength and the dielectric layer's thickness. The minimum dielectric layer that can be printed depends on the minimum layer thickness achievable by the printer as well as the number of layers required to separate both electrode layers from each other, avoiding a short circuit in the design. A nozzle with 0.4 mm diameter opening is used on a Diabase H series printer in this design. This FDM/FFF printer can print each layer at a minimal thickness of 0.06 mm.

4.2.4 Support Material

While fabricating using 3D printing, it was challenging to get the top electrode to print on the air gap, as eTPU from the top electrode layer did not have a heated base to adhere to. It caused effects as seen in Figure4.1. A snap assembly was considered to be employed for the fabrication, where the different parts were to be printed individually and fitted into a singular sensor. Disadvantages of FDM/FFF like poor layer adhesion due to the anisotropic distribution of the bending forces, especially for the assembly where both the mating parts are elastic, were key deciding factors for not continuing with the said method [93]. Apart from snap assembly, it was also considered using an interlocking connection, since the multi-material prototype did not have any durability criteria. For optimal friction, tension, and shear forces, a 0.5 mm tolerance is advised between the interlocking joints [94], which was way higher than the allowed tolerance of this design. Thus, it was also omitted.

Since these designs had to be a single assembly with multi-material printing, the 3D printer used was well capable of adding one more material to the assembly to solve this issue. It was decided to add a water-soluble filament to the assembly. Two different materials were explored for the same: Butenediol Vinyl Alcohol Copolymer [95] and PLA [96], based on the availability of the materials in the lab.

Figure 4.2: Dissolution of BVOH(left) versus PLA(right)

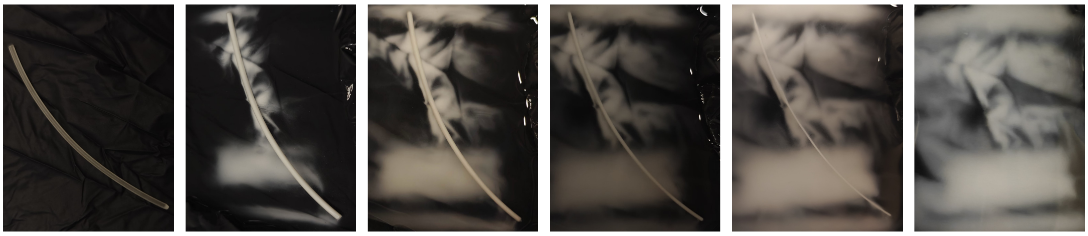

(a) t (b) t+15 (c) t+30 (d) t+45 (e) t+60 (f) t+75

Figure 4.3: Dissolution of BVOH filament, from time (t = time of adding water), till it gets completely dissolved.

As seen in Figure 4.2, PLA expands on dissolving. Apart from this, BVOH is a more efficient solute in terms of time and energy [97], this design utilized BVOH.

Based on the material properties, the manufacturer provides recommendations for parameters to be adjusted for the printer. This is done using slicing software, such as CURA, and is a part of the pre-processing stage of 3D printing. The next section explains the parameters used in this project and their impact on the prints.

4.2.5 Printing Parameters

The effect of printing parameters on the 3D printing process is explored in this section. For the various iterations of printing the design, the following parameters were experimented with:

Infill

A 3D-printed part consists of an outer wall and an infill section inside this wall. The infill section has two important parameters: the infill density and the infill pattern. The infill density refers to the percentage of material inside the part, while the infill pattern refers to the pattern in which the material is deposited inside the wall. Some common infill patterns include rectilinear, lines, honeycomb, triangular, and concentric. In the case of the flexible conductive filament eTPU used for the electrodes in this assignment, an 100 % infill density is utilized to minimize resistance and enhance conductivity. As flexibility is not a concern for the electrodes, a solid infill structure is preferred. On the other hand, the dielectric layer between the electrodes and sensors is compressible, and different infill densities can impact the capacitive sensing of the sensor. The default infill pattern of rectilinear is used for both materials.

Temperature

The printing process involves two temperature parameters—the nozzle temperature and the build plate temperature. The PI-eTPU filament used in printing is melted at a high temperature close to the nozzle and then solidified on the build plate. A very high temperature at the heater can cause the material to ooze and lead to printing inconsistency, which can affect the conductivity and mechanical properties of the sensors. Therefore, recommended temperature ranges were used as specified in the datasheet to print the sensors. The suggested print temperature range for eTPU is 200 °C to 230 °C [98], and for X60 is between 220 °C to 250 °C [99]. These temperature guidelines promote strong layer adhesion and avoid commonly encountered problems like clogging or under-extrusion. Based on the 3D printer, the print speed is recommended to be tested and adjusted. Table 4.2 shows the print temperature for both materials. Some test prints are shown in Figure 4.4.

Figure 4.4: Printed output of test samples with various print temperatures and print speeds.

The build plate temperature should be high enough to ensure proper adhesion between the layers. Build plate temperature of 75 °C is used to print the sensor assemblies.

Print Speed

The manufacturer of filament also recommends the speed for 3D printing the material. The recommended print speed for PI-eTPU ranges from 20 $\mathrm{mm\,s^{-1}}$ to 60 $\mathrm{mm\,s^{-1}}$ [98]. For X60, this parameter range is recommended to be 20 $\mathrm{mm\,s^{-1}}$ to 40 $\mathrm{mm\,s^{-1}}$ [99]. Considering the flexible nature of the materials, a lower speed is recommended, varying for different extruders and printers.

Cooling

To solidify the melted filament extruded from the nozzle, fans are used at varying speeds. For flexible filaments, a speed range of 50 % to 90 % is recommended. Cooling can help in cementing each layer quickly, reducing the chances of deformation and improving print accuracy by ensuring proper layer adhesion and surface finish by avoiding warping or detachment from the print bed. Nevertheless, the choice for the fan speed is highly dependent on the 3D printer. In this project, after multiple tests, the fan speed was set at 100 % for both filaments.

Walls

The number of wall lines and wall thickness are crucial for printing materials with the appropriate strength and flexibility, particularly when using flexible filaments. For PI-eTPU, a wall thickness of 1.2 mm to 2.0 mm is recommended by the manufacturer. for X60, this ranges from 1.2 mm to 2.4 mm. Depending on the nozzle diameter and the required print strength, this can amount to several wall lines. While smaller walls give more flexibility, thicker walls offer more strength and stiffness. For the assembly designed in this project, the parts were at a sub-millimetre level. It was difficult to explore this parameter, and it was set to be automatically determined by the slicer software.

Line width/Extrusion Multiplier

The extruder of a 3D printer deposits the filament material in thin lines, with the width of the line determined by the diameter of the nozzle and the extrusion multiplier. The extrusion multiplier parameter controls the amount of material that is extruded per unit length at a particular speed. This parameter alters the cross-sectional area of the extruded filament, affecting all the print's layers and fillings. The default value for the extrusion multiplier is 1 [100].

Table 4.2: Print settings

Printing parameter	**PI-eTPU**	**Flexion X60**
Layer height	0.1 mm, 0.06 mm	0.1 mm, 0.06 mm
Infill	100 %	100 %, 80 %
Print Temperature	210 °C	230 °C
Cooling	100 %	100 %
Nozzle Diameter	0.4 mm	0.4 mm
Extrusion width multiplier	1	1
Extrusion width	0.44	0.44
Cam dial settings	3	5

4.2.6 Printing Direction

Vu et al. explore the impact of different printing orientations (45°, 90°, and 180°) on the mechanical and electrical properties of sensors created using FDM with conductive TPU. The sensors printed at a 45° angle exhibit improved durability and stability under repeated mechanical stress compared to other orientations, allowing better distribution of mechanical forces [101].

The dielectric material must have a greater dielectric constant and a lower thickness. Additionally, it's critical to prevent dielectric breakdown, which occurs at different electric field strengths for different materials. Thus, it was important to have the dielectric layer higher than a certain thickness to avoid a breakdown in the sensor. To add further thickness in the dielectric layer, two different thicknesses of the dielectric layer are taken for each design; 0.1 mm and 0.2 mm.

4.2.7 Post Processing

To enhance the conductivity of the fabricated electrodes, all sensors produced in this project were subjected to annealing in an oven at a temperature of 150 °C for a duration of 24 h. The sensors had a slight curvature along the x and y axes. The electrical resistance of the electrodes was measured using a multi-meter, both before and after the annealing process. The results demonstrated a reduction in the electrical resistance of the electrodes for all the sensors. Additionally, there was a reduction in the dimensions of the sensors, and when the sensors were evaluated using the experimental setup, the results exhibited a noticeable difference in both resistance and capacitance output.

4.3 Conclusions

This chapter introduced conductive plastic materials that are used in making this sensor and 3D Printing using FDM/FFF as the fabrication method employed. Numerous areas of research were introduced in relative fields using the same. The process of 3D printing is outlined and relative material properties are explained before introducing the materials- eTPU and X60, used in this project to print the electrode and the dielectric respectively. Support materials used for printing the previous iterations of the designs were compared in the next section. The importance of the printing parameters was expressed, based on the materials used. Based on this information, a few designs were printed, and the impedance response of the sensors was tested on the setup explained in the next section.

5 Experimentation

This section describes the setup developed to test the sensor prototypes and explains the simulations created. The experiments performed are also explained in detail.

5.1 Experimental Setup

Modifications in the previous experimental setup were made to be able to test the 2D sensor such that the position probe actuator could be moved in along three axes, and could thus probe the maximum sensor size of 330*330 mm^2 size, larger than the common foot size of humans. Although the sensor prototype is not yet printed in this dimension, a setup was built as a pipeline for testing potential developments in that direction.

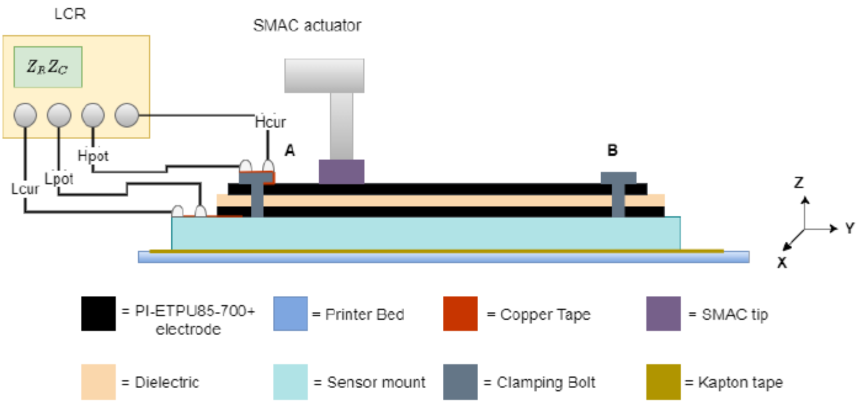

Figure 5.1: Schematic diagram of the experiment setup, courtesy [24].

To measure the impedance of this prototype, electrical contacts with an LCR were made as follows. To reduce the contact resistance, silver conductive paint (Ag) was painted on the top and bottom electrodes. A copper tape was applied to the bottom part of a plastic bed to rest the sensor and was wrapped around a small piece of plastic used as a press, in figure 5.1. This press was soldered with wires connected to the TiePieLCR, which will be explained later in this section. It also served the purpose of keeping the sensor stable on the plastic bed, ensuring that measurements stay undisturbed by any mechanical noise due to the movements in the setup.

The plastic bed was placed on the printing bed of FlexionStein3D using double-sided tape. This printing bed was a part of the system explained in the next subsection. It was grounded to avoid noise in the measurement, and Kapton tape was applied to the bed to avoid damage from the double-sided tape.

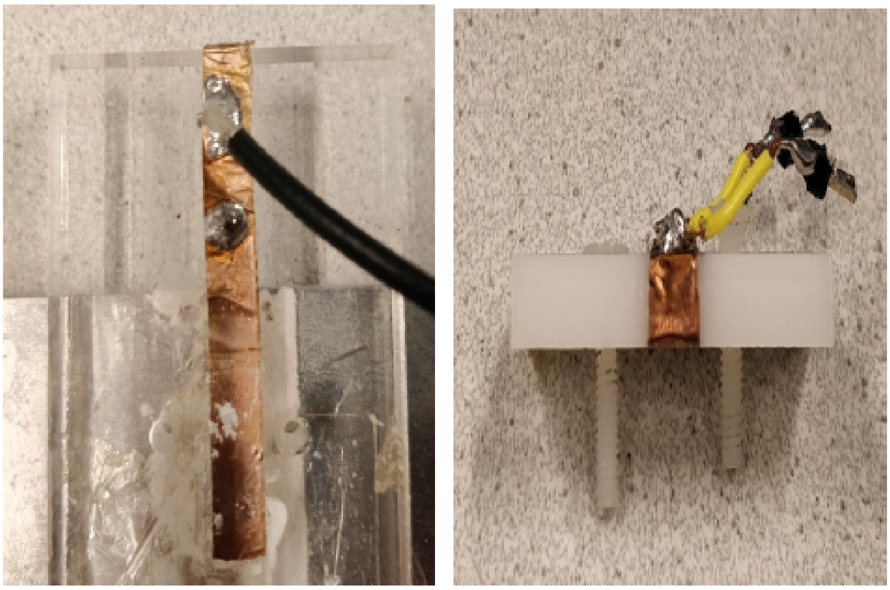

Figure 5.2: Copper tape placed on the mount with soldered wires to connect the bottom electrode and the top electrode, respectively, courtesy [24].

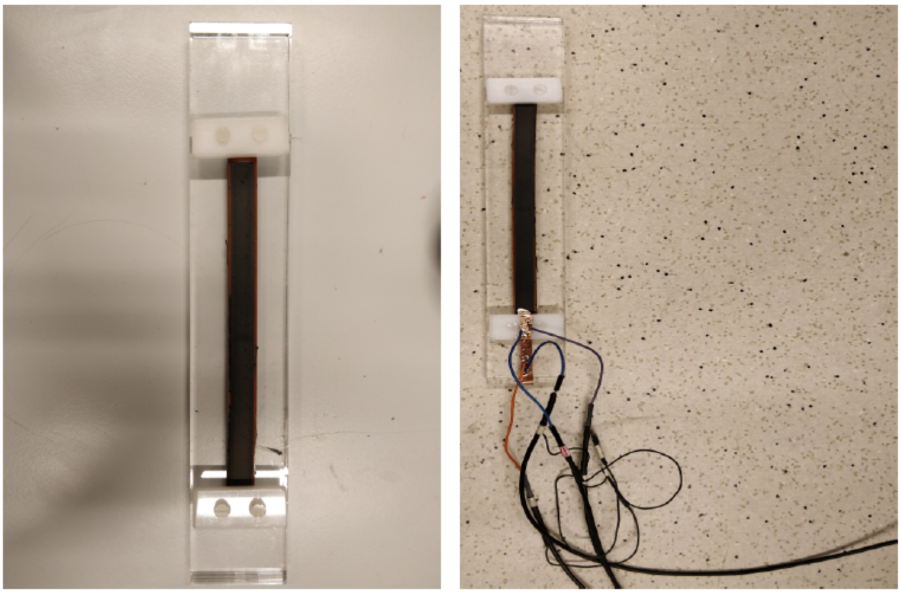

Figure 5.3: Sensor placed on the mount and clamped from both ends for electrical connections to the LCR, courtesy [24].

5.1.1 FlexenStein3D

The setup used to test the sensor was built by combining two 3D printers, a flashforge creator pro movement system [102] and a printer body, as well as a rova3D bed from ORD solutions [103]. A WIFI duet [104] was added to the setup to communicate with it, along with some custom parts. Because of having a lot of elements brought together in parts for a single machine, much like the creator of Frankenstein in Shelley's infamous novel from 1818 'Frankenstein; or, The Modern Prometheus, it was given the name 'FlexenStein3D'. The idea was to attach the linear actuator instead of a nozzle so that it is possible to move the actuator along all three axes. The serial port connects with this set-up at a 57600 baud rate and moves the build plate in the z direction, enough to allow the actuator to extend fully without collision with the test set-up for start-up calibration.

Figure 5.11 shows how these different pieces of equipment are connected. The actuator used here is SMAC and is explained further in the next section.

5.1.2 SMAC actuator

The linear actuator probes the sensor with a compressive force at positions randomly selected on the sensor using a script written in Python. These forces are in the range of 0 N to 6 N, also selected randomly by the script. The SMAC actuator (LCA25-050-15F) [105] is connected as shown in Figure 5.4.

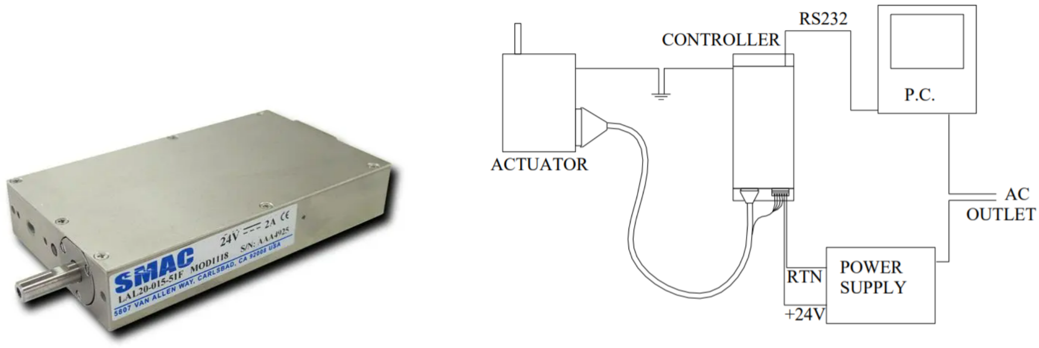

(a) Photograph of the linear actuator [105]. (b) Connections on the SMAC, courtesy [24].

Figure 5.4: SMAC Actuator and its connections.

The linear actuator used is programmable to custom applications, ranging from 5 mm to 150 mm of stroke length or a maximum of 500 N peak force. This peak force value is applied on jerks, and for a consistent force application, like required in this experiment, the actuator can apply the highest force of 13 N. The minimum resolution of the stroke length is 0.1 µm, and its piston weighs 90 g, adding the force of 0.9 N to the applied force. The serial port connects to the SMAC at the baud rate of, 115200 with a Python script to control force.

The potential at which SMAC operates is different from the potential of the sensor being tested. This can cause capacitive coupling in the impedance measurements [106], especially due to the metal tip. Creating a distance between the actuator and the sensor is important to avoid such coupling. For this, a plastic extension was fabricated using 3DP. To give the sensor a more human-like probe, we added a flexible tip to this extension at the point of contact with the sensor. In addition to this, a clamp was designed to hold the SMAC on the FlexenStein3D, as explained later in this chapter.

5.1.3 Extension and Tip Fabrication

To evenly distribute the force, an extension was designed for the SMAC probe. From the extensions designed by Patel in [24], the 'soft tip' was initially used. This was because, although Patel concluded a better response on the sensor by the 'hard tip', the 'soft tip' was more human-like in the form of weight distribution at the point of probe. This is because the flexible part of this tip deforms evenly because of its shape and the pressure is applied evenly on the sensor surface. This tip that contacts the sensor was fabricated using AGILUS30 [107] black flexible Polyjet material. A cover for this tip, that connects the SMAC with it, was fabricated using hard and transparent Veroclear [108] Polyjet material, schematically shown in Figure 5.5.

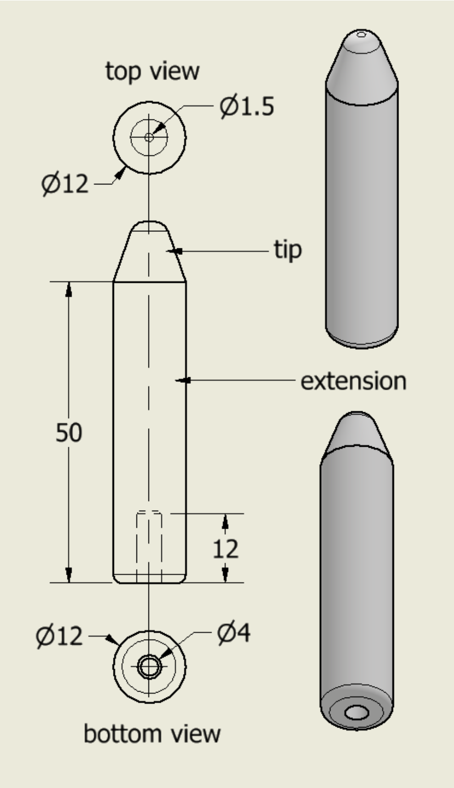

Figure 5.5: New sensor tip designed.

Due to the hollow structure of the Veroclear, the extension kept on breaking, bending, and being detached from the actuator. Electromagnetic interference was also seen in the measurement as electrical noise at the point of the probe. To solve this, a new design was fabricated. The extension was made by 3D printing a stronger polymer than previously used Veroclear, Polylactic Acid (PLA) [109]. This cylinder was printed with one hollow end having an outer diameter of 12 mm and an inner diameter of 4 mm extending the actuator's metal tip. This empty space of 12 mm was threaded and connected to a screw of 5 mm diameter and 15 mm length on the other side to have firm attachment with the SMAC tip as shown in Figure 5.6. The entire extension was designed to be 50 mm in length. The solid part that contacts the sensor is elastic and made of Ninjaflex [110]. It is 10 mm in height and has a flat tip of 5 mm, converging from the edge of the extension. The radius of this entire assembly is 12 mm, and it creates a distance of 52 mm from the metal screw between the SMAC probe and this extension. The entire structure was fabricated using 3DP as two separate parts, since the PLA and Ninjaflex were unable to bond at low temperatures away from the print bed, making it tough for the multi-nozzle H series Diabase printer to print the entire assembly. Loctite 406 instant adhesive was used to glue this assembly.

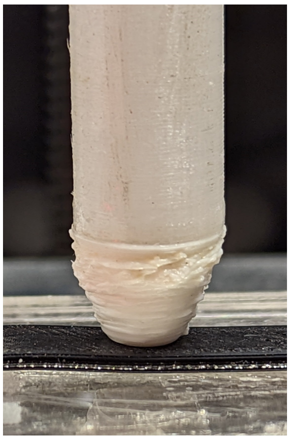

Figure 5.6: Tip attached to SMAC, pressing on the sensor.

5.1.4 Clamp Fabrication

A clamp was designed to hold the SMAC actuator vertically in place at the position where previously the nozzle on the FlexionStein3D had been. It was fabricated using 3DP on a Diabase H series printer using Polylactic Acid (PLA). It serves the purpose of avoiding suspension noise created due to jerks and vibrations developed by the linear actuator, and the FlexionStein3D bed where the sensor is sitting. It was attached to a steel cast to hold SMAC in its place, connected with the clamp with three screws as shown in Figure 5.7. Further, four screws were used to hold the actuator in verticle position as shown in Figure 5.4, Depending on the orientation of the SMAC, interference occurred in the internal coil of the actuator and the screws used to hold it, causing the force to be misapplied.

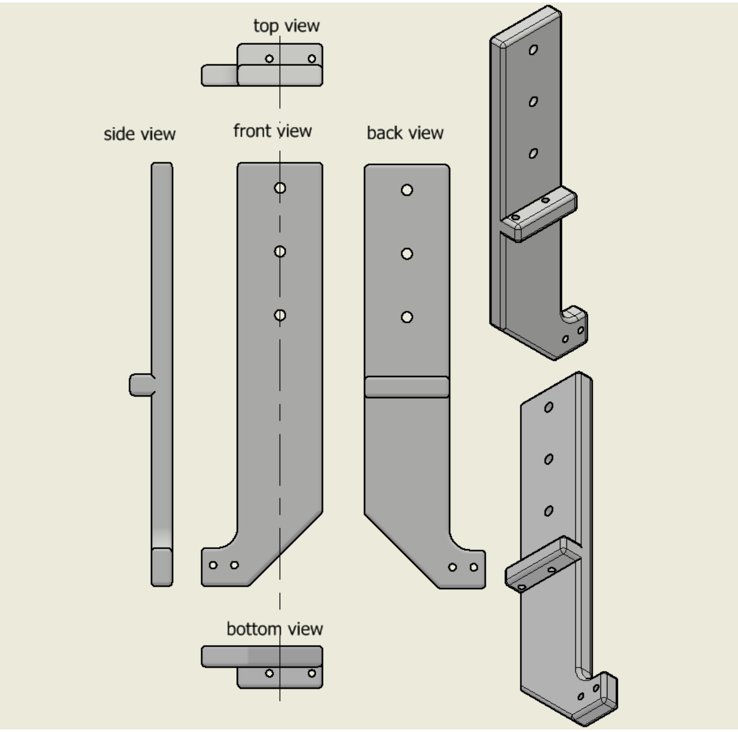

Figure 5.7: Clamp designed to hold SMAC on top of FlexenStein3D.

Figure 5.8: Clamp print to hold SMAC on top of FlexenStein3D.

5.1.5 TiePieLCR

The response of the sensor was determined in terms of changes in the impedance. It was measured with the help of an in-house developed multi-frequency impedance analyser, built by Schouten [21]. The sensor was connected to the analyser, as shown in Figure 5.10. The circuit uses a differential auto-balancing bridge method built using LTC6268 and LTC6268-10 op-amps, combining a high input impedance with a large gain bandwidth. This large bandwidth is advantageous to the measurement, along with the continuous measurement provided. Continuous measurement is possible because the LCR is connected to the Handyscope HS5-540 oscilloscope from 'The unbeatable USB oscilloscope' series by TiePie [111], which generates a harmonic excitation signal at the input voltage V_{in}.

In the measurement, there are real and imaginary components to the measured impedance. In general, the impedance is represented by:

$$Z = R + jX \tag{5.1}$$

Where the reactance, jX, represents the imaginary or 90° out-of-phase component of the impedance, and the resistance, R, represents the real or in-phase part of the impedance. A Python script is used to demodulate the voltage and the current. Figure 5.9 shows the simplified circuit diagram of the TiePieLCR.

The frequency analyser used for the TiePieLCR was designed to visualize the electric signal, as shown in Figure 5.10. Since the circuit uses a Trans-Impedance Amplifier, it is possible to choose a reference signal at L_{POT}, with a gain of $270\,\mu\text{A}\,\text{V}^{-1}$. The scope range was adjusted to avoid clipping and get a clear signal. No Direct Current (DC) offset was used.

Multiple frequencies are used with different weights to get the output. Higher weights are added to the lower frequencies since the sensor is capacitive. The capacitive impedance is

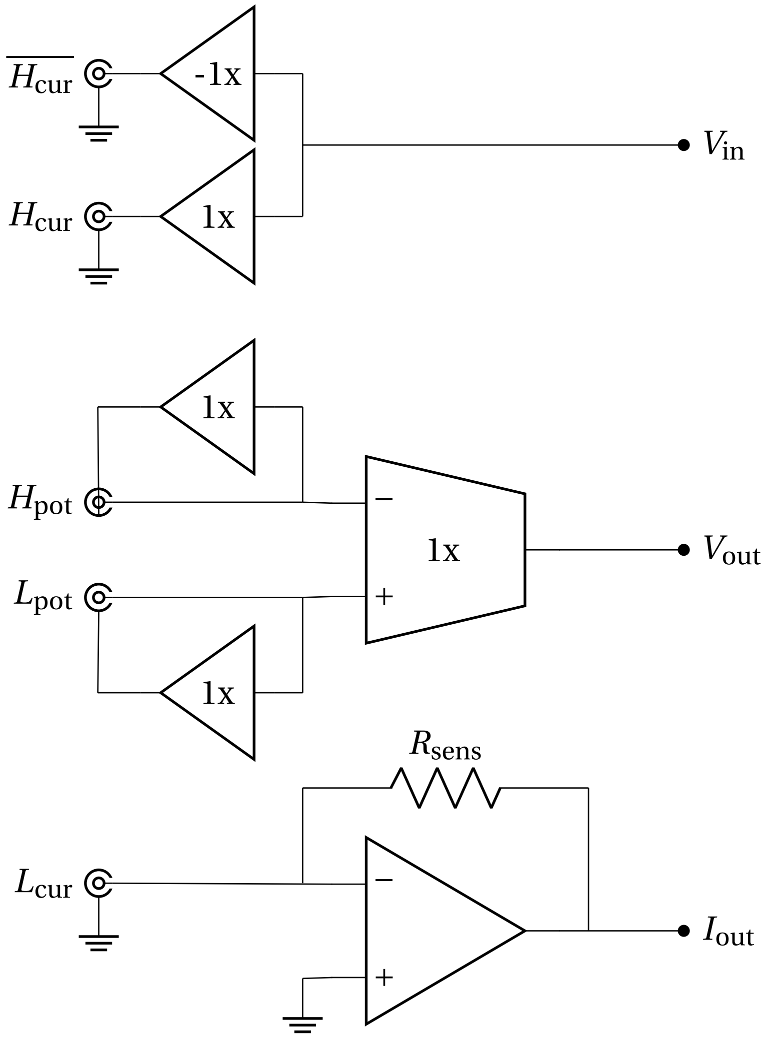

Figure 5.9: Simplified circuit diagram of the TiePieLCR, courtesy [21].

frequency-dependent, inversely proportional to the frequency. These frequencies are used to avoid harmonic interference in the read-out, considering the nonlinearities in the sensor that are not taken into account.

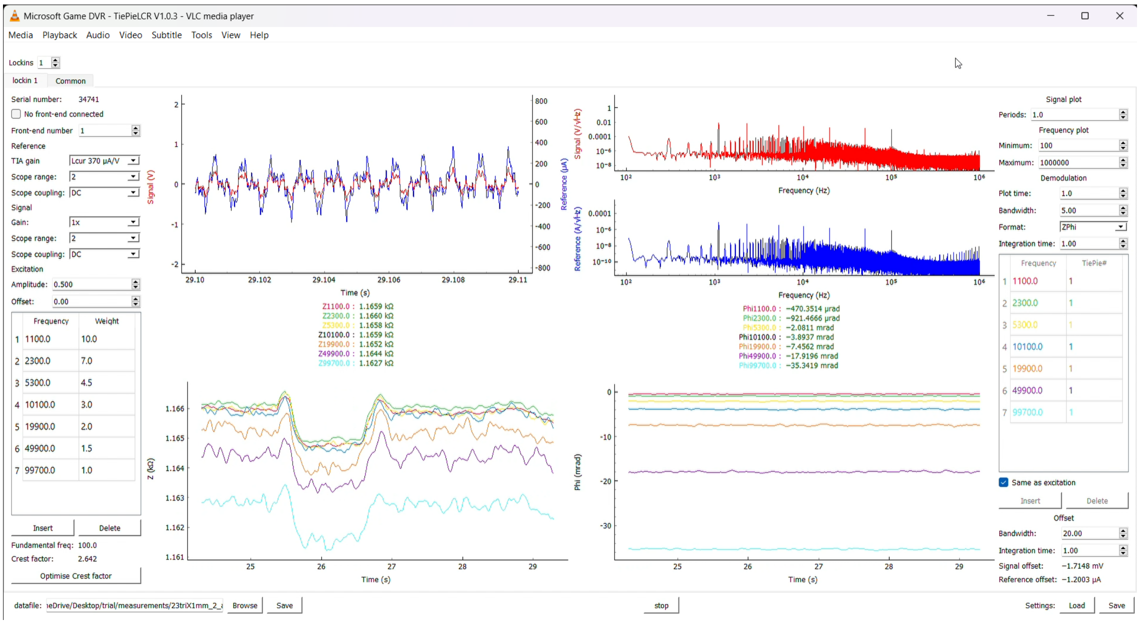

Lockins: 1

Serial number: 34741

☐ No front-end connected

Front-end number: 1

TIA gain: Lcur 370 μA/V

Scope range: 2

Scope coupling: DC

Gain: 1x

Scope range: 2

Scope coupling: DC

Amplitude: 0.500

Offset: 0.00

	Frequency	Weight
1	1100.0	10.0
2	2300.0	7.0
3	5300.0	4.5
4	10100.0	3.0
5	19900.0	2.0
6	49900.0	1.5
7	99700.0	1.0

Fundamental freq: 100.0

Crest factor: 2.642

Z1100.0 : 1.1659 kΩ
Z2300.0 : 1.1660 kΩ
Z5300.0 : 1.1658 kΩ
Z10100.0 : 1.1659 kΩ
Z19900.0 : 1.1652 kΩ
Z49900.0 : 1.1644 kΩ
Z99700.0 : 1.1627 kΩ

Phi1100.0 : −470.3514 μrad
Phi2300.0 : −921.4666 μrad
Phi5300.0 : −2.0811 mrad
Phi10100.0 : −3.8937 mrad
Phi19900.0 : −7.4562 mrad
Phi49900.0 : −17.9196 mrad
Phi99700.0 : −35.3419 mrad

Periods: 1.0

Minimum: 100

Maximum: 1000000

Plot time: 1.0

Bandwidth: 5.00

Format: ZPhi

Integration time: 1.00

	Frequency	TiePie#
1	1100.0	1
2	2300.0	1
3	5300.0	1
4	10100.0	1
5	19900.0	1
6	49900.0	1
7	99700.0	1

☑ Same as excitation

Bandwidth: 20.00

Integration time: 1.00

Signal offset: −1.7148 mV

Reference offset: −1.2003 μA

datafile: ıeDrive/Desktop/trial/measurements/23triX1mm_2_i

Settings:

Figure 5.10: Graphical User Interface of TiePieLCR, courtesy [21].

frequency	weight
1100	10
2300	7
5300	4.5
10100	3
19900	2
4990	1.5
99700	1

Table 5.1: distribution of weights and frequencies used.

5.2 Operation

As shown in fig 5.1, the SMAC actuator is connected with the FlexenStein3D using the clamp. The SMAC is instructed to press down on the sensor that is attached to the bed of Felexenstein with random force values applied on the sensor in the range of 0 N to 6 N at random positions. TiePieLCR is connected to the sensor as an input/output device, that measures voltage and current between its ports, as explained in the previous section.

The observance that previous developments in this project had not examined such random estimation of force and position values to understand the behaviour of this sensor is the basis for choosing the method.

5.3 Data Visualisation

Two different data files were outputted from the experimental data. One was from the TiePie LCR and the other was from the experimental setup including SMAC. Combining these two data files, the set force, set position, real and imaginary impedance values, errors related to them, and timestamps for each measurement, for all 7 frequencies, are obtained. Errors in the measurement were also outputted from the SMAC, and the data was visualised after ignoring the data points with errors. Since both the data sets did not have the same time interval, both the timestamps were synchronized with real time, in seconds.

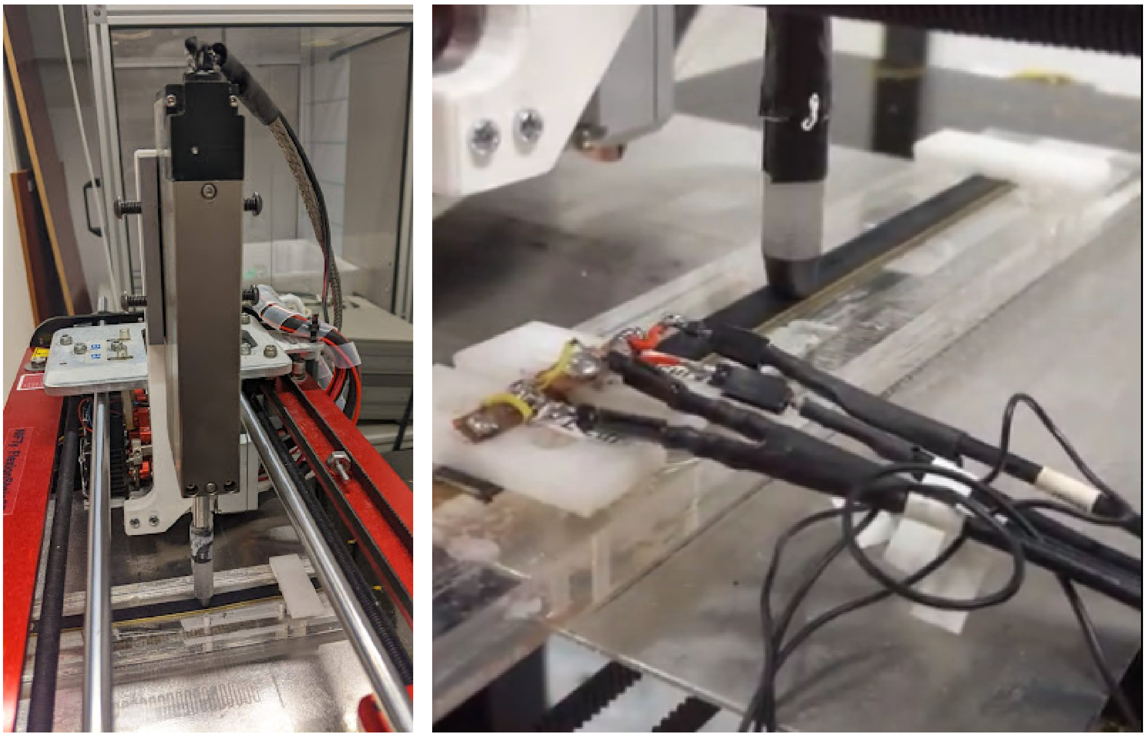

(a) The experimental setup, with SMAC held in place by the SMAC attached to FlexenStein3D using the clamp fabricated.

(b) The experimental setup with the tip of SMAC and sensor mount used to keep the sensor in place on FlexenStein3D bed.

Figure 5.11: Picture of the linear actuator mounted vertically on the steel frame. The actuator applies compressive vertical force on the sensor at different positions. An actuator tip placed on the piston reduces the interference due to capacitive coupling.

A fourth-order low-pass Butterworth filter was designed to remove the noise from the data. The filter uses the 'butter' function by MATLAB, with the sampling frequency of 66.6666 Hz and a cut-off frequency of 0.2727 Hz. The filter is applied to the signal acquired from the LCR, and then, this signal is split into the real and the imaginary part.

5.4 Conclusions

In this chapter, the experimental setup was explained, and all the components used in the setup were introduced thereafter. A 3D printer was modified to do the experiments. An actuator was used to probe the sensor, and a tip and its extension were fabricated to distribute the force evenly and eliminate interference from the actuator probing the setup. A clamp was made to hold the actuator in place, and the LCR used was introduced. The Operation of the experiment process was explained and some information about the visualization and the filtering of the data were described. The results from mathematical, simulation, and analytical models, as well as the fabrication process and the experiments, are described further.

6 Results and Analysis

This section presents the results of the new design addition to the sensor. Initially, the simulation outcomes are presented and analysed, followed by a discussion regarding the outcomes of the new design's fabrication process. Subsequently, the analysis of experimentation results on the new printed sensor designs is conducted.

6.1 Simulation Results

As discussed in chapter 3, two simulation methods were employed. This section introduces all the results found from the models and compares them with the analytical model introduced in the same chapter.

6.1.1 Mathematical model

To understand the sensor's response, the impedance was modelled when applying the force as a function of force and position, modifying the model made by Patel [24]. The sensor model was updated with the parameters mentioned in Table 3.1 and the behaviour was modelled for the multi-frequency approach. The impedance response was split into the real and imaginary parts, giving the values of resistance (R) and reactance (X) respectively. Figure 6.1(a) shows the dependence of the resistance, or the real part of the impedance on the force and position of the applied force, for the frequencies used in the experiments. Similarly, Figure 6.1(b) shows the dependence of the reactance, or the imaginary part of the impedance on the force and position of the applied force, for the frequencies used in the experiments.

From Figure 6.1, it is visible that the response of resistance and reactance are dependent on both, force and the position of the force application. At lower frequencies, these outcomes are redundant from the measurement results from previous work, where a clear dependence of the reactance and the force was determined, while a dependence of resistance was determined on both the force and the position of the application of force.

There is a significant difference in the response of the sensor as the frequencies are increased. At higher frequencies, both-resistive and reactive components of the impedance influence the measurement of both, force, and the position of the force application.

This is contrasted by the findings of the previous work [24], where Patel found the resistive components to be influenced by both, the force and position measurement, but where the capacitive component was merely influenced by the position measurements. At lower frequencies, the hypothesis made is deemed true; but as the frequencies increase, an influence of the reactive component is also visible in the force measurement. In this project, the reactive components are accounted for instead of the capacitive readings made in the previous work. Reactance is inversely proportional to capacitance, as mentioned in equation 2.24, and in section 2.6.

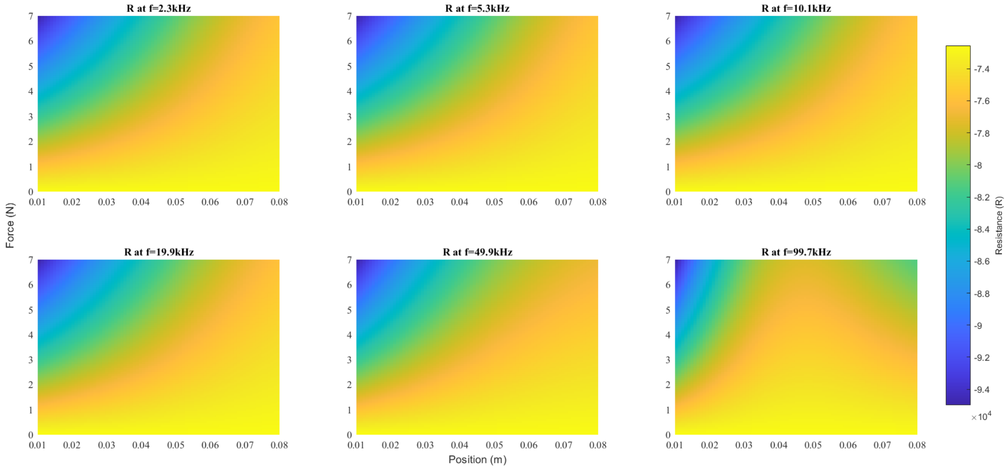

(a) Real part of the impedance (resistance R) from the mathematical model.

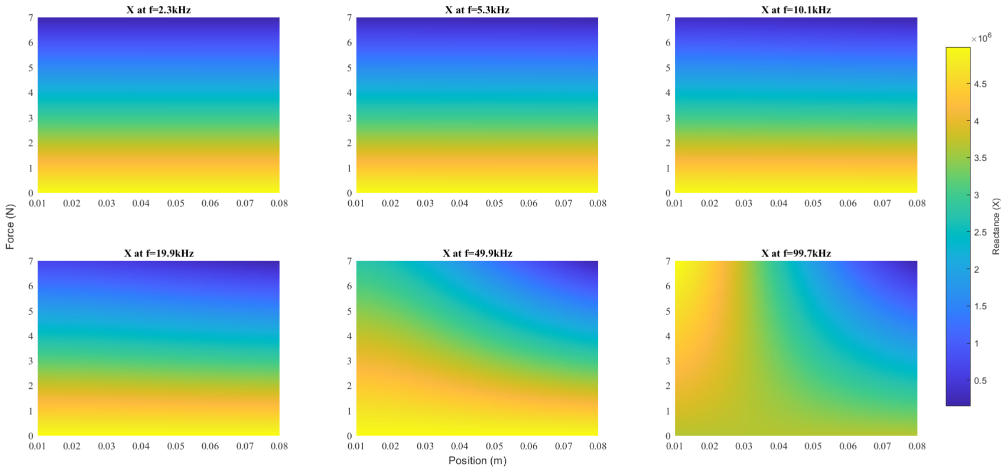

(b) Imaginary part of the impedance (reactance X) from the mathematical model.

Figure 6.1: Impedance (Z) response of the sensor with parameters in table 3.1, for different frequencies.

To understand the sensitivity, the dependence of the change in impedance on the force and position was modelled. Figure 6.2(a) shows the change in real values of impedance-resistance for a unit change in position, and Figure 6.2(b) shows the change in real values of impedance-resistance for a unit change in force. Figure 6.3(a) shows the change in imaginary values of impedance-reactance for a unit change in position, and Figure 6.3(b) shows the change in imaginary values of impedance-reactance for a unit change in force. It is visible from these figures that using a multi-frequency approach is helpful as at different frequencies, there is a varying dependence of the force as well as the position of the sensor on both, the reactance and the resistance. Since the difference in response was not substantial, only six of the used seven frequencies are used in the models of this report.

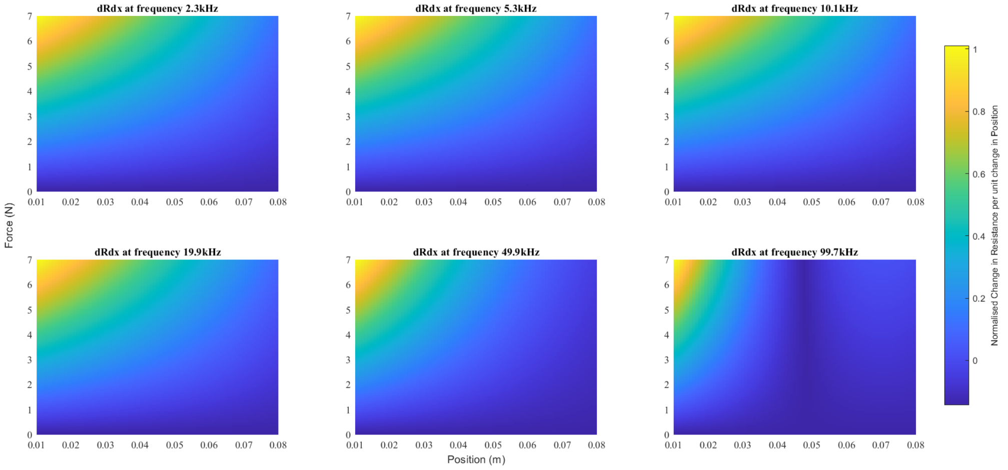

(a) Change in real impedance (resistance R) per unit change in Position.

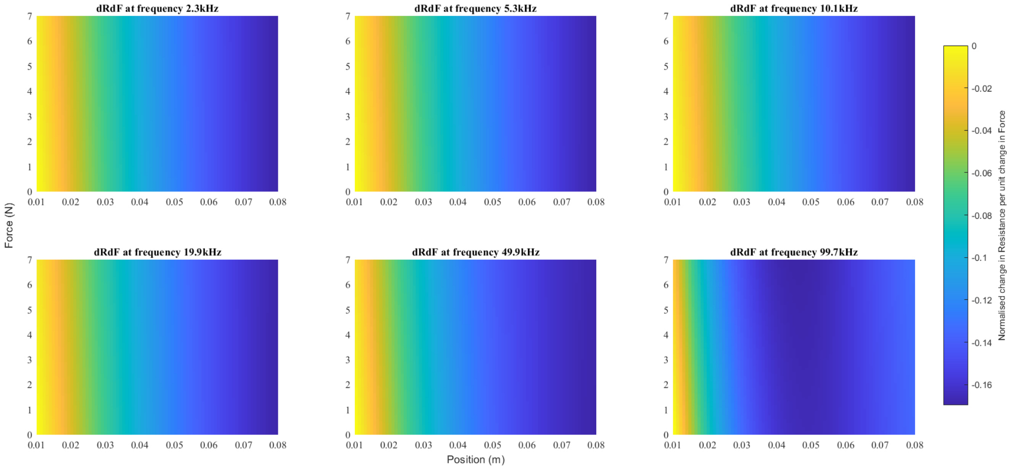

(b) Change in real impedance (resistance R) per unit change in Force.

Figure 6.2: Sensitivity of the simulated sensor: change in resistance (ΔR), for different frequencies.

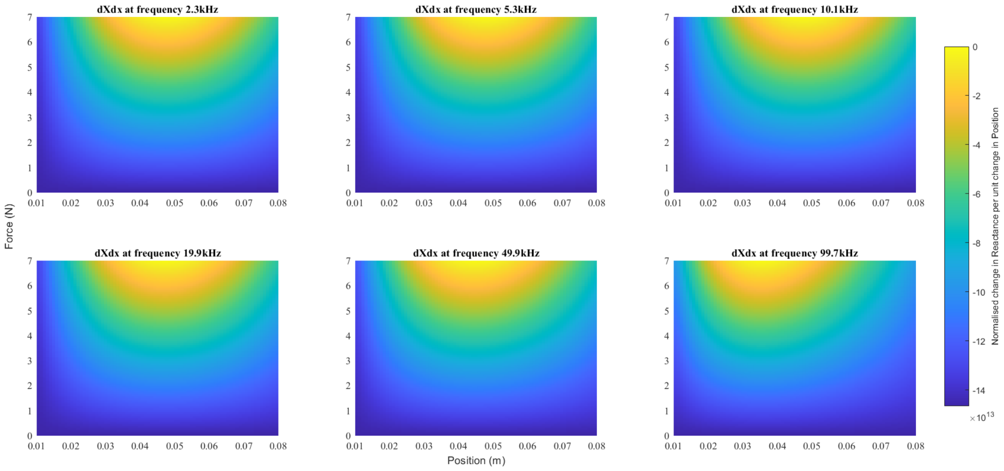

(a) Change in imaginary impedance (reactance X) per unit change in Position.

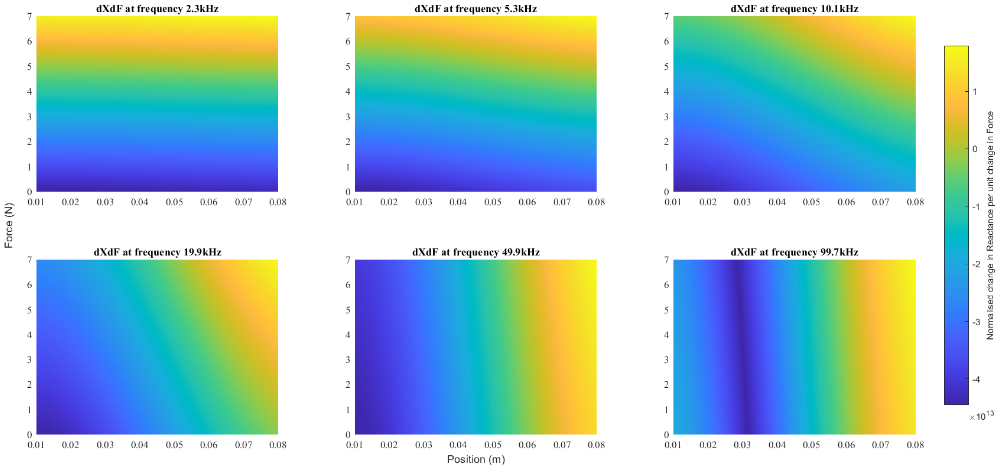

(b) Change in imaginary impedance (reactance X) per unit change in Force.

Figure 6.3: Sensitivity of the simulated sensor: change in reactance (ΔX), for different frequencies.

To understand the operational range of the sensor, an inverse model was created, modifying the inverse model made by Patel [24]. The sensor model was updated with the parameters mentioned in Table 3.1 and the behaviour was modelled for the multi-frequency approach. Figure 6.4(a) shows the range of position measurements, mapped from the sensor output of resistance and reactance measurements, at various frequencies used during the experiments. Figure 6.4(b) shows the range of force measurements, mapped from the sensor output of resistance and reactance measurements, at the same frequencies. The resistance value, at the x-axis is the real part of the impedance measurement, and the y-axis shows the imaginary, phase-shifted part of the impedance response.

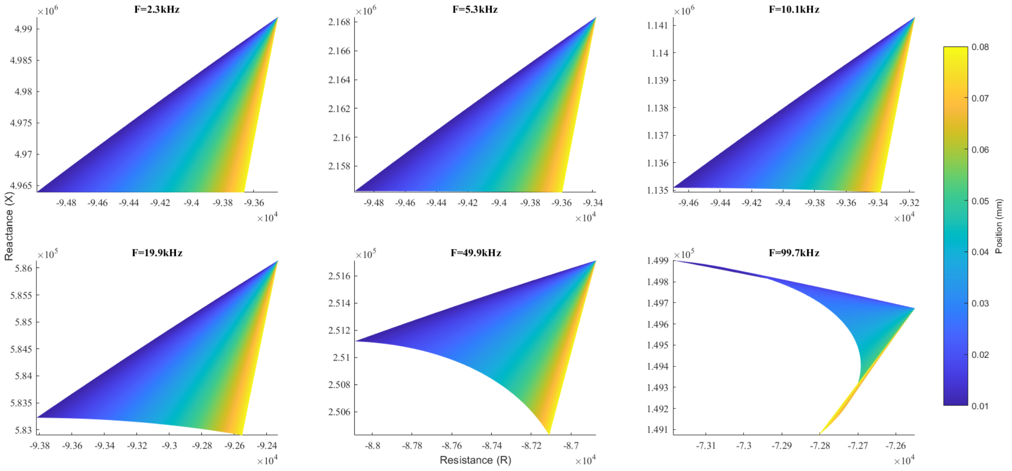

(a) Range of position values in terms of resistance R and reactance X.

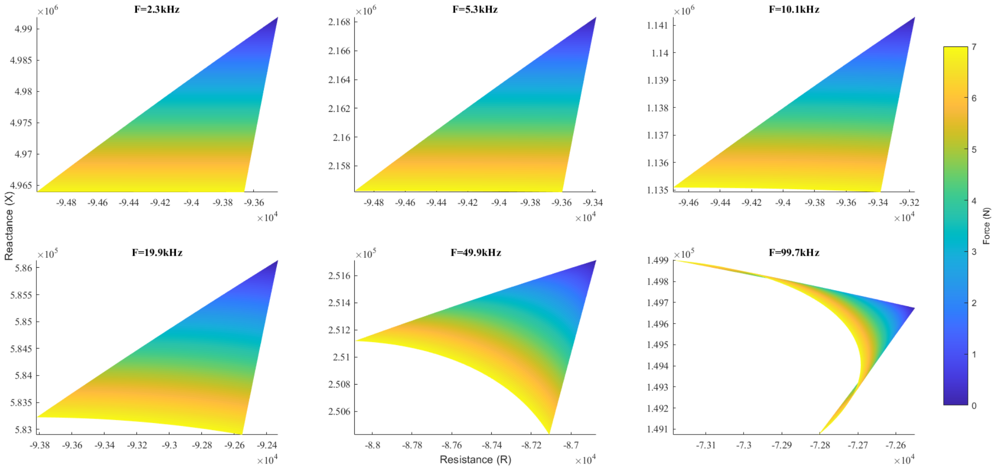

(b) Range of force values in terms of resistance R and reactance X.

Figure 6.4: Inverse model of the simulated sensor, for different frequencies.

It is visible from these figures that lower frequencies are more accurate to measure the force, and the position of the force applications, but as the frequencies increase, the range of measurement becomes smaller.

6.1.2 FEA Simulation

As explained in section 3.1.2, four different Finite Element Analysis (FEA) models were developed. Their results are presented in the section. FEA models were made in COMSOL Multiphysics. The physics of Solid Mechanics and Electrostatics were added. A stress of the range $0\,\mathrm{N\,m^{-2}}$ to $1 \times 10^{5}\,\mathrm{N\,m^{-2}}$ was applied in the negative Z direction and the deformation of the structure was visualised. The movement of the sensor design was restricted in the X and Y directions and the geometry was free to move in the Z direction. The response is discussed in the following section.

Triangular Design

Figure 6.5(a) shows the output of the FEA simulation made on the model shown in Figure 3.1. The deformation is scaled to a factor of 3. The highest displacement within the structure is observed at the centre of the design, although the expected displacement is at the air gap. This effect is because the periodic conditions added at the edges constrain the structure. 0.035 mm of deformation is seen in the structure. To test the limits of the structure, the parametric sweep was performed for exponential stress values, and Figure 6.6 shows the deformation of the sensor structure before errors start to occur. It is found that the maximum displacement is again at the centre, where the deformation of the structure is visible, although the air oozes out completely from the air gap. From the figure, it is safe to assume that all the air is leaving the structure, but the physics does not allow huge deformations to occur within the structure without errors. Figure 6.11(a) shows the displacement within the structure when the geometry is not constrained from the X and Y directions. Deformation in the 0.075 mm is seen in that case, which is more than double the measurement seen in the same structure with constraints assumed due to the property of periodicity in the structure.

Figure 6.5(b), shows the distribution of electric potential, ranging between the voltage applied between the electrode terminals. The arrows show the direction of the electric field. Not all the fields are in the Z direction, showing the limits of the assumptions made for the analytical model, seen in Figure 6.12 and discussed later in this chapter.

The response is discussed further in the next part. A change in capacitance as well as the change in dielectric layer height does not vary as expected, and thus, a new model was designed using FEA in COMSOL Multiphysics. Instead of using Solid Mechanics physics, the geometry of the structure was varied by changing the angle between two points in the geometry, over a constant radius, simulating the shrinking of the air gap, and keeping the volume of all components constant. Figure 6.7 shows the electric potential as well as the direction of the electric field in this model.

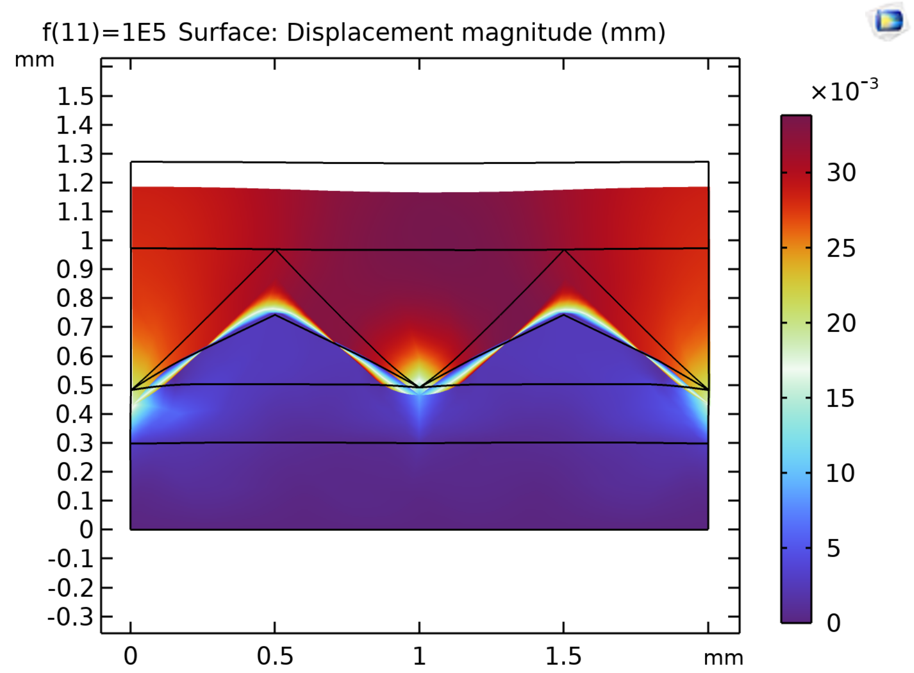

(a) Deformation of the structure, scaled by a factor of three.

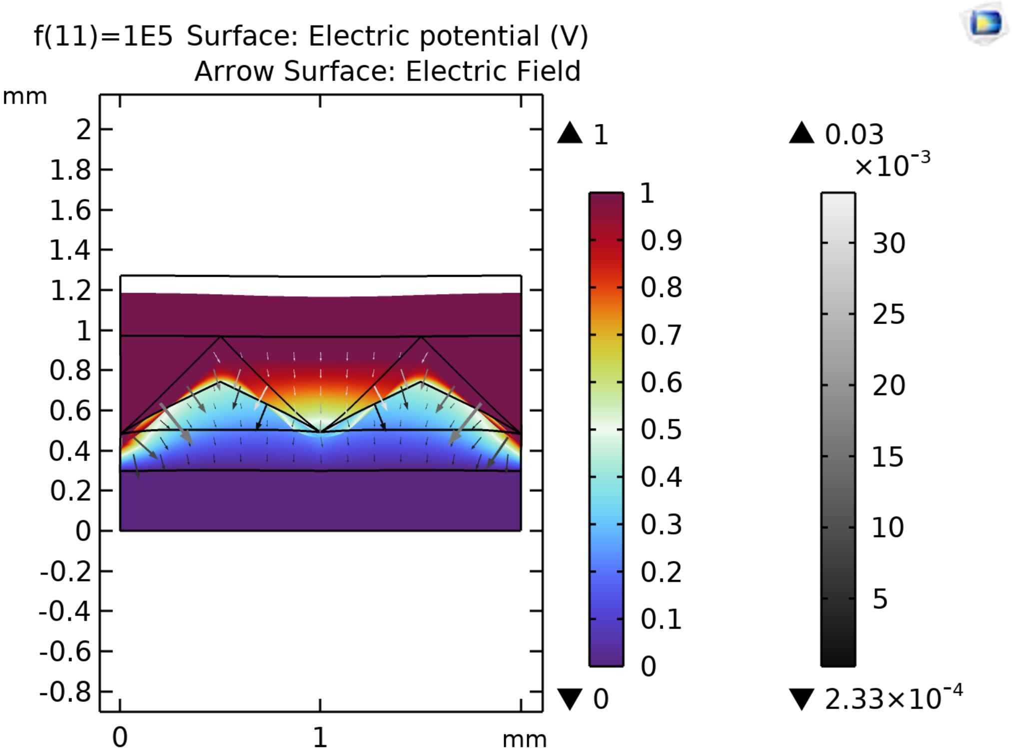

(b) Electrical potential distribution and the direction of electric fields for the model.

Figure 6.5: FEA results showing the mechanical deformation and electrical potential distribution under a load of $1 \times 10^5\,\mathrm{N\,m^{-2}}$, for the model made in COMSOL Multiphysics using Solid Mechanics and Electrostatics physics.

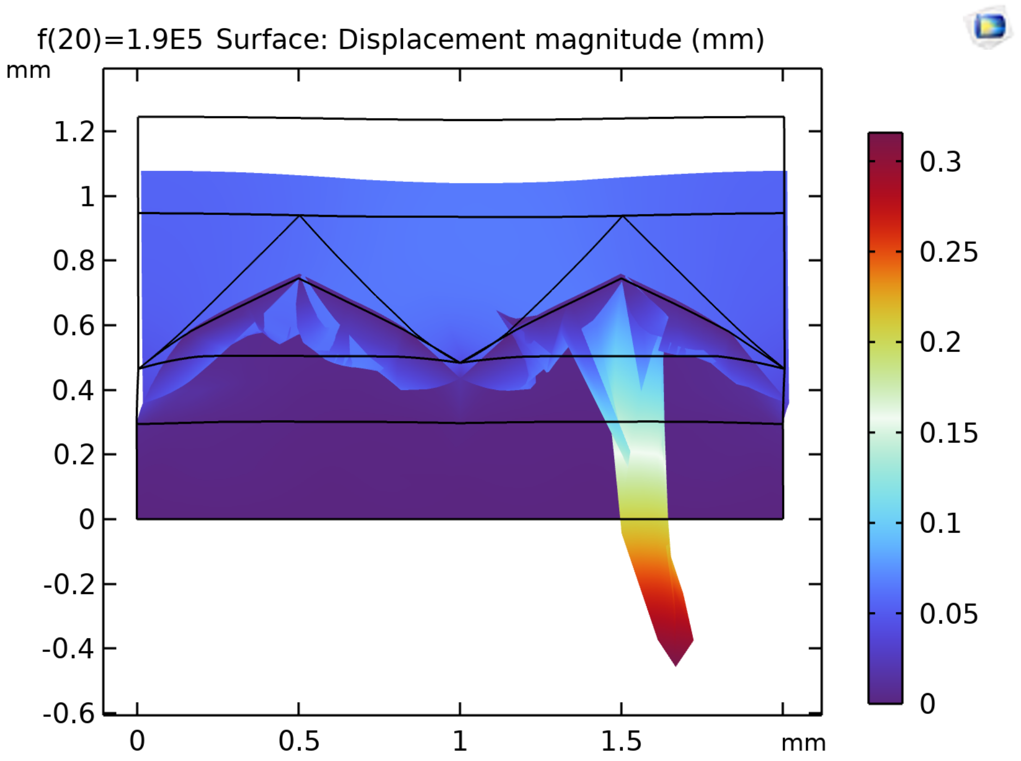

Figure 6.6: Deformation of the structure under the stress of $2 \times 10^5\,\mathrm{N\,m^{-2}}$, scaled three times.

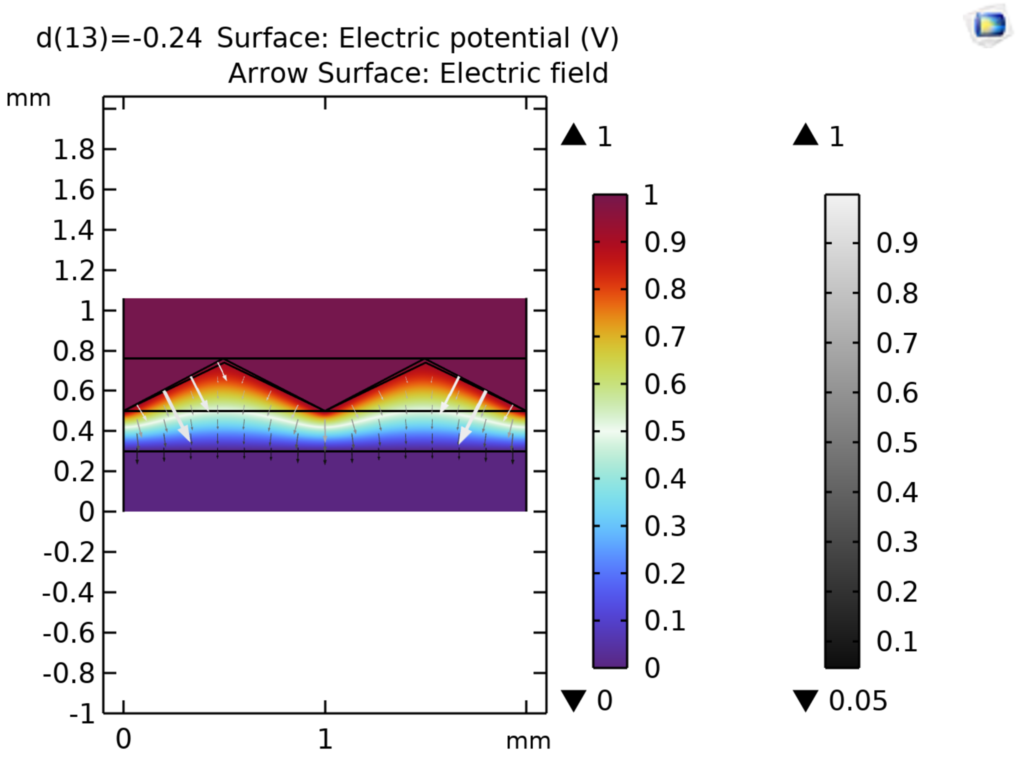

Figure 6.7: Electric potential distribution and the direction of electric fields for the model made by manually changing the dimension of the components.

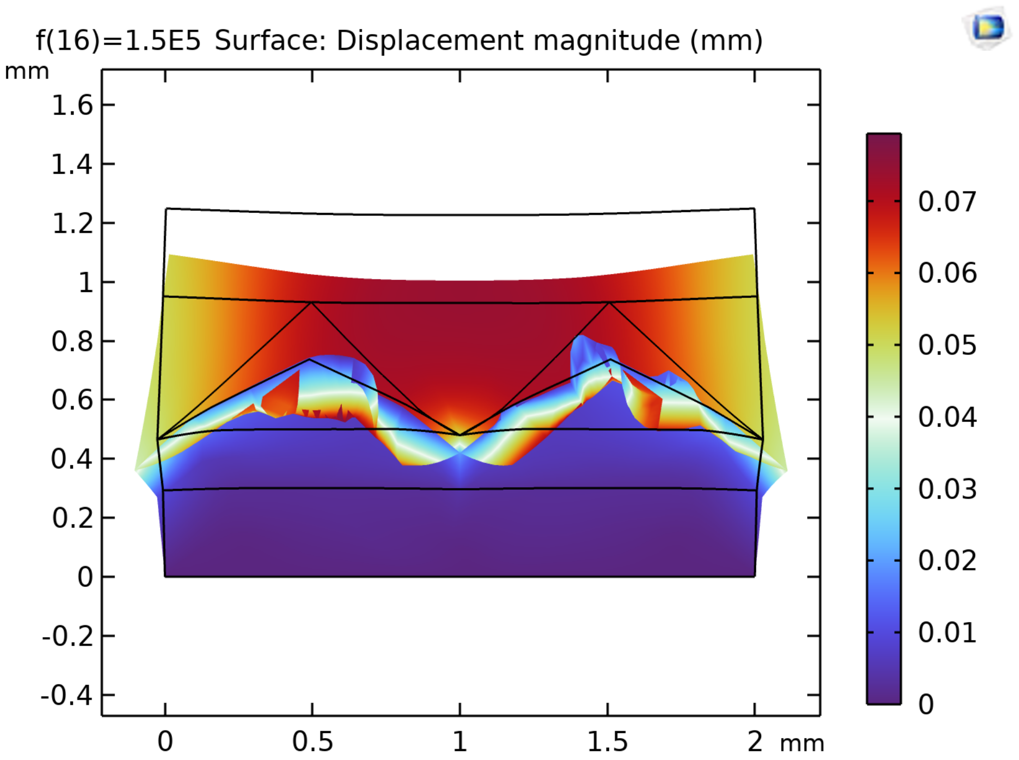

(a) Deformation of the structure, for the triangular model without constraints, scaled by a factor of 3.

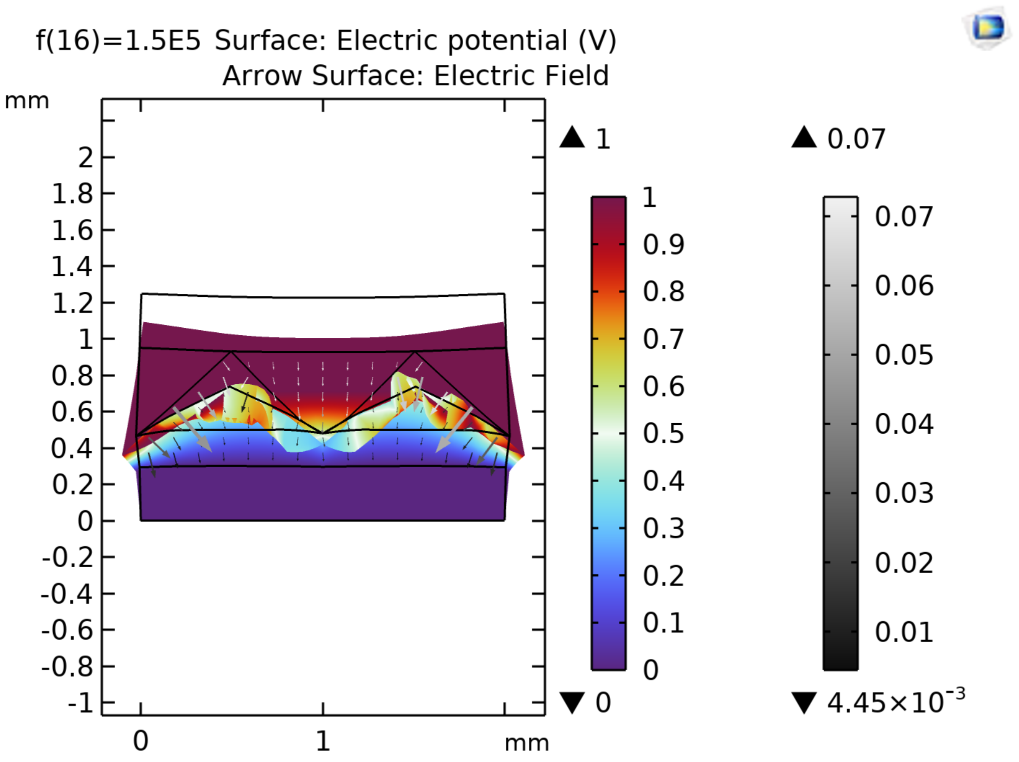

(b) Electrical potential distribution and the direction of electric fields for the triangular model without constraints, along with displacement scaled by a factor of 3.

Figure 6.8: Deformation of the structure, for the triangular model without constraints, scaled by a factor of 3.

Rectangular Design

Figure 6.9(a) shows the output of the FEA simulation made on the model shown in Figure 3.3. The deformation is scaled to a factor of 30. The highest displacement within the structure is also observed at the centre of the design, similar to the triangular design, as the periodic conditions added at the edges constrain the structure. 7.5×10^{-3} mm of deformation is seen in the structure, which is considerably smaller than the deformation seen in the triangular design. The constraint on this model is applied from both X and Y directions, and the structure is a square of 1 mm, unlike the triangular design, where the structure is a 10 mm long and has the width of 2 mm.

Figure 6.9(b), shows the distribution of electric potential, ranging between the voltage applied between the electrode terminals. The arrows show the direction of the electric field. Even in this model, the fields in not distributed in the Z direction only.

Since this model did not respond as expected as well and thus, a new model was designed using FEA in COMSOL Multiphysics. Instead of using Solid Mechanics physics, the geometry of the structure was varied by changing the height and the width as a factor of the height of the air gaps in the geometry, simulating the shrinking of the air gap, and keeping the volume of all components constant. Figure 6.10(a) shows the deformation in the model's geometry to be not more than 0.2 mm, and Figure 6.10(b) shows the electric potential as well as the direction of the electric field in this model.

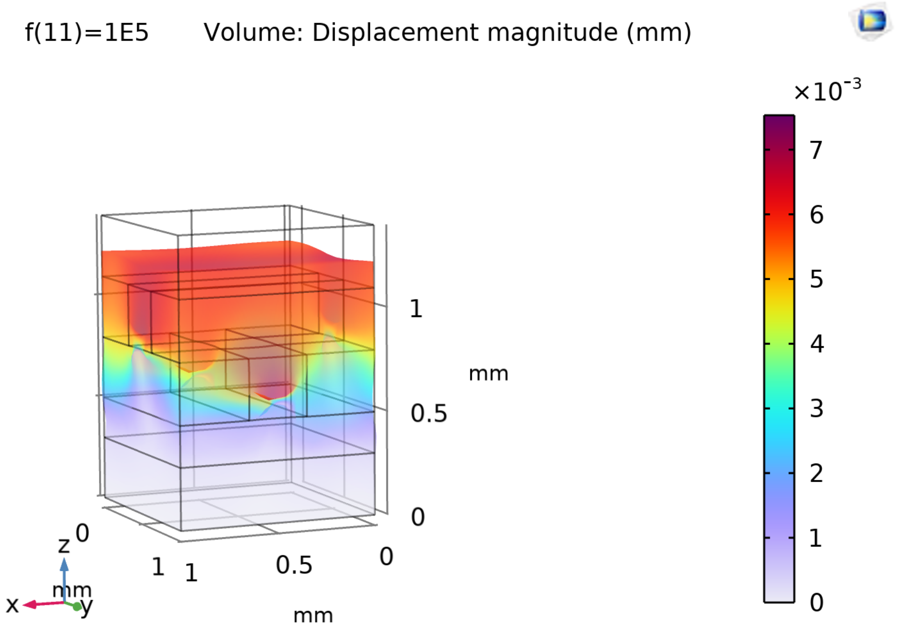

(a) Deformation of the structure, scaled by a factor of 30.

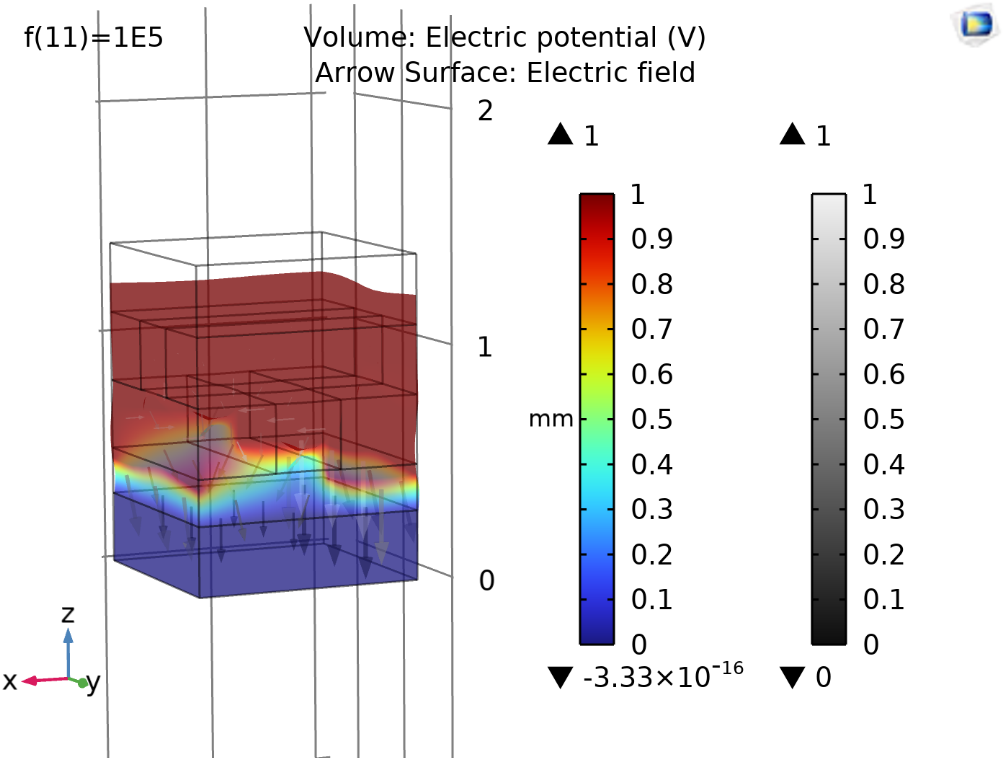

(b) Electrical potential distribution and the direction of electric fields for the model.

Figure 6.9: FEA results showing the mechanical deformation and electrical potential distribution under a load of $1 \times 10^5\,\mathrm{N\,m^{-2}}$, for the model made in COMSOL Multiphysics using Solid Mechanics and Electrostatics physics.

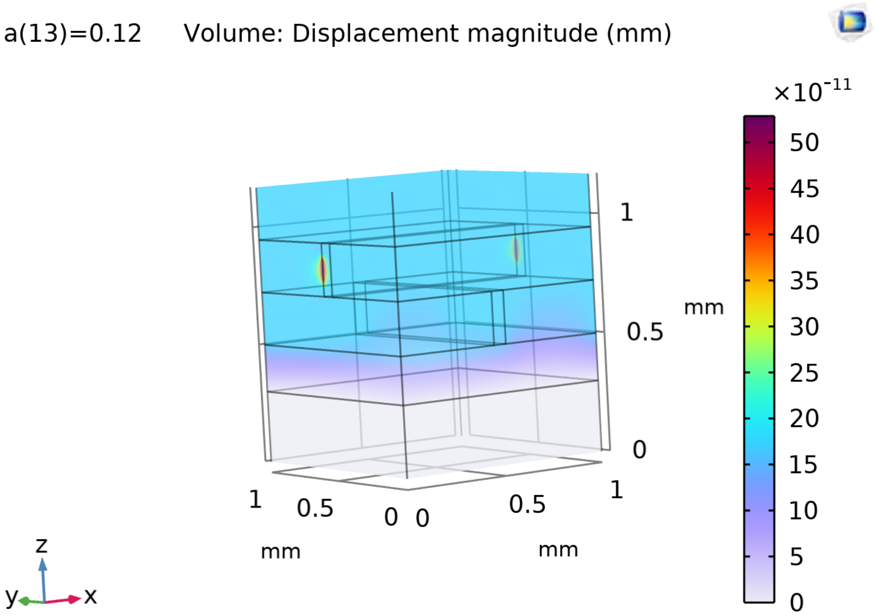

(a) Deformation of the structure, scaled by a factor of 30.

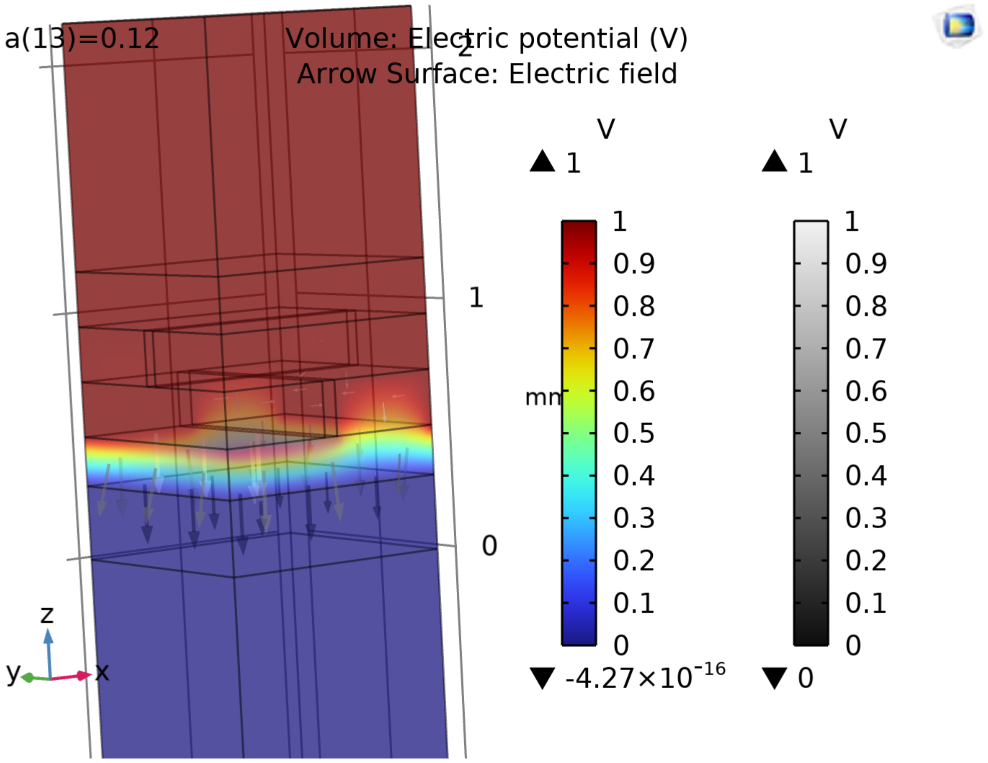

(b) Electrical potential distribution and the direction of electric fields for the model. The red box on top of the structure is air. The blue box at the bottom of the structure is also air, polarized by the electric field.

Figure 6.10: FEA results showing the mechanical deformation and electrical potential distribution under a load of $1 \times 10^5\,\mathrm{N\,m^{-2}}$, for the model made in COMSOL Multiphysics for the model made by manually changing the dimension of the components.

Since the voltage applied on the top electrode was 1 V and the bottom electrode was grounded, the potential difference between the electrodes can be considered unity. From the equations below,

$$q = Cv \tag{6.1}$$

Since

$$v = 1 \tag{6.2}$$

$$q = C \tag{6.3}$$

The charge can be taken as the capacitance in the structure for the FEA models. The analytical model discussed in section 3.2 outputs the graph shown in Figure 6.12(a) for the triangular design in blue colour. Change in the dielectric layer of the model in COMSOL Multiphysics was obtained by a global evaluation of distance measurement between the points in the model that had all layers of dielectric X60. As seen in the figure, the result of the first FEA model made in COMSOL with stress application is very restricted. The change in capacitance is much larger for the respective change in the height of the dielectric layer. As the stress was increased in the model over the values of $1 \times 10^5\,\mathrm{N\,m^{-2}}$, as shown in Figure 6.6, the slope of the line stayed the same, but because of the breakage in the structure simulated, there were irregularities in the obtained results. This indicates that, in contrast to the other two lines, which both depend on a change in the air gap's size to alter the capacitance of the entire structure and thus omit the force's effect on the dielectric X60 layer, a greater change in capacitance was seen for a relatively small change in the dielectric's height.

It is safe to assume the slope of the real graph would be more similar to the first model made in COMSOL using Solid Mechanics, than the ones plotted to understand the influence of the added air gap in the model, giving the change in capacitance to be in the range of approximately 10 pF, when projected. To compare this quantity with the model in previous work, devoid of the added electrode extension and air gaps. The response of the model in Figure 6.11(a) can be used. The charge on the electrode was found to be approximately 1 pC, corresponding to 0.01 pF of capacitance from the equation 6.1.2. This gives around10 % increase in the sensitivity of the capacitive measurement.

Figure 6.12(b) shows the change in capacitance for the rectangular design in blue colour. Like in the triangular design, the change in the dielectric layer of the model in COMSOL was obtained by a global evaluation of distance measurement between the points in the model that had all layers of dielectric X60. As seen in the figure, the result of the first FEA model made in COMSOL with stress application is even more restricted than in the triangular design. The change in capacitance is much larger for the respective change in the height of the dielectric layer. Because of the breakage in the structure simulated, there were irregularities in the obtained results for the values of stress over 1×10^5 newton/m^2. For the response of the FEA model by manually changing the geometry of the components, the response is not followed in the Analytical model, unlike in the triangular design. This might be because of the constraints in electrostatics as explained in this section before, as the physics constrains the geometry in the X and Y directions, also seen in Figure 6.11(b). This is because of the high value of nearly 0.5 of Poisson's ratio of both X60 and eTPU. The range of change in capacitance is less, even less than 1 pF, as compared to the change of 10 pF observed in the triangular design.

From the Figure 6.11(b), the charge on the electrode was found to be approximately 0.01 pC, corresponding to 0.01 pF of capacitance from the equation 6.1.2. This gives around 100 % increase in the sensitivity of the capacitive measurement for the 1 mm x 1 mm grid of sensor.

To test the designs, CAD models were built and fabricated using FDM/FFF. The next section discusses the results of this fabrication process.

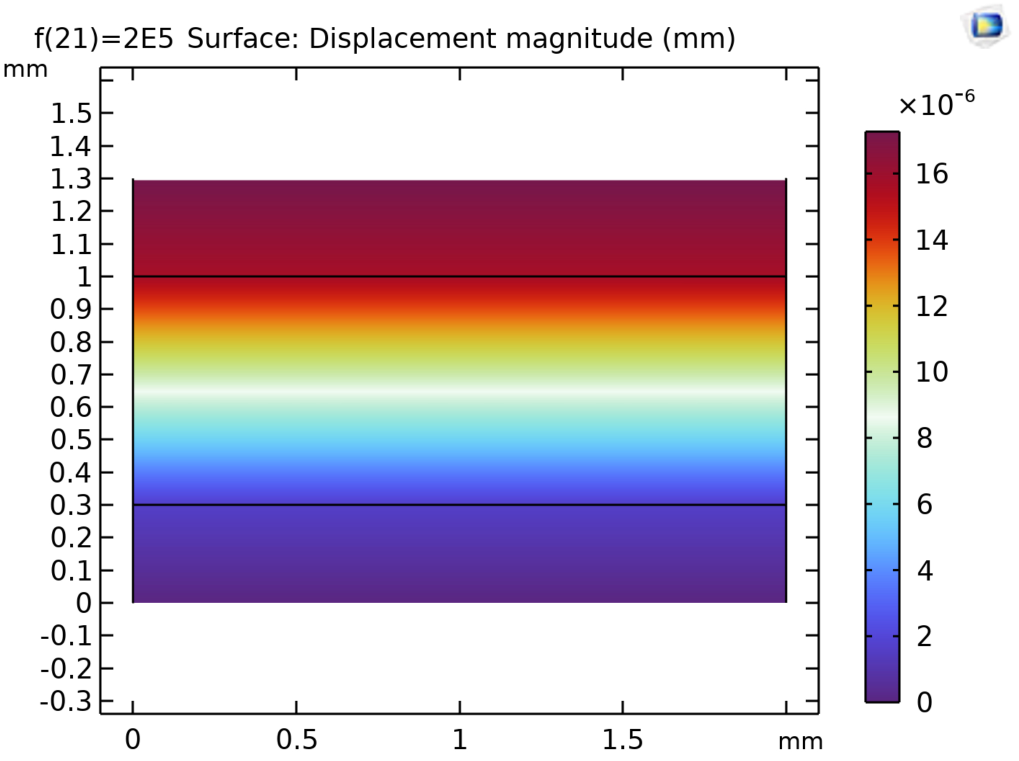

(a) Displacement magnitude, scaled with the factor of 3, for the 2D FEA model.

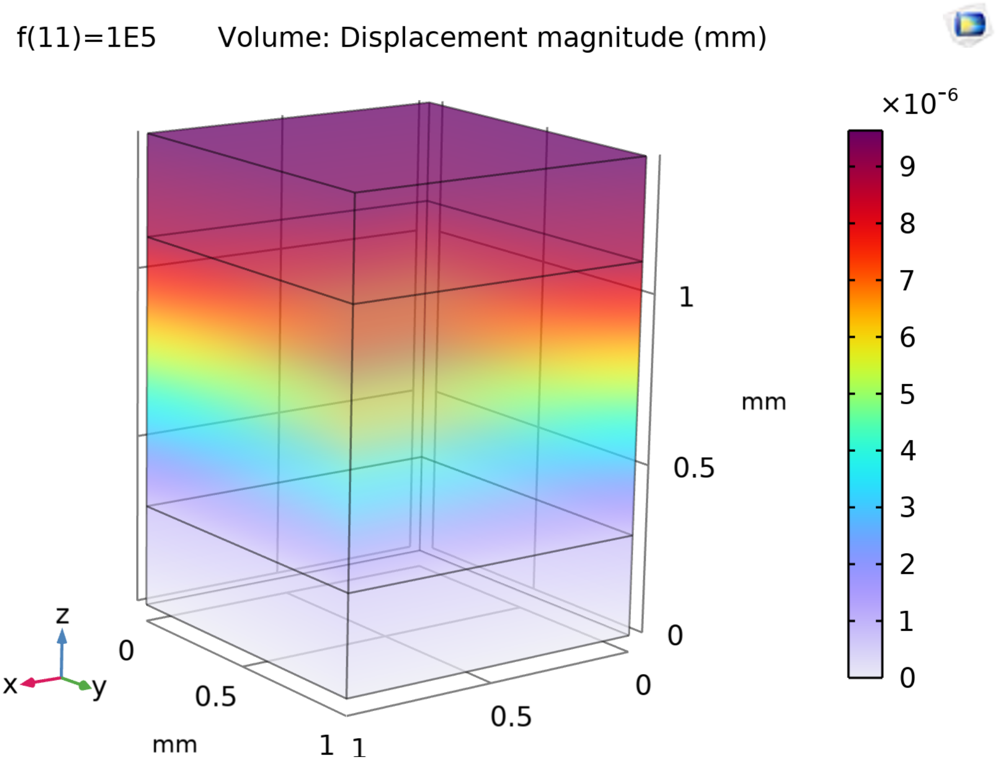

(b) Displacement magnitude, scaled with the factor of 30, for the 3D FEA model.

Figure 6.11: Volume displacement in the model made from the previous work made by Patel [24] without artefacts.

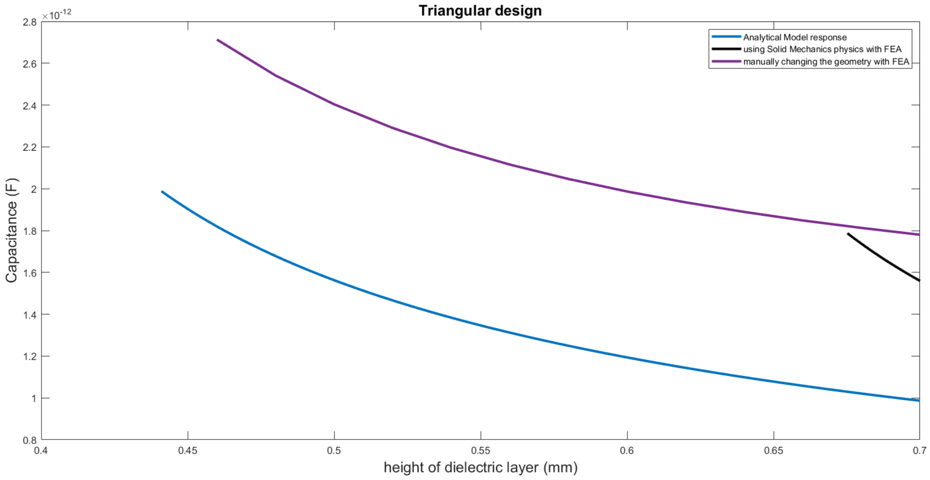

(a) Charge on electrode versus change in height of the dielectric layer of Triangular design.

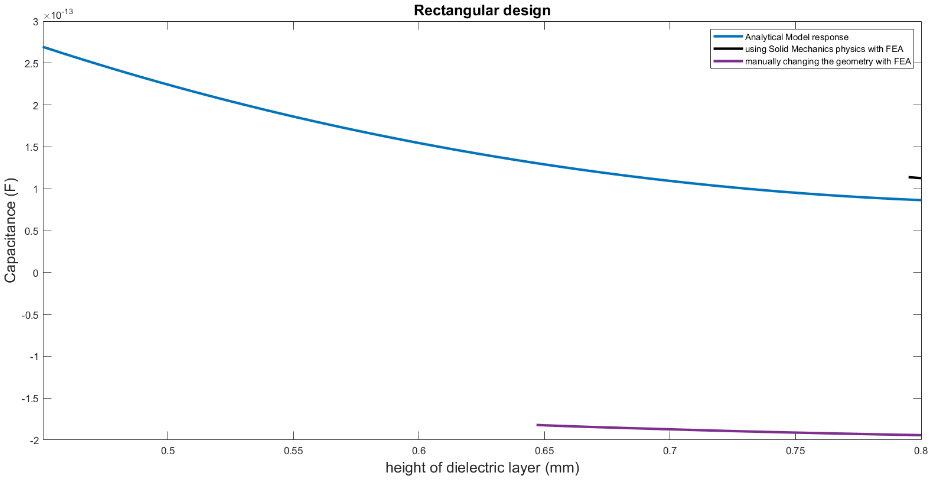

(b) Charge on electrode versus change in height of the dielectric layer of Rectangular design.

Figure 6.12: Charge on electrode versus change in height of the dielectric layer, compared over simulated results.

6.2 Fabrication Results

As mentioned previously in chapter 4 section 3.3, the parameters of the artefacts in the design, such as the frequency, the height, and the width of the cogs as well as the air gaps were determined by the printing capabilities of the printer, the nozzle used as well as the behaviour of the materials used when printed. Figure 4.1 shows the print results for the case where there was no support for the top electrode to be printed on. Creating support using BVOH or any other soluble material was not useful because this problem was experienced through the post-processing stage, explained in section 4.2.7. Many other issues were faced while printing eTPU, as seen in Figure 4.4. Figure 6.13 shows some failures encountered when printing the entire sensor.

(a) Sensor misprint before top layer is printed.

(b) Various types of issues on the printed sensors.

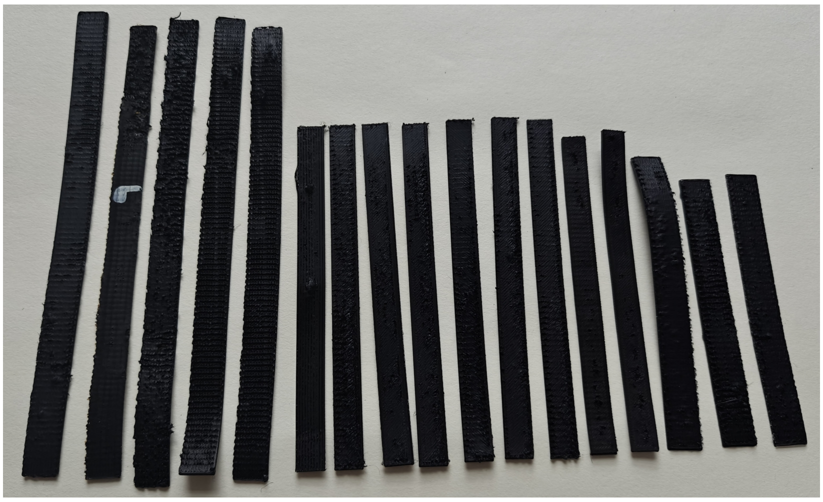

(c) Sensors with top layer not printed over airgaps.

(d) Sensors with holes on the top layer, because of under-extrusion [112].

Figure 6.13: Different types of failures in 3D printing.

During the printing process, eTPU filament emitted fumes as it passed through the nozzle, which is an indication of moisture content in the filament [112]. This occurrence is common when TPU has been exposed to ambient humidity for an extended period. To mitigate this issue, it is crucial to thoroughly dry the filament before use. While drying parameters, such as temperature and duration, can vary based on the filament type and the amount of moisture absorbed, a general recommendation is to dry the filament in an oven or filament dryer, often at around 70 °C for approximately five hours. However, achieving optimal dryness may require trial and error, as no definitive methods exist to measure the exact moisture content. Ensuring the filament is properly dried before extrusion is essential to prevent clogging and other moisture-related issues during the printing process [113]. In this project, no pre-processing had taken place, which resulted in the nozzle clogs during printing, as shown in Figure 6.14, giving print results as seen in Figure 6.15.

In addition to TPU's hygroscopic characteristic, several additives are added to the virgin TPU material to modify its elastic characteristics as well as homogeneously dope it with carbon nanoparticles. These additives range from wax-like external lubricants that are used to avoid friction with the equipment used for the processing, internal lubricants that are used to ensure homogeneous processing, stabilizers and other processing aids that are necessary fillers for changing the intrinsic properties of TPU, like hardness and elasticity. These additives have varied life spans, subjected to exposure to temperature changes, moisture and also time.

(a) Nozzle clog experienced while printing the support material, BVOH.

(b) eTPU clogged around the nozzle after printing BVOH.

(c) eTPU clogging the nozzle while printing bottom layer.

Figure 6.14: Nozzle clogs

(a) Issues in printing the top layer.

(b) Issues in printing the top and middle layers.

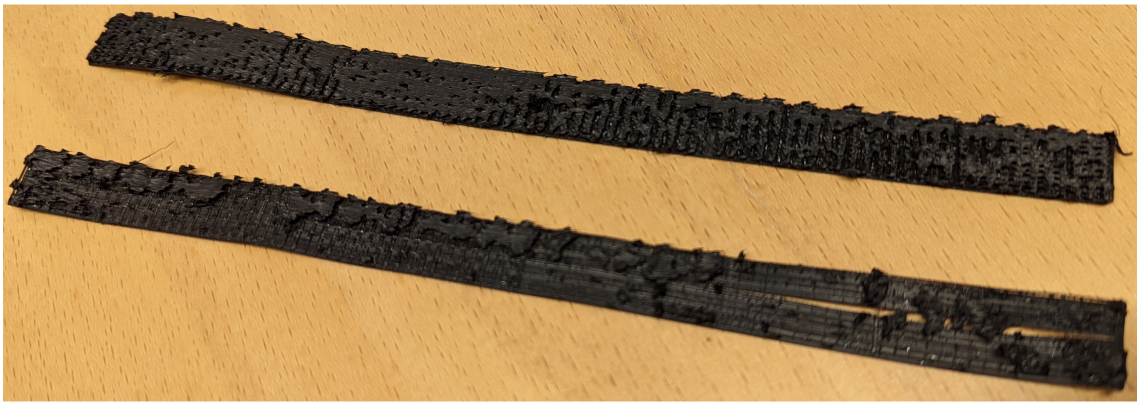

(c) Issues in printing the layers.

Figure 6.15: Different issues while 3D printing the sensor.

(a) Dielectric layer printed.

(b) Inconsistent print in internal layer.

(c) Zits seen on the top layer because of misprints in the internal layers of the sensor.

Figure 6.16: The printing of dielectric, and the resultant prints with zits on them.

X60 filament was easier to print, but some zits were seen on the printed sensor, as seen in Figure 6.16(c). After baking the sensor, it was easily torn apart because of a lack of adhesion between the top and bottom layer, as seen in Figure 6.13(a). Other prints have holes in them, that appeared after the post-processing step, explained in section 4.2.7, which resulted in brittle sensor prints, even when the prints looked normal before baking. This brittle structure can be seen in Figure 6.17. Apart from this, the lack of support for the top layer because of the misprint of dielectric material caused the sensor to be completely broken, as seen in Figure 6.18.

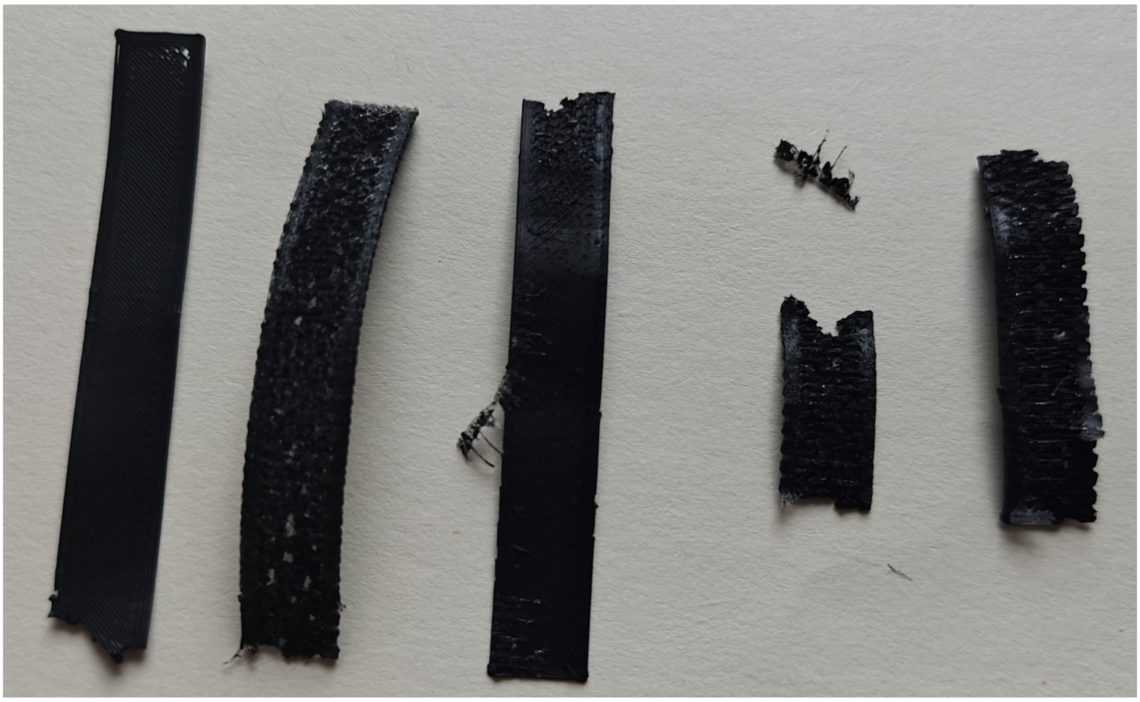

Figure 6.17: Dismantled sensor print with misprinted dielectric.

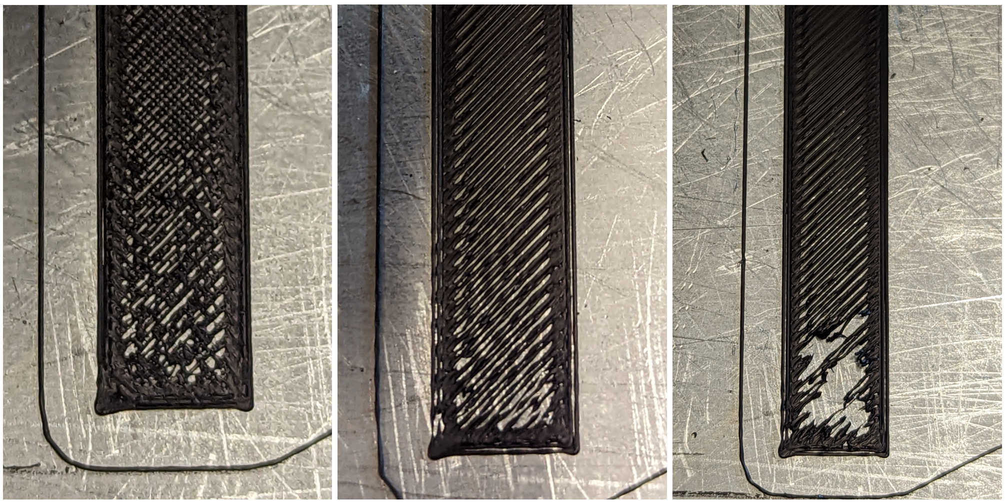

(a) Issues printing the eTPU layer.

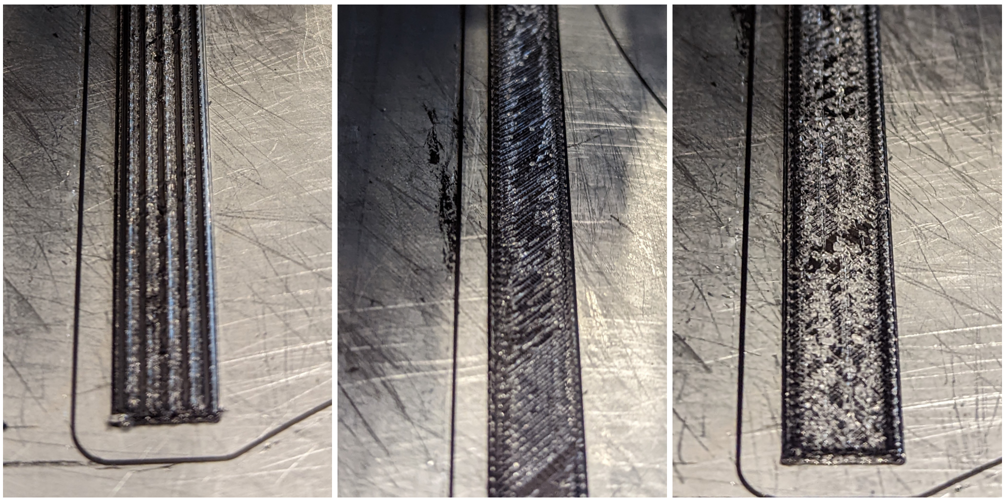

(b) Issues printing the X60 layer.

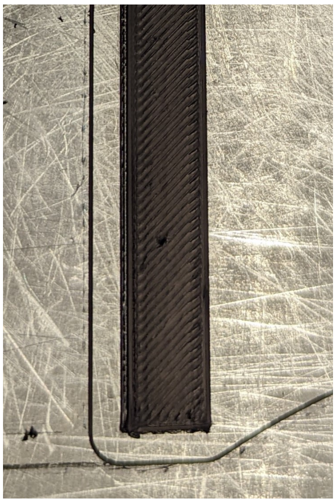

(c) Unsucessfully printed sensor.

Figure 6.18: Different stages of the sensor being printed.

When the infill percentage was less than 100 %, the printer could not understand the outside wall of the sensor, even when it was specified under 'walls' settings in the slicer CURA. As seen in Figure 6.18(a), there were also some calibration issues for the printer. Figure 6.18(b) also shows the printing of X60 in the dielectric layer on failed prints. It is safe to assume that most of the prints exhibited these issues while printing the dielectric layer, which resulted in the zits and holes on the top layer of the sensor prints.

(a) The first layer of print.

(b) Failed top layer of print

Figure 6.19: Some issues related to printing.

A similar effect is seen in Figure 6.19(a), where the eTPU layer in the bottom starts to print perfectly in the edges and continues to print perfectly for some more time, till it starts showing 'under extrusion' behaviour. The same issue was faced while printing the top layer of the sensor, as seen in Figure 6.19(b). After adjusting the print temperature, retraction rate and flow rate for the nozzle respective to eTPU filament in the slicer, as suggested in [114–116], a more continuous print was achieved.

As seen in Figure 6.20, there is poor adhesion between the printed electrode layer of eTPU and the printed dielectric layer of X60. This effect might have added to the issues faced during the printing of the top layer of the sensor, as seen in Figure 6.19(b), apart from the lack of support and under-extrusion.

Many prints were achieved as the printing process was being explored, as seen in Figure 6.21(a). The first successful patches are seen in Figure 6.21(b). The dielectric layer of these patches was also printed successfully, as seen in Figure 6.22. Upon baking them, as explained in section 4.2.7, holes started appearing in the prints, visible in Figure 6.13(d). As seen in Figure 6.23, the dimension of the sensor shrunk by approximately 20 % in its dimension. This effect might

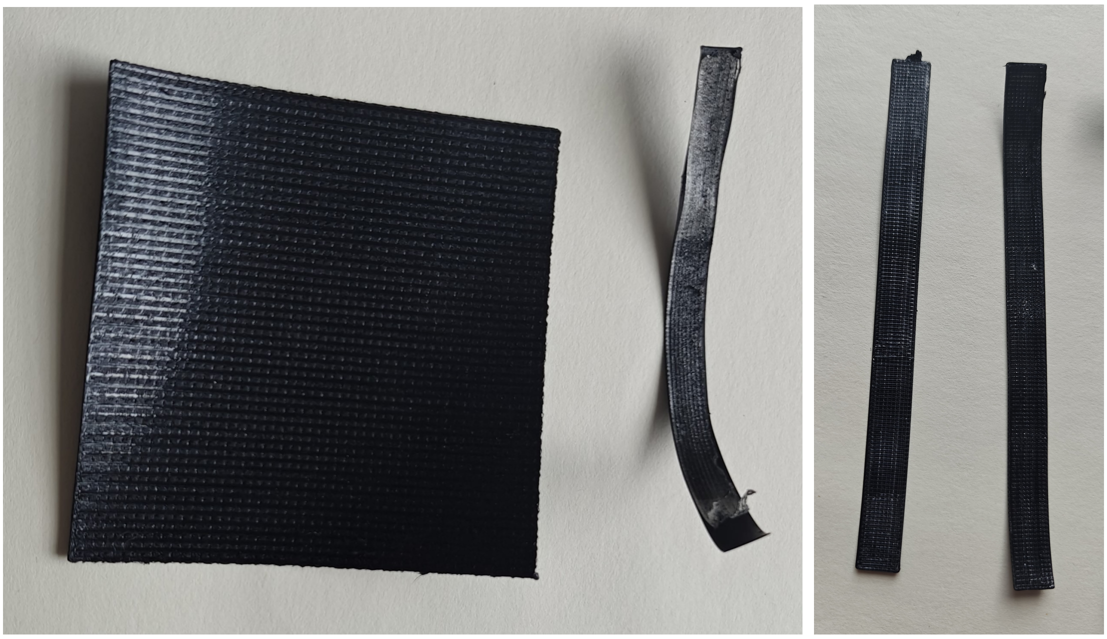

Figure 6.20: Prints without top layer, dielectric layer printed properly.

have caused the internal structure to be inconsistent, causing non-continuous conduction of electricity within the sensor.

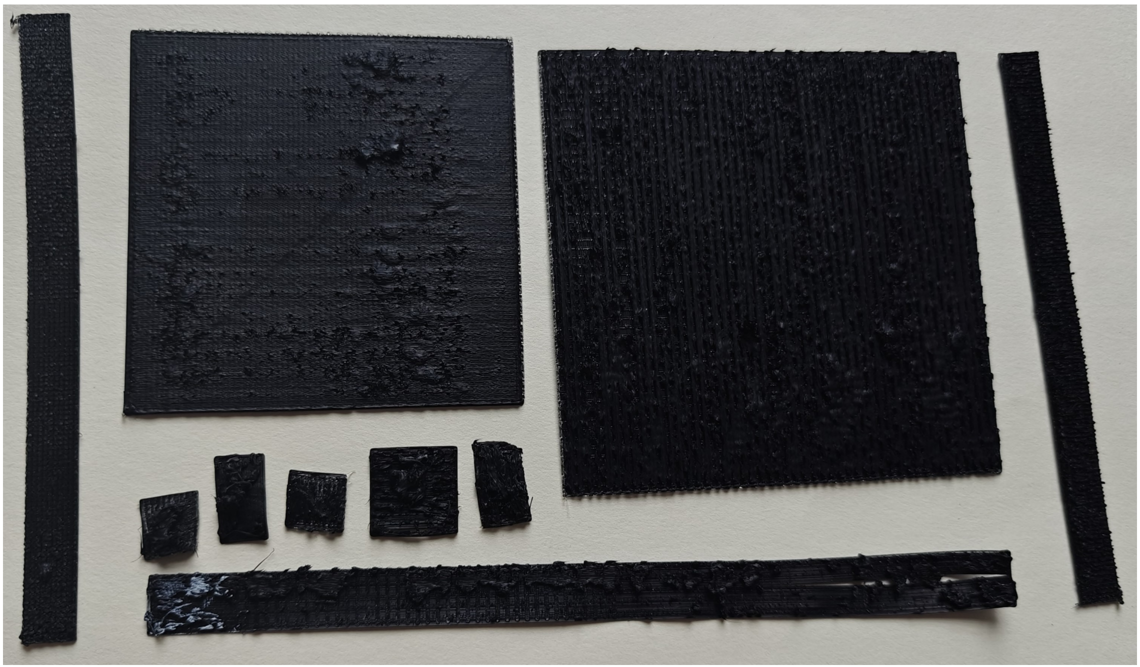

(a) Patches printed with various issues

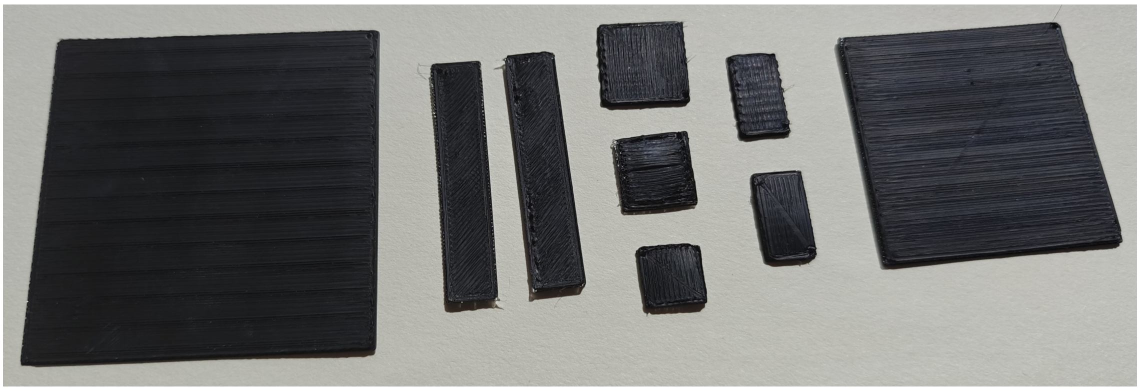

(b) Patches printed successfully

Figure 6.21: Printing of design tested by making different sizes of patches.

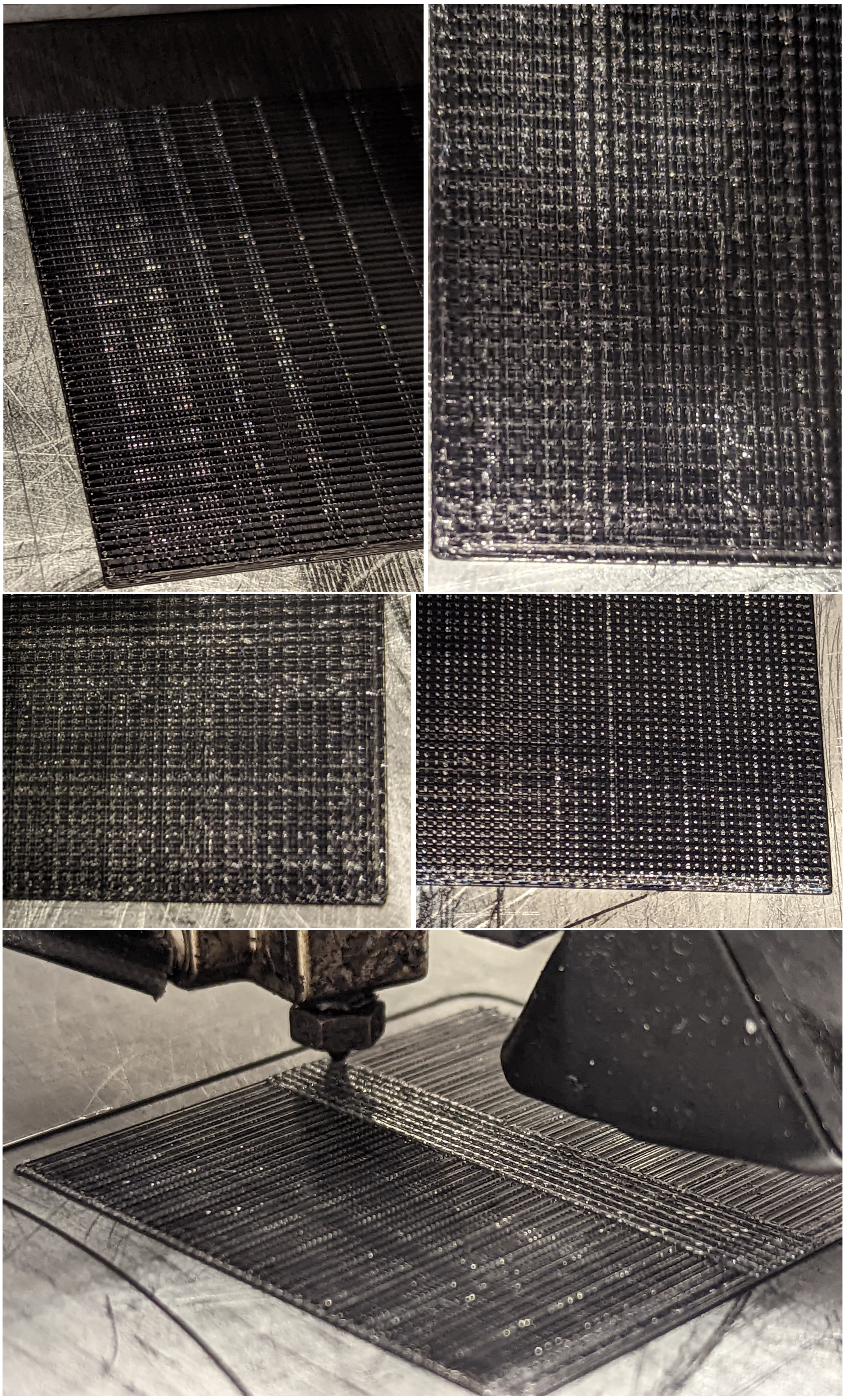

Figure 6.22: Successful printing of dielectric layer artefacts for the sensor.

Figure 6.23: Sensor prints before and after(shrunken) baking.

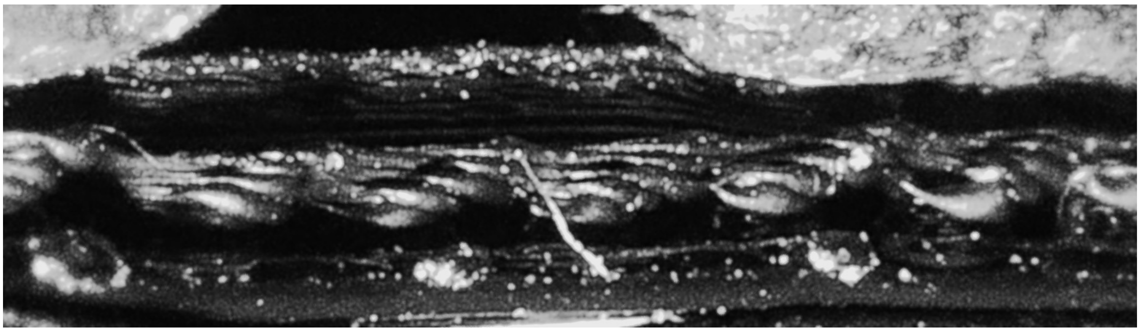

(a) Triangular Design

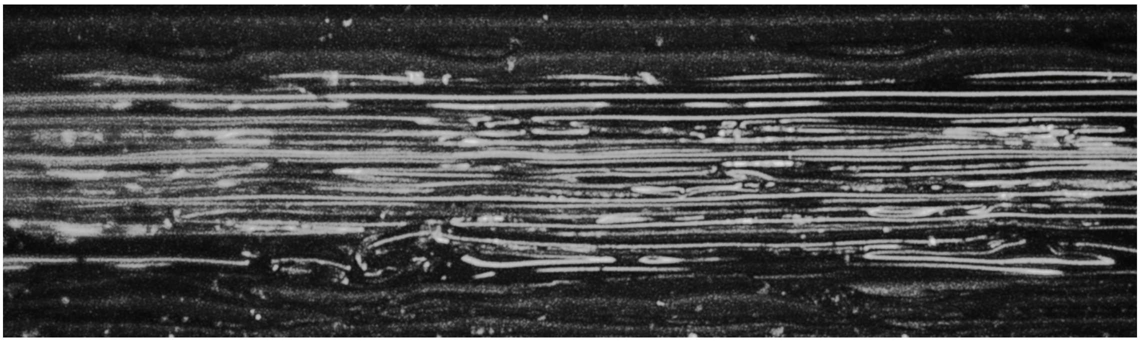

(b) Rectangular Design

Figure 6.24: Printed sensor under the microscope.

6.3 Experimentation Results

As seen in Figure 6.24, the 3DP structure is very different from the model made. This happens because of the line-by-line deposition in the additive manufacturing fabrication. Non-consistent structures are obtained because of the filament deposited in lines on each layer, causing intra-layer voids, explained by Stano et al., shown in Figure 6.25. These voids contribute to a non-homogeneous density in the structure of the sensor. The material's susceptibility is inconsistent because of this, and the polarization varies in all directions, causing irregularities in the impedance measurement. Since the shape of the electrode is not straight and has triangular and rectangular design artefacts, contributing to the cog-like extensions of the electrode, these anisotropic characteristics are amplified, causing scatter in the measurement.

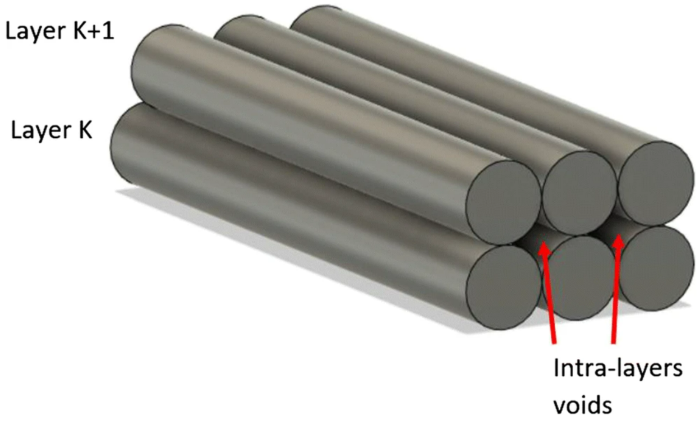

Figure 6.25: Simplification of the welding effect to better understand intra-layer voids. These voids are smaller in reality than this because of the quasi-elliptical shape of the extruded filaments, taken from [117].

Apart from the scatter experienced in the measurement of the signal due to the structural design and fabrication of the sensor, the measurement setup might also have contributed to the signal's noise. The high operational frequencies of the SMAC linear actuator might cause electromagnetic interference in the impedance measurements. The eddy currents induced due to the changing magnetic fields of force application in the device might contribute to this effect. Because this interference was only experienced while the sensor was being triggered with the force application at the position of the trigger, it is difficult to differentiate the sensor measurement from this induced noise.

Additionally, the build plate on FlexenStein3D, as shown in Figure 5.11 is conductive as it is made of metal. When the plate was grounded, a better response was achieved, eliminating signification noise in the measurement, likely because of the connections to the sensor from the power source and the TiePieLCR.

Besides the measurement setup, the noise can also be induced by the piezoresistive effect not accounted for in this project.

A Butterworth filter was designed in MATLAB to filter the data visualised as explained in section 5.3. The real part of the signal is filtered as shown in Figure 6.26(a) and 6.27(a), and the reactance is shown in Figure 6.26(b) and 6.27(b). The Butterworth filter offers a smooth response in the pass band, retaining lower frequencies, and was used as a starting point to remove noise.

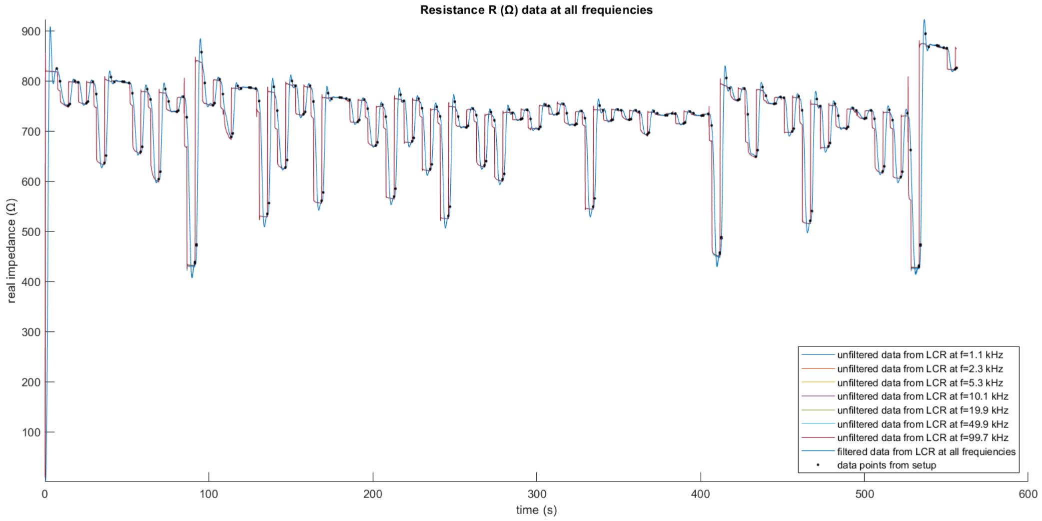

(a) Filtered and unfiltered resistance data for all the frequencies used.

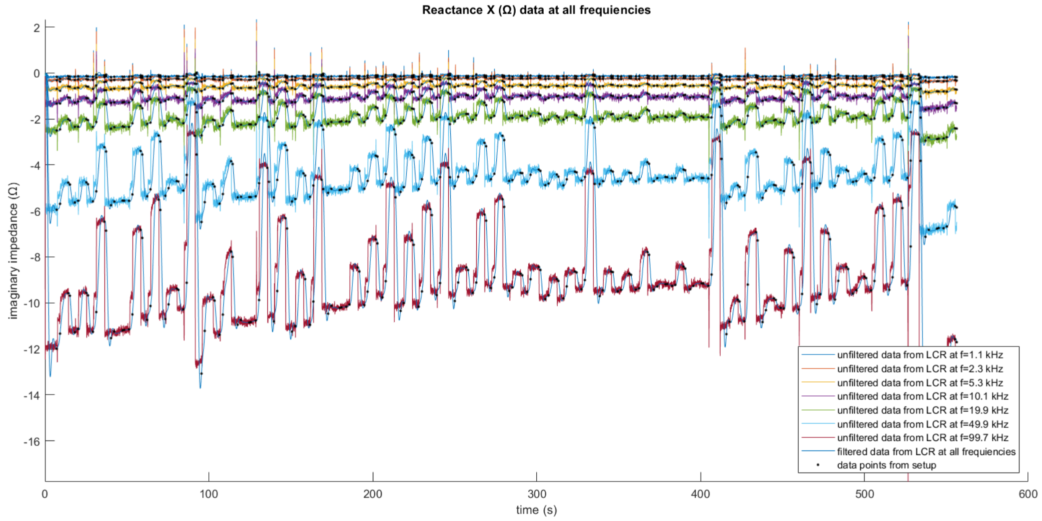

(b) Filtered and unfiltered reactance data for the frequencies used.

Figure 6.26: Filtered and unfiltered impedance data from a set of experiments, data points are denoted by dots in measurement signal, for the frequencies used.

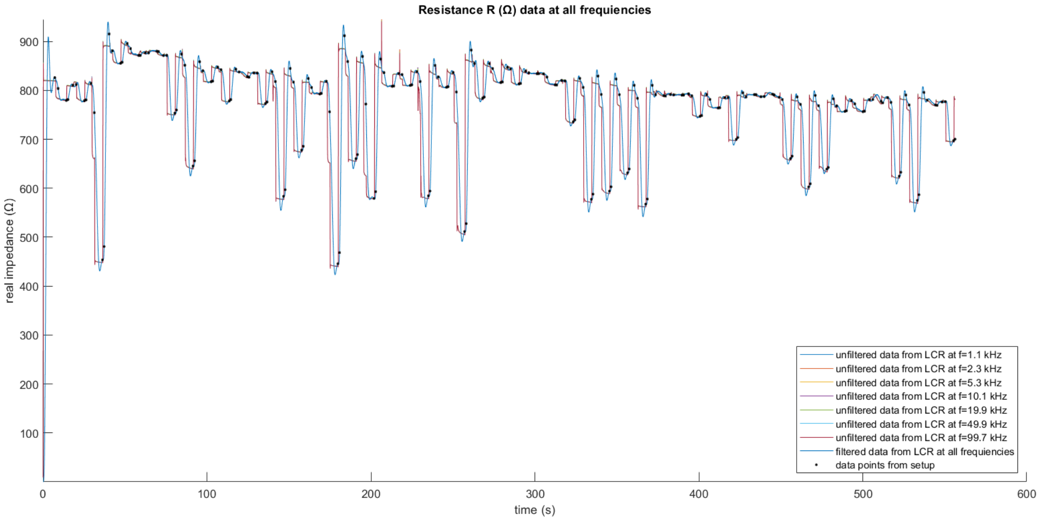

(a) Filtered and unfiltered Resistance data for all the frequencies used.

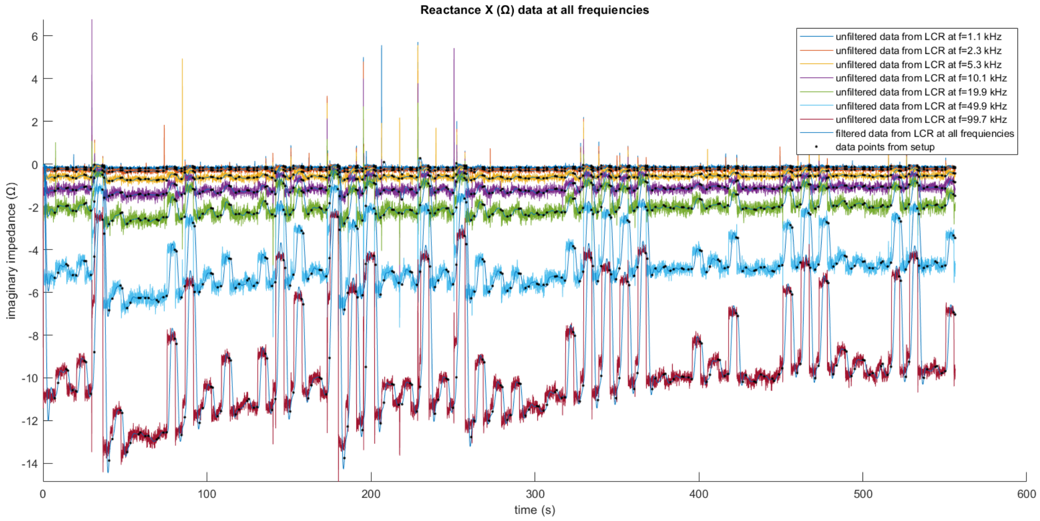

(b) Filtered and unfiltered Reactance data for all the frequencies used.

Figure 6.27: Filtered and unfiltered impedance data from a set of experiments, data points are denoted by dots in measurement signal, for the frequencies used.

Figures 6.28 and 6.29 show a drift in the measurement. In the previous work done in this project, this problem was discussed and a double-layered sensor was concluded to give the best results. In this project, only a single layer of the designs was printed to understand the changes in the drift of the response along with the changes in sensitivity. This new sensor design with increased sensitivity is developed to be used for a 2D sensor mentioned in the next section 7.2.6. Two layers of this design are to be added as mentioned in Figure 7.3. If drift is observed at that stage, the strategy of differential measurement, tested by Patel in previous work [24, 54] can be applied to a double-layered differential sensor can be used instead of a single-layer sensor.

The data points of interest in this project are the change in impedance response between the relaxed sensor: data points are seen as circles in Figure 6.28 and Figure 6.29 and the sensor being probed with force, seen in the figures as dots. The difference of these points of measurement gives the highest change in impedance, as visible in the figures. The drift in measurement can be neglected because of this.

Figure 6.30(a) shows the change in impedance values for a set of experiments done on a sensor with the triangular design, and Figure 6.30(b) shows the response for the same design, but with different sensor print. As it is immediately visible, there is no trend seen in the response. The expected response was close to Figure 6.1. This noisy response might be because of various reasons like the short-circuiting of the electrodes, due to shirking during the post-processing, the misprints in the dielectric layer causing zits and holes on the top layer, or the inconsistencies in the printing of the electrode, as explained in the previous section.

Since the added artefacts in the design result in inconsistency in the polarization and the direction of it, noise can be induced in the structure. As seen in Figure 6.24, the inconsistencies in the structure because of the fabrication process could have introduced anisotropic properties, adding to the noisy measurement.

In contrast to the results from the mathematical model made in MATLAB, seen in Figure 6.1, the experimental results show no difference in the response of the real part-resistance of the impedance response, but the imaginary part-reactance shows a very high dependency on the frequency, seen in Figures 6.31, and 6.32. This is because of the equation 2.24, where the dependence of ω on the capacitive reactance is signified.

Figure 6.33 is the visualization of the difference in the impedance value for all the successful data sets, described in Table D.1, Appendix D. The difference in impedance was relatively higher in some data sets than in others. To compare all the results, the values of difference in the resistance and the reactance values were normalized in the range of 0, to 1,

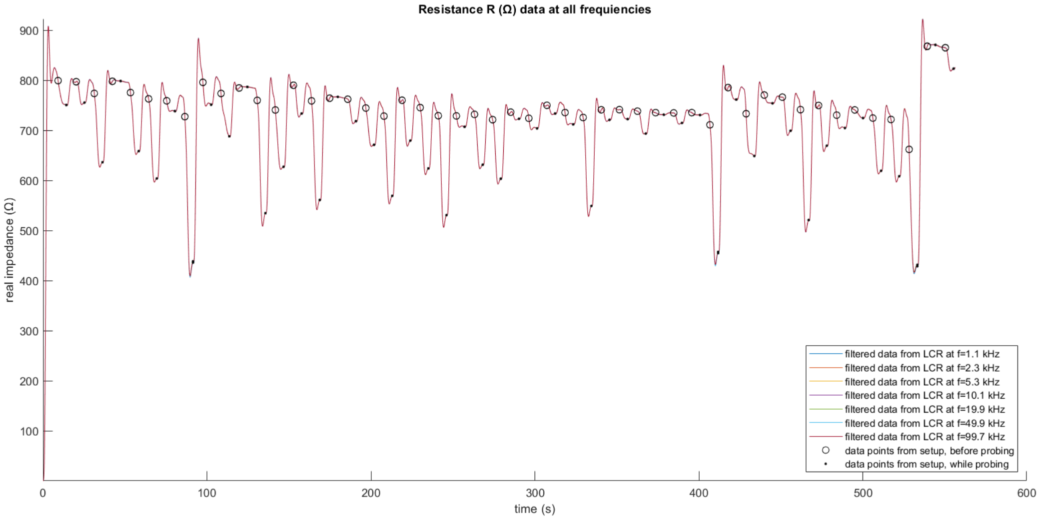

(a) Real part of impedance response from a set of experiments, for all the frequencies used.

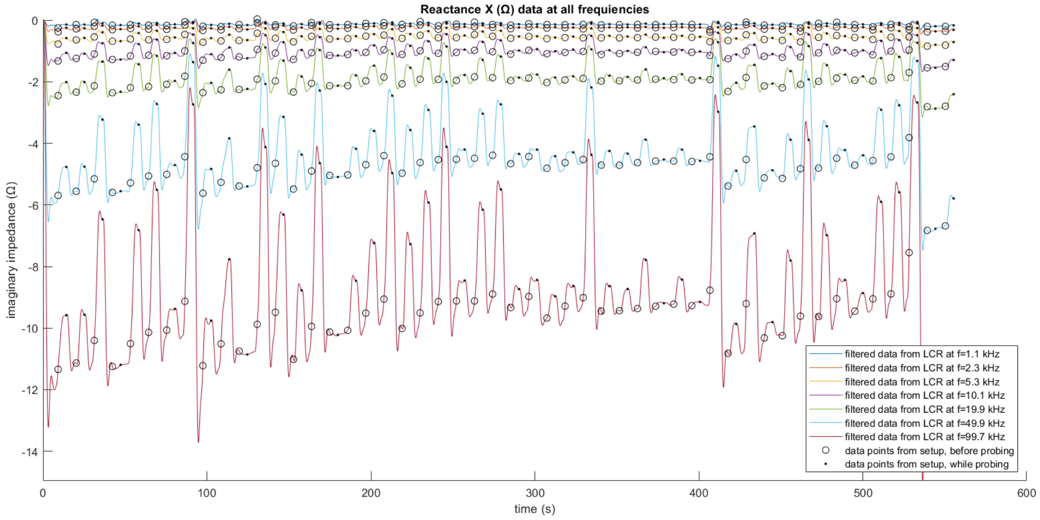

(b) Imaginary part of the impedance response from a set of experiments, for all the frequencies used.

Figure 6.28: Impedance response from a set of experiments, data points taken before the sensor is probed with force are denoted by a circle, while the data points taken while the sensor is probed are denoted by dots in measurement signal, for the frequencies used.

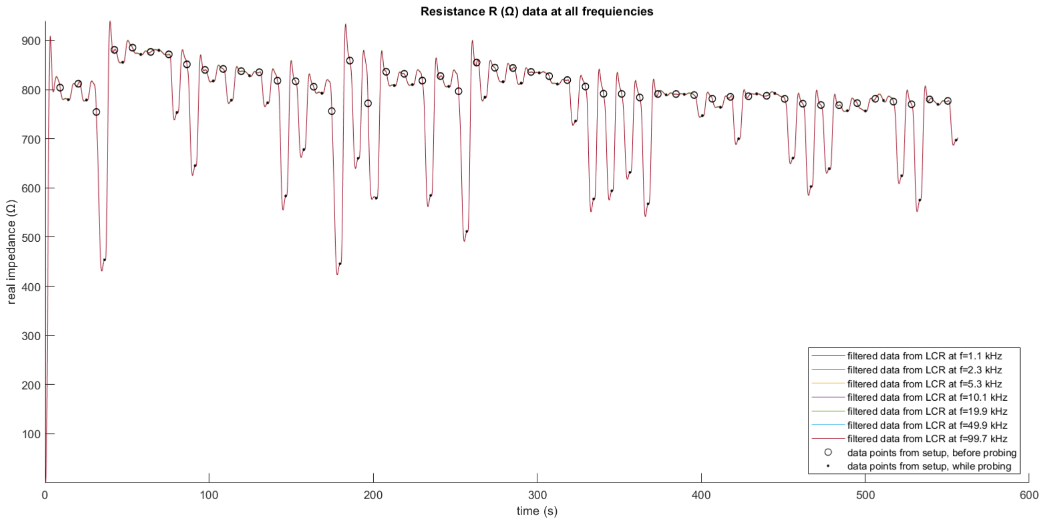

(a) Real part of the impedance response from a set of experiments, for all the frequencies used.

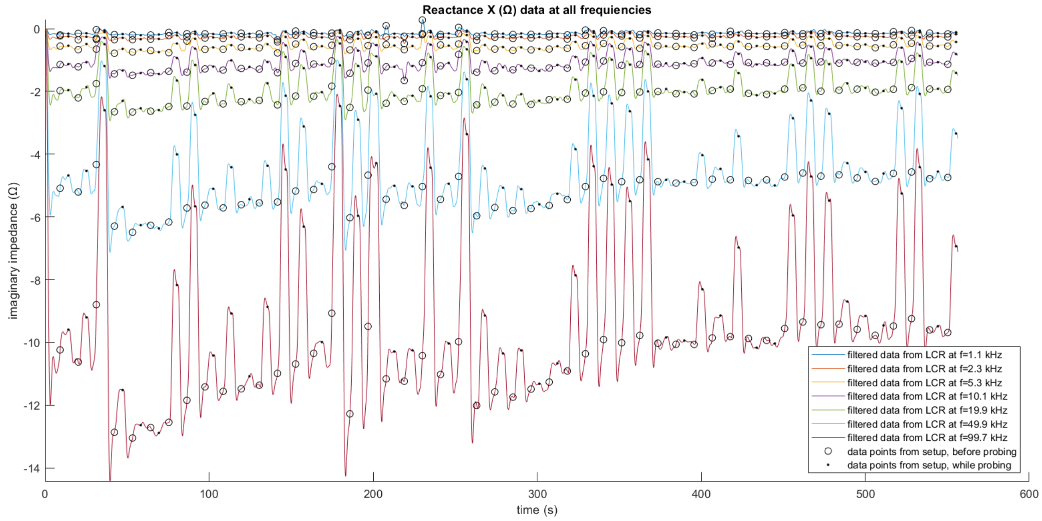

(b) Imaginary part of the impedance response from a set of experiments, for all the frequencies used.

Figure 6.29: Impedance response from a set of experiments, data points taken before the sensor is probed with force are denoted by a circle, while the data points taken while the sensor is probed are denoted by dots in the measurement signal, for the frequencies used.

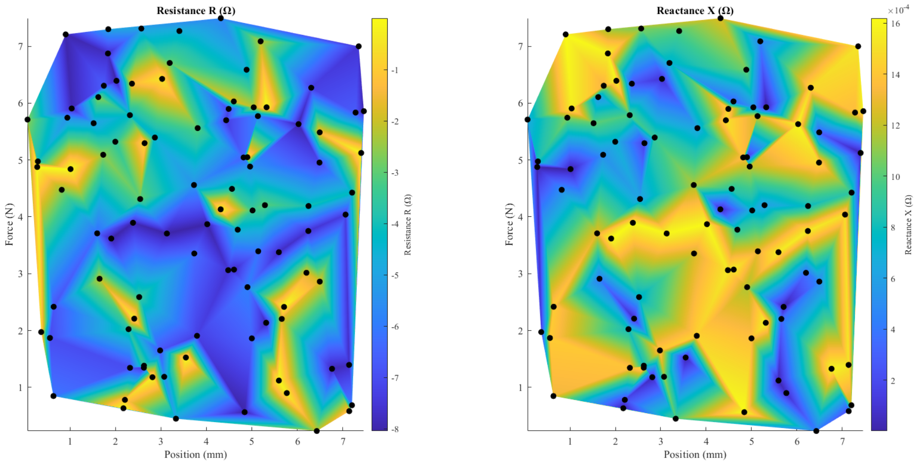

(a) Impedance response from a set of experiments with the triangular design, for 1.1 kHz frequency.

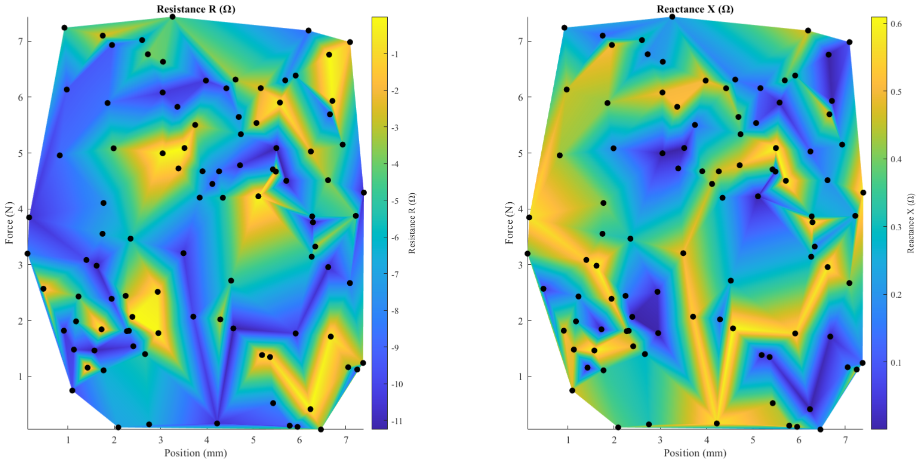

(b) Impedance response from a different set of experiments on a different printed sensor, with the triangular design, for 99.7 kHz frequency.

Figure 6.30: 3D interpolated surface of change in impedance data from a set of experiments. The change is measured between data points taken before the sensor is probed with force, denoted by a circle, and data points taken while the sensor is probed, denoted by dots in the measurement signal, similar to the one shown in Figure 6.28.

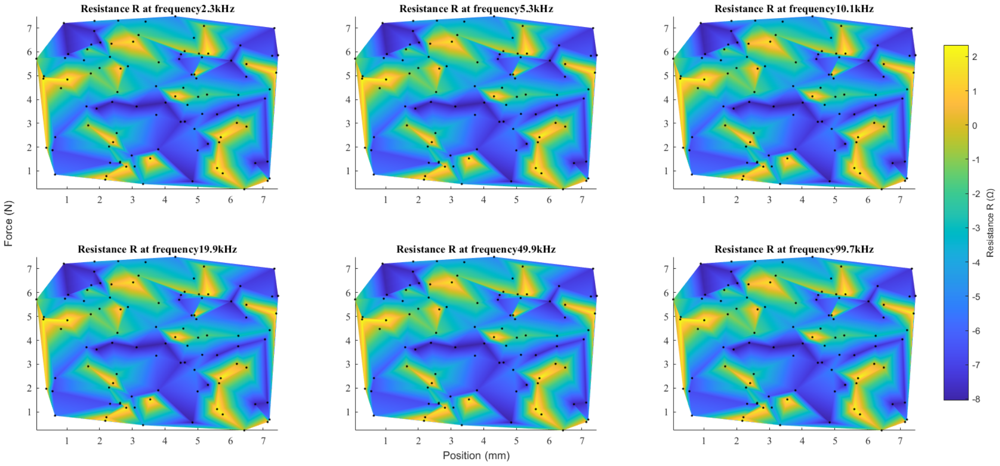

(a) Real impedance (resistance R) response from a set of experiments, for the frequencies used.

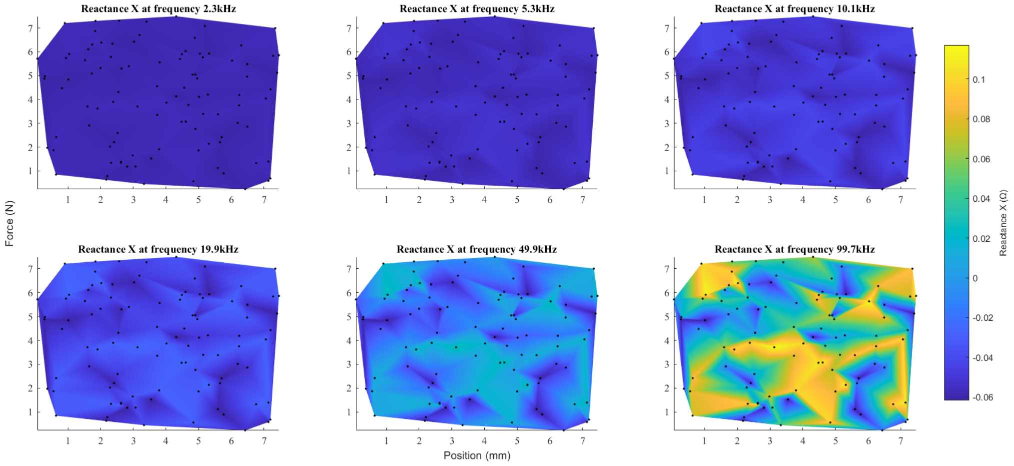

(b) Imaginary impedance (reactance X) response from a set of experiments, for the frequencies used.

Figure 6.31: 3D interpolated surface of change in impedance data from a set of experiments. The change is measured between data points taken before the sensor is probed with force, denoted by a circle, and data points taken while the sensor is probed, denoted by dots in the measurement signal shown in Figure 6.28, for the frequencies used.

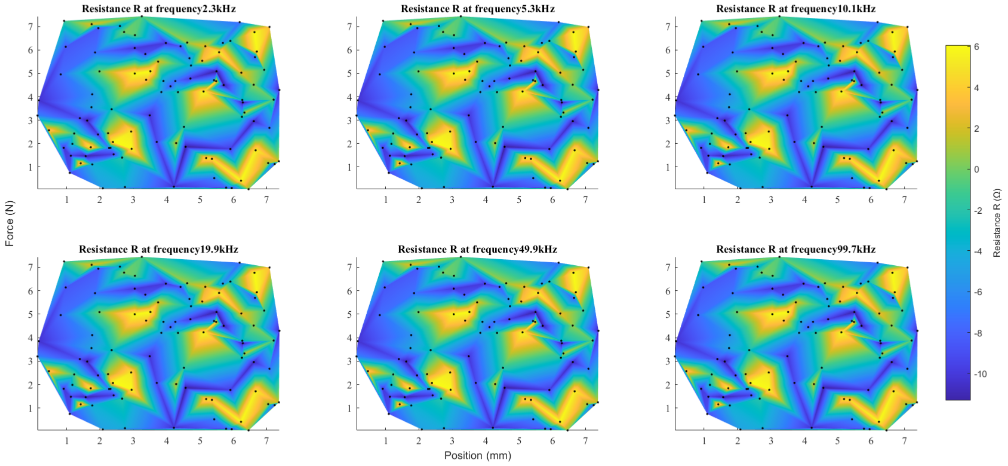

(a) Real impedance (resistance R) response from a set of experiments, for the frequencies used.

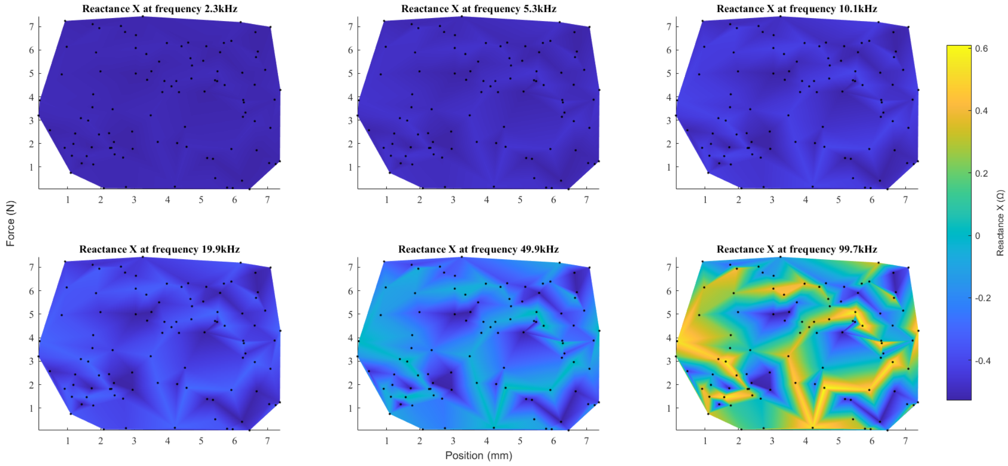

(b) Imaginary impedance (reactance X) response from a set of experiments, for the frequencies used.

Figure 6.32: 3D interpolated surface of change in impedance data from a set of experiments. The change is measured between data points taken before the sensor is probed with force, denoted by a circle, and data points taken while the sensor is probed, denoted by dots in the measurement signal shown in Figure 6.29, for the frequencies used.

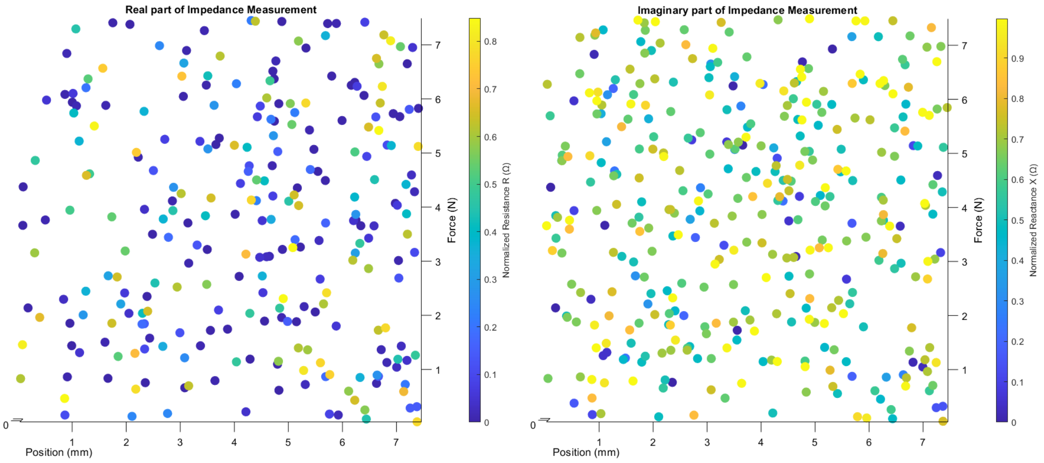

Figure 6.33: Measured difference between impedance before pressing and impedance while pressing the sensor. The values are normalised and the successful sensor prints are included.

6.4 Conclusions

In this chapter, the results were introduced and discussed. Initially, the simulation results were explained and divided into results from the mathematical models and the FEA simulations. The results from the mathematical models using MATLAB showed clear differences at various ranges of frequencies, although the range of sensing decreased as higher frequencies were introduced. The need to use a multi-frequency approach was favoured based on these results. The FEA results revealed a relatively small change in the dimensions of the structure, as well as a smaller change in capacitance response. Subsequently, the FEA simulation results were compared to the results of the analytical model. However, it is safer to assume that the analytical response and the response of FEA model made by manually changing the size of the air gap only shows the contribution of the added air gap artefact in the design and the slope of the FEA simulation that did not reach the desired results is a more accurate representation of how the structure should work. The next section discussed the issues faced during the fabrication process and the steps taken to minimize them. This was followed by the introduction of the response of the printed sensor, tested on the experimental setup. Many insights were presented about the lack of desired trends observed in the experiment results. The results outlined here successfully address the key research questions in this project.

7 Conclusions And Future Considerations

This chapter attempts to conclude the developments in this project by answering the research questions, introduced in chapter 1. Recommendations based on lessons learned throughout this project are included in the final section of the report.

7.1 Conclusion

The project reported in this document aims to investigate the effects of adding microstructure on the sensitivity of the elastomeric sensor and of adding multiple frequencies to the readout technique. As previously mentioned, the overall goal of this project is to create an in-shoe force and position sensor for applications such as gait analysis. For that, the primary objective is to add a dimension for detecting the measurement of the force and location of the sensor.

7.1.1 Effect of Addition of Microstructures on Sensitivity

- Two different microstructures are explored in this project:

  cog-like structures that were added to the electrode, and

  air gap added to the dielectric layer.

- Two different sensor designs were created:

  Triangular Design, with triangular cogs in the top layer of dielectric and polygonal air gaps between the dielectric and the extension of the electrode layer, and

  Rectangular Design, with two layers of rectangular artefacts, laid transverse to each other, both layers containing dielectric materials, air, and electrode material.

- From the past work of Patel [24], the SX60 sensor design was used as a base design for design exploration in this project. FEA models were created in COMSOL Multiphysics to understand the change in the geometry and the electric potential distribution at the time of probing of stress.

  The first model used Solid Mechanics and Electrostatics physics simultaneously, applying $1 \times 10^5\,\mathrm{N\,m^{-2}}$ stress on the top electrode, with 1 V potential at the terminal, and grounding the bottom terminal, with constrained movement.

  The highest deformation output of approximately 3.5×10^{-3} mm on the Triangular design; and of approximately 7.5×10^{-3} mm was seen on the Rectangular design.

  The change in capacitance output of approximately 10 pF can be projected from the slope of output from the change in dielectric layer height, which was less than 0.05 mm for the Triangular design; and of approximately 1 pF can be projected from the slope of output from the change in dielectric layer height, which was less than 0.005 mm on the Rectangular design.

  The second model manually swept the dimension of the air gap within the structure of the sensor and applied Electrostatics physics with 1 V potential at the terminal, and grounding the bottom terminal, with constrained movement.

  The change in capacitance output of approximately 1 pF for the change in dielectric layer height, which was than 0.45 mm for the Triangular design; and of approximately 0.01 pF can be projected from the slope of output from the change in dielectric layer height, which was less than 0.005 mm on the Rectangular design.

  The last models used Solid Mechanics and Electrostatics physics simultaneously on a 2D and a 3D sensor model, of a simple capacitor, without any artefacts of cogs and air gaps. This was made to serve as a reference design, to understand the change in sensitivity.

The highest deformation output of approximately 17×10^{-6} mm on the 2D model; and of approximately10×10^{-6} mm was seen on the 3D model.

The change in capacitance output of approximately 10 pF for the 2D design; and of approximately 10.001 pF on the 3D model.

This gives around 10 % increase in the sensitivity of the capacitive measurement in the Triangular design when compared to the 2D model, and gives around 10 % increase in the sensitivity of the capacitive measurement, proving that the sensitivity is positively affected by the artefacts explored in the project.

- Both the sensor designs were fabricated using 3D Printing (3DP) with Fused Deposition Modeling (FDM) / Fused Filament Fabrication (FFF). However, many difficulties were faced during this process, considering the nature and dimensions of the interlayer artefacts designed.
- Inconsistencies in the prints of the dielectric layer of the sensor resulted in short circuits and a non-homogeneous structure of the sensor, contributing to the ambiguity of the experimental response. It caused the response of the sensor to lack a trend in the force and position measurements.

7.1.2 Multi-Frequency Approach

- From the past work of Patel [24], the SX60 sensor design was used as a base design for design exploration in this project. The mathematical model of this sensor was modified to add a multiple frequency response, using 7 different frequencies simultaneously to measure the change in impedance values at the time of the application of force, at various positions.
- From the results of this project, it is possible to determine the multiple frequency readout approach to increase the sensitivity of the sensor and expand the size of the sensor from 1D to 2D.
- The response of the real part of the impedance-resistance varies negligibly, showing minimal dependence on the frequency; while the response of the imaginary part of the impedance-reactance varies substantially, showing significant dependence on the frequency.
- A single frequency can be used to measure force at various positions, while multiple frequencies can be used to precisely determine which force is applied at a particular position.

7.2 Future Considerations

During this project, many insights were gained about the 3D printing process as well as the sensor design. The following considerations are recommended:

7.2.1 Filament Pre-Drying and Storage

As explained in section 3.3, it is important to pre-process eTPU and X60 filaments to get a smooth print. To avoid this, storing the filament away from moisture is very important [118].

TPU exhibits hygroscopic properties, which are unlike most other commonly used filaments. Apart from that, eTPU is sensitive to temperature, moisture and age, as explained in section 6.2. Therefore, it is advisable to dry TPU after each print. The drying process can be carried out using an oven set at a temperature of 65 °C for approximately 4 h to 5 h, as recommended by [119].

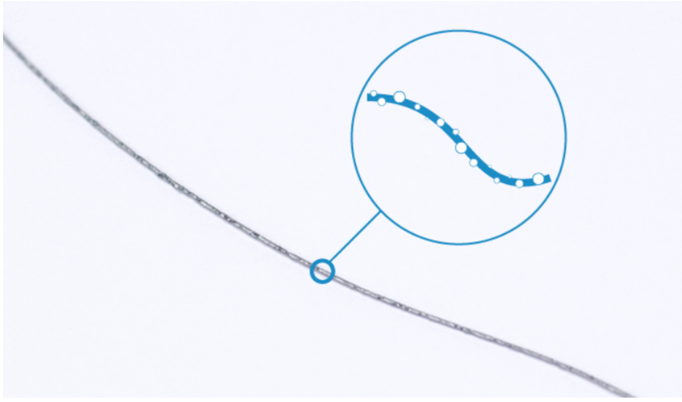

Figure 7.1: Air bubbles found in filament of BVOH [97].

Alternatively, the manufacturers of [120] suggest a temperature of 90 °C for 1 h. Many recommendations suggest adding a significant amount of silica gel beads from desiccant packets to an airtight storage box. A food dehydrator can also be used for this purpose. It is worth noting that both eTPU and X60 can benefit from being stored in a closed dry box containing a 60 W utility lamp overnight.

For better printing of eTPU with the intricate design artefacts introduced in this project, similar to cogs and air gaps, it would be easier to use support material, as explored in this project, described in section 4.2.4. Because these materials are water-soluble, it is important to pre-dry and store the filaments properly.

7.2.2 Infill Percentage

Considering the positive conclusions drawn by Patel in [24], it was obvious that decreasing the percentage of dielectric infill further increases the sensitivity of the sensor. Since we have the dielectric height less than 1 mm and with a lot of microstructures, the change in the percentage of infill was seen to make no difference to the design. It is expected to have greater effects if the slicing profile is defined as fine, with the layer height of 0.1 mm, change the walls, by making the wall thickness 0.8 mm, printing thin walls. The top/bottom thickness in the corresponding tab should be set for 0.3 mm for a 1.2 mm dielectric layer. The skin layer on the upper surface can be set between layers 0 , to 3 , depending on how well eTPU adheres to X60. It should all be using lines for simplicity. Now, the infill percentage can make sense. Before that is changed, it is good to ensure that the infill line distance is less than or equal to 0.3 mm and the infill pattern is set to be a grid, to ensure a homogeneous output. Infill percentage can safely range from 20 % to 100 %, but it is easier to control the wall thickness and let the infill density be defined automatically unless the amount of dielectric used is to be controlled.

Stano et al. conducted a study on a 3D-printed capacitive force sensor with various infill patterns, including Cross3D, Gyroid, and Zig-zag. They tested prototypes and analysed the change in capacitance. The results indicated that the Cross3D infill structure demonstrated the highest increase in sensitivity [70].

7.2.3 Influence of Slicing

The proposed method was not evaluated due to the inability to successfully print a simpler design with 100 per cent infill density, which was previously described in section 6. It resulted in inadequate printing of the dielectric layer between the electrodes and caused the sensor to behave as a short circuit upon application of force to this component.

Investigating the influence of slicing, specifically the direction of the line, on sensor performance is a potentially valuable avenue for further research. Vu et al. evaluated the impact

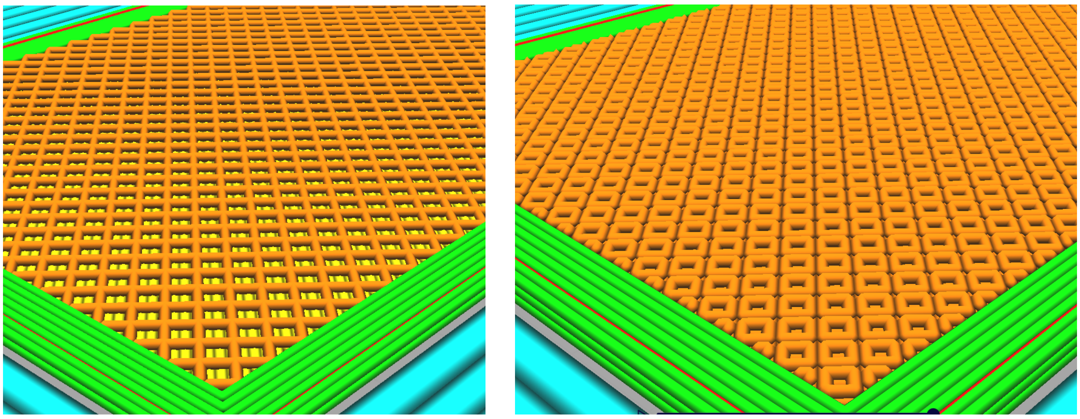

(a) Sliced preview of the dielectric layer with a lower infill percentage and thin walls.

(b) Sliced preview of the dielectric layer with a higher infill percentage at the same distancing, with double walls.

Figure 7.2: Proposed technique for infill percentage demonstrated.

of three different 3D printing line directions (45°, 90°, 180°) on resistive sensor stability and reliability [101].

7.2.4 Adding Isolation Layer

A passive isolation layer can be added on top of the electrode of the sensor to eliminate any cross-electrostatic coupling arising from the interaction between the sensor and the human body. This is an important addition as the sensor is designed to work accurately only if the human body is directly on top of the flat surface of the sensor, without any shoes on. One way to use it is also to add it inside a shoe as a shoe sole.

7.2.5 Other Additive Manufacturing Methods

Alternatively, several advanced additive manufacturing technologies can be explored, apart from Fused Deposition Modeling (FDM)/Fused Filament Fabrication (FFF). More recent technologies allow microscale precision, with some even capable of reaching nanometre resolutions, thereby making them suitable for intricate designs. Recent developments in Stereolithography (SLA) can be used to mitigate the anisotropic properties experienced in sensors fabricated using FFF. Multiple materials can be used simultaneously on a single print, as required in this sensor design, as it is possible to use multiple materials consequently for it [121–123]. Microstereolithography (μSLA) and Projection Microstereolithography (PμSL) are also increasingly being researched on, although expensive at this phase. μSLA utilizes an ultraviolet laser to cure photosensitive resins, creating highly detailed parts with fine features. PμSL, employs ultraviolet light from a projector, allowing for the rapid photopolymerisation of entire layers [124]. Furthermore, another precise technology is Two-Photon Polymerization (2PP), which uses a pulsed femtosecond laser to achieve sub-micron resolutions, positioning it within nanofabrication. Because the methods most frequently used for micro additive manufacturing technology use VAT polymerization like these, it might also be possible to make better designs that focus on application parameters and not on fabrication. Although it is not possible to mass manufacture with these technologies, they are increasingly being accepted as fabrication techniques [125].

7.2.6 Adding Dimension

Many strategies can be applied to add sensing across another dimension for this now-sensitive sensor design. Patel, in his report, suggested implementing a similar approach as Xu et al. [72, 78]. Two dielectric sheets were stalked perpendicular to each other. It was found that high-frequency signals get attenuated into the electrode as its length increases, while low-frequency signals are retained throughout the length. They used two different capacitance sensing circuits to probe the keyboard with sensing frequencies of 1 kHz to 60 kHz frequency sweep. After dividing the sensor into four virtual quadrants, the capacitance change was measured for both frequencies. Higher frequency response in both x and y directions was used to determine the quadrant being probed. They found that the capacitance change was relatively larger near the origin. Lower frequency capacitance change was used to determine the amount of pressure applied by the probe. This multi-frequency approach was used to scale the sensor from a 2x2 array to a 3x3 array. The sensor can be subdivided to increase the resolution; however, there is a limit as each additional section reduces the area of the section, which reduces the difference in capacitance between two adjacent frequencies. All the frequencies used to analyse the sensor behaviour should be below the cut-off frequency.

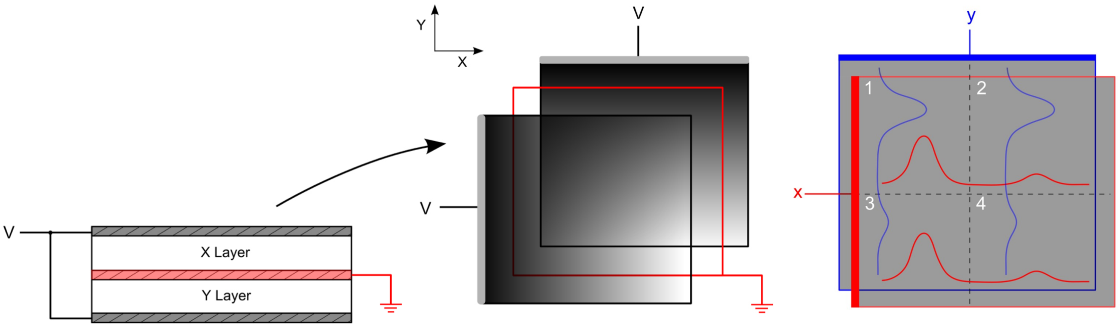

(a) Input-output connections on the sensor for current and voltage readout.

(b) Dividing the sensor using the multi-frequency approach explored in this project.

Figure 7.3: Concept for adding dimension in the future for the explored sensitive sensor, courtesy [78].

Apart from this, electric connections are also possible to be made in smaller segments, as shown in [126]. Grids can be made of smaller sections of the unidirectional sensor, and each wire can be connected to a single element of the grid.

Contrary to the complexities because of that, the multi-frequency approach used in this project can be implemented by connecting sensors on the edge, as shown in Figure 7.3. Apart from this, other strategies can be explored, such as the segmentation of the sensor suggested by Zhu et al. [127] or making a grid like in a keyboard with conductive and non-conductive materials, as suggested by Yao et al. [128]. It is also nice to avoid multiple wires connected to the sensor, which would be required if the common approach is taken, suggested by Lou et al. [129]. To avoid multiple wires, it could be possible to use a multiplexer in the shoe and use some remote communication module to process probing position and force information and avoid connecting more than 5 wires to the shoe, but more sophisticated approaches exist and this should be used as the last resort.

7.2.7 Adding Passive Layer for Insulation

To avoid the noise in capacitance due to contact of the body with the top layer of the sensor, a simple solution is to add a layer of 0.1 mm of a non-conductive material, like elastic TPU or X60 on top of the sensor. This was not tested because of the time restriction, and the problem of cross-conduction was solved by adding a tip to the SMAC instead, as explained in figure 5.5. But for testing the sensor, it would need to be as a mat or as a shoe sole, and the addition of such an insulating layer would be beneficial* [130].

A Tools and software used during this assignment

During the preparation of this work, the author used ChatGTP, Google Scholar and GITHUB, among other tools to find relevant information about the material properties, the 3D Printing (3DP) processes as well as some coding-related information. LanguageTool, Grammarly, and QuillBot were used to help with the writing process. The author also used MATLAB, COMSOL, LaTeX and other in-house built Graphical User Interface (GUI) and codes described in the report. The operation of simulations and experiments were carried out using the code made by Schouten and Patel, as expressed in relative parts of the report. After using this tool/service, the author reviewed and edited the content as needed, and takes full responsibility for the content of the work.

B Mathematical Model of Previous Work

Patel [24] made a parallel plate capacitor that was fabricated using 3D Printing (3DP). The sensor was formed by a layer of dielectric of thickness d printed using X60, sandwiched between two conductive layers of elastomeric thermoplastic polyurethane (Expanded Thermoplastic Polyurethane (eTPU)) acting as electrodes for of the capacitor. This sensor has connections on one of the edges of the sensor, as shown in Figure B.1. It gives information about the magnitude of force applied as well as the position at which the force is applied.

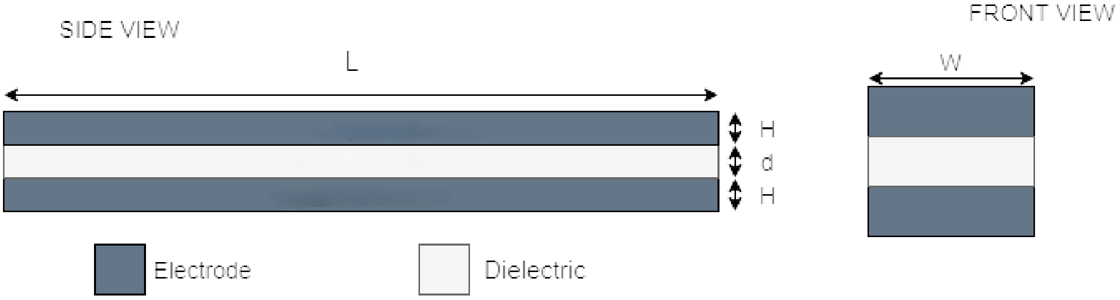

Figure B.1: Schematic diagram of the sensor designed by Patel, reused from [24].

Xu et al. [78] developed a stretchable programmable rubber keyboard that uses dielectric elastomer sheets made from a curing PDMS dielectric sandwiched between two conductive electrodes doped with carbon black particles. Resistance distributed between electrodes is lossy, creating a gradient across the electrodes for different voltages. A low-pass filter characterizes each infinitely small segment of this highly resistive dielectric and acts as a transmission line of resistors and capacitors. Patel used this model to localize applied force in his sensor design.

Because of FDM 3DP, structures show anisotropic electrical properties. To characterize such properties of conductive surfaces, the model discussed by Dijkshoorn et al. is used [131]. The cross-section of the sensor designed by Patel can be visualized as Figure B.1. The sensor has a dielectric of thickness d 3DP using Thermoplastic Polyurethane (TPU) sandwiched between two conductive layers that are 3DP using conductive thermoplastic polyurethane acting as electrodes of the capacitor. It has length L in x-direction, width W in y-direction and height H in z-direction. Patel describes the flow of current due to changing potential across each electrode. The voltage across the electrodes and the current can be characterized using a set of differential equations. To solve these equations, we need to first determine the boundary conditions of our sensor.

Boundary Conditions

To solve for the coefficients of our eigenvectors and eigenvalues, the following four boundary conditions for voltage and current at $x = 0$ and $x = L$ are possible.

1. Fixed voltage: top electrode connected to fixed voltage supply U_{in}, bottom electrode connected to the ground

$$\begin{aligned} U_1(0) &= U_{\text{in}} \\ U_2(0) &= 0 \end{aligned} \tag{B.1}$$

2. Fixed current: sensor input

$$I_1(0) = I_{\text{in}} \tag{B.2}$$

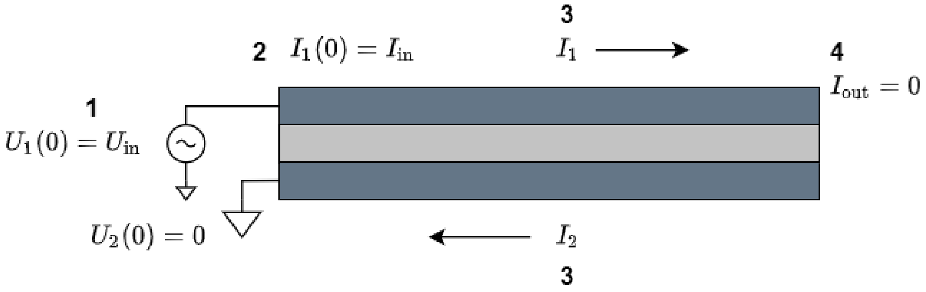

Figure B.2: Illustration of the used boundary conditions.

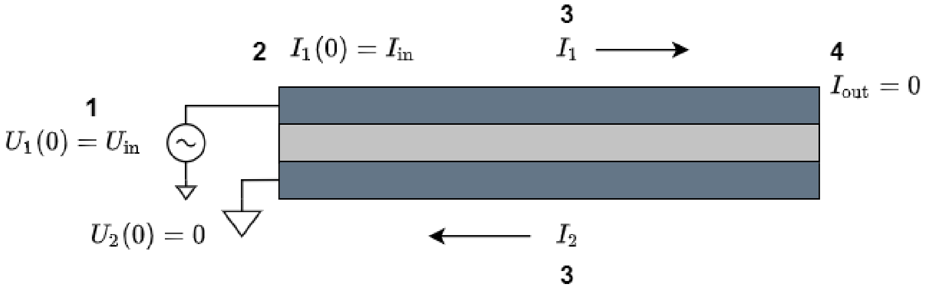

Figure B.3: Illustration of the used boundary conditions.

3. Open connections: sensor not connected on any other side

$$I_{out}(L) = 0 \tag{B.3}$$

4. The current going through the circuit will return to the source.

$$I_1(L) = -I_2(L) \tag{B.4}$$

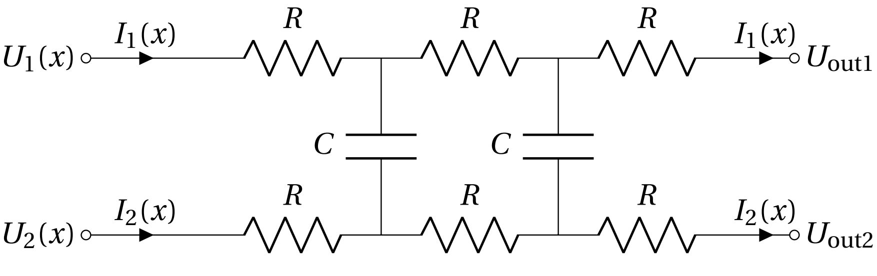

Figure B.4: Circuit diagram of the transmission line model by Patel [24].

The parallel plate capacitive sensor is represented by its equivalent circuit diagram of a lossy transmission line (Figure B.4) [78]. For simplicity, we assume that the electrode is purely resistive. The resistance of the sensor of Δx width can be defined as $R = \frac{\rho \Delta x}{HW}$ with ρ as the volume resistivity of the electrode in $\Omega\,$m. For an infinitely small part of the sensor, the potential difference in track U_1 causes the current to flow from left to right:

$$I_1(x,t) = \frac{\Delta U_1(x,t)}{R_n} = \frac{-HW}{\rho} \frac{\Delta U_1(x,t)}{\Delta x} \tag{B.5}$$

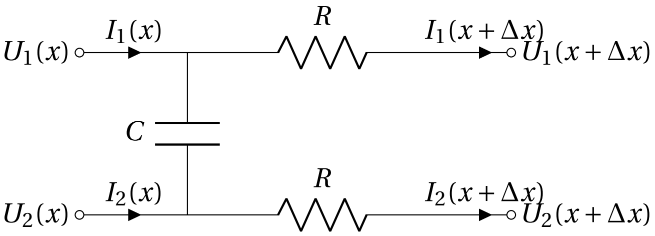

Figure B.5: Electrical diagram for the infinitesimal part of the sensor.

Limit on $\Delta x \rightarrow 0$:

$$I_1(x,t) = \frac{-HW}{\rho}\frac{\partial U_1(x,t)}{\partial x} \tag{B.6}$$

We get this equation in the time domain. Since we want impedance in the frequency domain, the Fourier transform gives us:

$$\hat{I}_1(x,\omega) = \frac{-HW}{\rho}\frac{\partial \hat{U}_1(x,\omega)}{\partial x} \tag{B.7}$$

We differentiate the equation with x to get a second-order term of voltage.

$$\frac{\partial \hat{I}_1(x,\omega)}{\partial x} = \frac{-HW}{\rho}\frac{\partial^2 \hat{U}_1(x,\omega)}{\partial x^2} \tag{B.8}$$

Parallel plate approximation used to get capacitance:

$$C = \frac{\varepsilon_0 \varepsilon_\mathrm{r} A}{d} \tag{B.9}$$

with area A of the plates, distance between the plates d, permittivity of vacuum ε_0 in $\mathrm{F\,m^{-1}}$, and relative permittivity and ε_r.

$$C = \frac{\varepsilon_0 \varepsilon_\mathrm{r} W \Delta x}{d} \tag{B.10}$$

The potential difference of U_2 and U_1 causes the current to pass through the capacitor C. This current I_c is expressed in Fourier transform while assuming harmonic functions as:

$$\hat{I}_1(x+\Delta x,\omega) - \hat{I}_1(x,\omega) = -\hat{I}_c(\omega) \tag{B.11}$$

$$\hat{I}_1(x+\Delta x,\omega) - \hat{I}_1(x,\omega) = \frac{-\left(\hat{U}_2(x,\omega) - \hat{U}_1(x,\omega)\right)}{\hat{Z}_\mathrm{eq}(\omega)} \tag{B.12}$$

The impedance between the capacitive plates is given by:

$$\hat{Z}_\mathrm{eq}(\omega) = \frac{1}{j\omega C} = \frac{d}{j\omega\varepsilon_0\varepsilon_\mathrm{r} W \Delta x} \tag{B.13}$$

Combining equation B.12 and B.13,

$$\hat{I}_1(x+\Delta x,\omega) - \hat{I}_1(x,\omega) = \frac{j\omega\varepsilon_0\varepsilon_\mathrm{r} W \Delta x\left(\hat{U}_1(x,\omega) - \hat{U}_2(x,\omega)\right)}{d} \tag{B.14}$$

Considering an infinitely small slice of the sensor, the above equation can be written as a partial derivative:

$$\frac{\partial \hat{I}_1(x,\omega)}{\partial x} \rightarrow \frac{-HW}{\rho}\frac{\partial^2 \hat{U}_1(x,\omega)}{\partial x^2} = \frac{j\omega\varepsilon_0\varepsilon_\mathrm{r} W\left(\hat{U}_1(x,\omega)-\hat{U}_2(x,\omega)\right)}{d} \tag{B.15}$$

Since the W term occurs on both sides, we can eliminate it. Multiplying the negative sign, we get:

$$\frac{\partial^2 \hat{U}_1(x,\omega)}{\partial x^2} = \frac{\rho j\omega\varepsilon_0\varepsilon_\mathrm{r}\left(\hat{U}_{2,}(x,\omega)-\hat{U}_1(x,\omega)\right)}{Hd} \tag{B.16}$$

Conduction parameter:

$$\Gamma = \frac{j\omega\varepsilon_0\varepsilon_\mathrm{r}\rho}{Hd} \tag{B.17}$$

Substituting B.17 in B.16 yields, we get a second-order differential equation. For top track:

$$\frac{\partial^2 \hat{U}_1(x,\omega)}{\partial x^2} - \Gamma\left(\hat{U}_2(x,\omega)-\hat{U}_1(x,\omega)\right) = 0 \tag{B.18}$$

And for the bottom track, the differential equation:

$$\frac{\partial^2 \hat{U}_2(x,\omega)}{\partial x^2} - \Gamma\left(\hat{U}_1(x,\omega)-\hat{U}_2(x,\omega)\right) = 0 \tag{B.19}$$

In matrix form: $\frac{\partial^2\overrightarrow{U}}{\partial x^2} = A\overrightarrow{U}$

gives the eigenvalue problem:

$$(A-\lambda^2 I)\overrightarrow{U} = \begin{Bmatrix}\Gamma-\lambda^2 & -\Gamma \\ -\Gamma & \Gamma-\lambda^2\end{Bmatrix}\begin{Bmatrix}U_1 \\ U_2\end{Bmatrix} = 0 \tag{B.20}$$

with

$$A = \begin{Bmatrix}\Gamma & -\Gamma \\ -\Gamma & \Gamma\end{Bmatrix} \tag{B.21}$$

The coupled differential equations B.18 and B.19 can be solved as:

$$\overrightarrow{\hat{U}}_1(x,\omega) = B_{1,1}e^{\lambda_1 x} + B_{1,2}e^{\lambda_2 x} + B_{1,3}e^{\lambda_3 x} + B_{1,4}e^{\lambda_4 x} \tag{B.22}$$

$$\overrightarrow{\hat{U}}_2(x,\omega) = B_{2,1}e^{\lambda_1 x} + B_{2,2}e^{\lambda_2 x} + B_{2,3}e^{\lambda_3 x} + B_{2,4}e^{\lambda_4 x} \tag{B.23}$$

expressed as a single equation by using eigenvectors:

$$\begin{Bmatrix}\overrightarrow{\hat{U}}_1(x,\omega) \\ \overrightarrow{\hat{U}}_2(x,\omega)\end{Bmatrix} = B_1\overrightarrow{\eta_1}e^{\lambda_1 x} + B_2\overrightarrow{\eta_2}e^{\lambda_2 x} + B_3\overrightarrow{\eta_3}e^{\lambda_3 x} + B_4\overrightarrow{\eta_4}e^{\lambda_4 x} \tag{B.24}$$

Solving coefficients for the eigenvalues λ using the determinant of equation B.21:

$$\lambda_{1,2} = 0, \lambda_3 = \sqrt{2\Gamma}, \lambda =_4 -\sqrt{2\Gamma} \tag{B.25}$$

Thus, equation B.24 can be written as:

$$\overrightarrow{\hat{U}}(x,\omega) = B_1\overrightarrow{\eta_1} + B_2\overrightarrow{\eta_2}x + B_3\overrightarrow{\eta_3}e^{\sqrt{2\Gamma}x} + B_4\overrightarrow{\eta_4}e^{-\sqrt{2\Gamma}x} \tag{B.26}$$

Solving coefficients of the eigenvectors $\overrightarrow{\eta}$:

$$\begin{aligned}\overrightarrow{\eta}_1 = \overrightarrow{\eta}_2 = \begin{Bmatrix}1\\1\end{Bmatrix}\\ \overrightarrow{\eta}_3 = \overrightarrow{\eta}_4 = \begin{Bmatrix}1\\-1\end{Bmatrix}\end{aligned} \tag{B.27}$$

Results in:

$$\overrightarrow{\hat{U}}(x,\omega) = \begin{Bmatrix}\overrightarrow{\hat{U}}_1(x,\omega)\\ \overrightarrow{\hat{U}}_2(x,\omega)\end{Bmatrix} = B_1\begin{Bmatrix}1\\1\end{Bmatrix} + B_2\begin{Bmatrix}1\\1\end{Bmatrix}x + B_3\begin{Bmatrix}1\\-1\end{Bmatrix}e^{-\sqrt{2\Gamma}x} + B_4\begin{Bmatrix}1\\-1\end{Bmatrix}e^{\sqrt{2\Gamma}x} \tag{B.28}$$

The coefficient of B can be derived by using its boundary conditions. The **first boundary condition** (B.1) exists where the input voltage U_{in} is applied in the U_1 and the U_2 is ground. Thus, equation B.28 can be written as:

$$\hat{U}_1(0,\omega) = \hat{U}_{\text{in}} = B_1 + B_3 + B_4 \tag{B.29}$$

$$\hat{U}_2(0,\omega) = 0 = B_1 - B_3 - B_4 \tag{B.30}$$

Solving B.29 and B.30 gives B_1:

$$B_1 = B_3 + B_4 = B_1 = \frac{\hat{U}_{\text{in}}}{2} \tag{B.31}$$

For current taken as the boundary condition, a derivative of equation B.28:

$$\frac{\partial\overrightarrow{\hat{U}}(x,\omega)}{\partial x} = B_2\begin{Bmatrix}1\\1\end{Bmatrix} - B_3\begin{Bmatrix}1\\-1\end{Bmatrix}\sqrt{2\Gamma}e^{-\sqrt{2\Gamma}x} + B_4\begin{Bmatrix}1\\-1\end{Bmatrix}\sqrt{2\Gamma}e^{\sqrt{2\Gamma}x} \tag{B.32}$$

can be used. For current (I) passing through the length L:

$$\overrightarrow{\hat{I}}(L,\omega) = \frac{-HW}{\rho}\left(B_2\begin{Bmatrix}1\\1\end{Bmatrix} - B_3\begin{Bmatrix}1\\-1\end{Bmatrix}\sqrt{2\Gamma}e^{-\sqrt{2\Gamma}L} + B_4\begin{Bmatrix}1\\-1\end{Bmatrix}\sqrt{2\Gamma}e^{\sqrt{2\Gamma}L}\right) \tag{B.33}$$

Applying the **fourth boundary condition** (B.4), the current will be equal and opposite $\hat{I}_1(L,\omega) = -\hat{I}_2(L,\omega)$

$$\hat{I}_1(L,\omega) = \frac{HW}{\rho}\left(-B_2 + B_3\sqrt{2\Gamma}e^{-\sqrt{2\Gamma}L} - B_4\sqrt{2\Gamma}e^{\sqrt{2\Gamma}L}\right) \tag{B.34}$$

$$\hat{I}_2(L,\omega) = \frac{HW}{\rho}\left(-B_2 - B_3\sqrt{2\Gamma}e^{-\sqrt{2\Gamma}L} + B_4\sqrt{2\Gamma}e^{\sqrt{2\Gamma}L}\right) \tag{B.35}$$

Solving these gives us the coefficient B_2 as 0. The **second boundary condition** in (B.2) shows the input current at U_1 as $\hat{I}_1(0,\omega) = \hat{I}_{\text{in}}$

$$\hat{I}_{\text{in}} = \frac{HW}{\rho}\left(B_3\sqrt{2\Gamma} - B_4\sqrt{2\Gamma}\right) \tag{B.36}$$

Solving equation B.36 and B.31 yields B_3 and B_4:

$$B_4 = \frac{-2\hat{I}_{\text{in}}\rho + HW\hat{U}_{\text{in}}\sqrt{2\Gamma}}{4HW\sqrt{2\Gamma}} \tag{B.37}$$

$$B_3 = \frac{\hat{U}_{\text{in}}}{2} - B_4 = \frac{\sqrt{2}\hat{I}_{\text{in}}\rho + H\sqrt{\Gamma}\hat{U}_{\text{in}}W}{4H\sqrt{\Gamma}W} \tag{B.38}$$

Giving the output current at length L:

$$\hat{I}_{\text{out}}(L,\omega) = \frac{e^{-\sqrt{2\Gamma}L} HW \left\{2\left(1+e^{\sqrt{2\Gamma}2L}\right)\hat{I}_{\text{in}}\rho + \sqrt{2}\left(-1+e^{\sqrt{2\Gamma}2L}\right)H\sqrt{\Gamma}\hat{U}_{\text{in}}W\right\}}{4H\rho W} \tag{B.39}$$

The output voltage at length L is $\hat{U}_{\text{out1}}$ and $\hat{U}_{\text{out2}}$, given by:

$$\hat{U}_{\text{out1}} = \hat{U}_1(L,\omega) = B_1 + B_3 e^{-\sqrt{2\Gamma}L} + B_4 e^{\sqrt{2\Gamma}L} \tag{B.40}$$

$$\hat{U}_{\text{out2}} = \hat{U}_2(L,\omega) = B_1 - B_3 e^{-\sqrt{2\Gamma}L} - B_4 e^{\sqrt{2\Gamma}L} \tag{B.41}$$

Solving B.40 and B.41 we get,

$$\hat{U}_{\text{out}} = \frac{e^{-\sqrt{2\Gamma}L}\left\{-\sqrt{2}\left(-1+e^{\sqrt{2\Gamma}2L}\right)\hat{I}_{\text{in}}\rho + \left(1+e^{\sqrt{2\Gamma}2L}\right)H\Gamma\hat{U}_{\text{in}}W\right\}}{2H\Gamma W} \tag{B.42}$$

To calculate the output for input at length L of the sensor, we can use a transfer matrix A:

$$\begin{Bmatrix} U_{\text{out}} \\ I_{\text{out}} \end{Bmatrix} = \begin{Bmatrix} A_{11} & A_{12} \\ A_{21} & A_{22} \end{Bmatrix} \begin{Bmatrix} U_{\text{in}} \\ I_{\text{in}} \end{Bmatrix} \tag{B.43}$$

Solving equation B.39 and B.42, elements of matrix A are given as:

$$A_{11} = \frac{1}{2}e^{-\sqrt{2\Gamma}L}\left(1+e^{\sqrt{2\Gamma}2L}\right) \tag{B.44}$$

$$A_{12} = \frac{-e^{-\sqrt{2\Gamma}L}\left(-1+e^{\sqrt{2\Gamma}2L}\right)\rho}{\sqrt{2\Gamma}HW} \tag{B.45}$$

$$A_{21} = \frac{-e^{-\sqrt{2\Gamma}L}\left(-1+e^{2\sqrt{2\Gamma}L}\right)\sqrt{\Gamma}HW}{2\sqrt{2}\rho} \tag{B.46}$$

$$A_{22} = \frac{1}{2}e^{-\sqrt{2\Gamma}L}\left(1+e^{2\sqrt{2\Gamma}L}\right) \tag{B.47}$$

$$A = \begin{Bmatrix} \frac{1}{2}e^{-\sqrt{2\Gamma}L}\left(1+e^{\sqrt{2\Gamma}2L}\right) & \frac{-e^{-\sqrt{2\Gamma}L}\left(-1+e^{\sqrt{2\Gamma}2L}\right)\rho}{\sqrt{2\Gamma}HW} \\ \frac{-e^{-\sqrt{2\Gamma}L}\left(-1+e^{2\sqrt{2\Gamma}L}\right)\sqrt{\Gamma}HW}{2\sqrt{2}\rho} & \frac{1}{2}e^{-\sqrt{2\Gamma}L}\left(1+e^{2\sqrt{2\Gamma}L}\right) \end{Bmatrix} \tag{B.48}$$

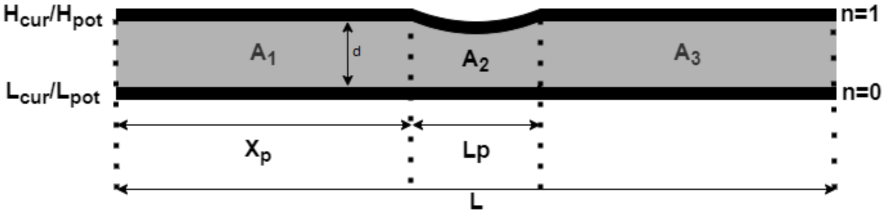

Figure B.6: Part-wise sensor definition, taken from [24].

The parallel plate sensor has length L with dielectric of height d, Figure B.6. As the sensor is probed at x_p, the parameters of the pressed part L_p will differ from the parameters of the unpressed part. This can be modelled by splitting the sensor into three respective sections with three transfer matrices A, with different parameters. This change in the parameters of the section A_2 is caused by a change in the dielectric thickness of the sensor at the probed position due to the electrode's piezoresistivity [53]:

$$\Delta h = -\frac{Fh_0}{A_0 E'} \tag{B.49}$$

Δh gives the change in thickness, F gives the applied compressive force, A_0 gives the area of the electrodes, and E' gives the effective Young's modulus for the dielectric. We assume the dielectric to have Poisson's ratio near zero as it is compressible and has low density. Thus, we ignore the change in the area of the electrode. The piezoresistivity of the electrode is the relative change in resistivity because of the applied force. It is modelled on a macroscopic level, and is calculated by using the sensitivity factor S_n:

$$\frac{\Delta\rho}{\rho} = S_n F \tag{B.50}$$

Scalar multiplication is possible on the A matrices as the outputs of sections are connected to the inputs of another section. We can thus compute the final matrix and calculate the conduction through these sections, equation B.50. The impedance can be calculated using the equation B by using this A_{final} matrix.

$$A_{\text{final}} = A_3(L - X_{\text{p}} - L_{\text{p}})A_2(L_{\text{p}})A_1(X_{\text{p}}) \tag{B.51}$$

The third boundary condition makes the impedance Z:

$$I_{\text{out}} = A_{21}U_{\text{in}} + A_{22}I_{\text{in}} = 0 \tag{B.52}$$

Defining the impedance of the sensor and the A values from the equation above, we get:

$$\begin{aligned} Z_{\text{total}} &= \frac{\hat{U}_1(0,\omega) - \hat{U}_2(0,\omega)}{\hat{I}_1(0,\omega)} \\ &= -\frac{A_{22}}{A_{21}} \\ &= \frac{\sqrt{2}\rho\left(1 + e^{2\sqrt{2\Gamma}L}\right)}{H\sqrt{\Gamma}W\left(-1 + e^{2\sqrt{2\Gamma}L}\right)} \end{aligned} \tag{B.53}$$

As the resistance and capacitance are in series, the total impedance:

$$Z_{\text{total}}(\omega) = \Re\{Z(\omega)\} + \Im\{Z(\omega)\}\, j \tag{B.54}$$

C MATLAB® Implementation of Previous Work

The model is implemented in MATLAB® code written with the help of the code by Patel [24]. Table C.1 illustrates the parameters used to simulate the model. They are modified as in the code according to the changes in the new design.

Table C.1: Sensor parameters for MATLAB implementation by Patel, [24].

Parameter name	**value**
Sensor length (L)	17.8 cm
Sensor width (W)	0.84 cm
L_{press}	1 cm
X_{press}	5 cm
Relative permittivity dielectric (ε_1)	6.33
Dielectric height (h)	600 µm
Young's modulus dielectric (E'_1)	1 MPa
Young's modulus bottom dielectric (E'_{-1})	12 MPa
Resistivity of top electrode (ρ_1)	0.07 Ω m
Resistivity of bottom electrode (ρ_0)	0.2 Ω m

The next parts are relevant work by Patel, taken from [24]. Modelling this project is implemented with the following work taken as preliminary.

C.0.1 Frequency response

Since the sensor is modelled as an RC-low-pass filter, the path of the current changes above the cut-off frequency. This leads to the current not passing through the entire sensor. It still passes through the part of the sensor that is close to the connections, and this distance the current travels is dependent on the frequency of the current. This concept birthed the idea of adding a multi-frequency approach to get better information about the position.

C.1 Inverse Model

The analytical model implemented in MATLAB® calculates the variation in impedance based on a known force and position. The objective of the project, however, is to infer the force and position from the impedance measurements. To achieve this, an inverse model is developed and proposed in this section. It provides an estimate of the force and position values from the impedance readings.

C.1.1 Estimation using $fmincon$

This new model employs straightforward equations to compute the variation in resistance and capacitance. The relationship between force and capacitance is approximated using a linear equation, and the resistance is assumed to have a linear dependence on force, to simplify the model. The association between resistance and position is also approximated using a quadratic equation. A preliminary estimation is carried out in the first instance, where the values of resistance and capacitance, as well as the changes in resistance and capacitance due to force and position, are estimated. The parameters obtained from this initial estimation are enumerated as follows:

- Estimated resistance, R_0
- Estimated capacitance, C_0

- change in capacitance due to applied force, C_F
- change in resistance due to applied force, A
- quadratic term of the position, B
- change in resistance due to change in position, D
- change in resistance due to force and position, E

The parameters are multiplied by the weight vector w_0 to determine the coefficients of the equations. The w_0 is a vector of ones, $w_0 = [1, 1, 1, 1, 1, 1, 1]$. The change in capacitance is calculated by:

$$C = C_0 + FC_\mathrm{F} \tag{C.1}$$

The change in resistance is calculated by:

$$R = R_0 + AF + Bx^2 + Dx + EFx \tag{C.2}$$

where F is the force applied and x is the position where the force is applied. The real impedance $\Re\{Z(\omega)\}$ and imaginary impedance $\Im\{Z(\omega)\}$ are calculated from the resistance and the capacitance, using that they are in series.

A cost function is defined which is the root mean square of the summation of the squared difference between the model impedance and the estimated impedance:

$$J = \sqrt{\frac{1}{m}\sum_{i=1}^{m}(\Re\{Z_\mathrm{M}\} - \Re\{Z_\mathrm{est}\})^2} + \sqrt{\frac{1}{m}\sum_{i=1}^{m}(\Im\{Z_\mathrm{M}\} - \Im\{Z_\mathrm{est}\})^2} \tag{C.3}$$

The MATLAB® function *fmincon* is used to minimize the error of this cost function by finding the optimal coefficients given by $w_\mathrm{fit} = [0.18, 0.28, 0.11, 0.23, 0, 2.96, 0.29]$. The impedance is calculated using w_fit vector. To determine position and force from the impedance an inverse function is implemented in MATLAB® by inverting equations C.2 and C.1. The applied force F is calculated using:

$$F = \frac{C - C_0}{C_\mathrm{F}} \tag{C.4}$$

and the change in position x is calculated by solving the quadratic formula $\frac{-b-\sqrt{b^2-4ac}}{2a}$, however, this formula did give values that were outside the sensor and those values were neglected:

$$x = \frac{-(D + EF) - \sqrt{-(D + EF)^2 - 4B(R_0 + AF)}}{2B} \tag{C.5}$$

The function takes impedance as the initially estimated parameter and the optimized weights and outputs the corresponding force and position values. The force is depicted as a function of $\Re\{Z(\omega)\}$ and $\Im\{Z(\omega)\}$. The plot indicates that the value of force, ranging from 3-11 N, is determined by $\Im\{Z(\omega)\}$. Similarly, the information on the position is obtained by $\Re\{Z(\omega)\}$ and is in the range of 0.01-0.09 cm taken from the actual length of the sensor.

D Multimeter results of resistance recorded on printed sensors

Table D.1: Design Iterations and Electrical Resistances.

Design	Resistance in Y	Resistance in Z	Remarks
19 sqXY	0.9k	0	
19 sqYX	1k		
20 sq 1	1.4k		
20 sq 2	600k		
20 sqXY	1.4k		
20 sqYX	1.7k		
20 sqXY 6mm	59k		not baked
20 sqYX 6mm	6.9k	70k	
21 triY	2.9k		
22 triX	2.3k / 3.8k	3.3k / 1.3k	small holes
22 sqXY	2.5k	650k	
23 triX	0.68k	45	
23 triX r	0.6k	13	
23 triX 2	0.63k	13.6	
23 triX 3	0.67k	53	
23 triX 4	0.68k	32	
23 triX .1mm	0.74k	28	
23 triX .1mm 2	0.8k	1.13k	small holes
23 triX .1mm 4	0.8k	0.27	
23 triX .2mm	0.65k	0.26k	small holes
23 triX .2mm 2	8k	39.3k	small holes, test again
23 triX .2mm 3	0.85k	40	
23 triX .2mm 4	0.8k	0.3k	small holes
23 triY	0.36k	7	
23 triY r	0.435k	16 / 24	
23 triY 2	0.5k	18	
23 triY 3	0.5k	34	
23 triY 4	0.45k	30	
23 triY .1mm	0.5k	9.2	
23 triY .1mm l	0.5k	45	
23 triY .1mm 2	0.9k	110	small holes
23 triY .1mm 3	0.9k	0.3k / 1.8k	small holes
23 triY .1mm 4	0.7k	0.7k	small holes
23 triY .1mm fine	1k	1.1k	small holes
23 triY .1mm xtrafine	0.65k	36	
23 triY .1mm xfine	75k	1.1m	not baked
23 triY .2mm x fine	0.9k	0.3k	80% infill for x60
23 triY .2mm m	38k	0.3m	
23 triY .2mm 2	0.4k	13	
23 triY .2mm 3	0.6k	65 / 130	
23 triY .2mm 4	0.5k	45	
23 sqXY	0.75k	142	
23 sqXY 2	1.2k	2k	small holes

Table D.1: Design Iterations and Electrical Resistances.

Design	Resistance in Y	Resistance in Z	Remarks
23 sqXY 3	0.8k	123	
23 sqXY 4	0.6k	60	
23 sqXY .1mm	1k	2k	
23 sqXY .1mm 2	1.4k	0.7m	
23 sqXY .1mm 3	2.5k / 3k	5k / 0	big holes
23 sqXY .1mm 4	1.1k	20k	
23 sqXY .2mm	1k	1.6k	small holes
23 sqXY .2mm 2	2.2k	5.7k	small holes
23 sqXY .2mm 3	1.3k	0.7k	big holes
23 sqXY .2mm 4	0.7k	0.6k / 0.8k	big holes
23 sqYX	0.6k	0.2k / 0.4k	small holes
23 sqYX r	1.1k	1.4k	big holes
23 sqYX 2 x fine	0.9k	1.2k	small holes
23 sqYX 3	0.7k	38	
23 sqYX 4	1k	1k	big holes
23 sqYX 0.1mm x fine	1k	1k	80% infill for x60
23 sqYX 0.1mm			
23 sqYX 0.1mm 4	0.8		
23 sqYX 0.2mm	3k		
23 sqYX 0.2mm 2	1.4k	0	
23 sqYX 0.2mm 3	1.6k / 1k	0.5k / 1k / 1.3k	
23 sqYX 0.2mm 4	4k	4k	
25 triX	0.5k / 0.8k	0.26k	
25 triY	0.4k / 0.6k	100 / 180	
25 sqXY	0.9k / 2k	0.5k / 3k	
25 sqYX	0.8k / 2.3k	8.5k / 10.5k	

Information about all the prints that came out to be usable for the experiment is added in the above table. the first two numbers in the design name is the number of design iterations. sq and tri are renditions of the rectangular shape and triangular shape. XY, YX, X and Y are the direction of the artefacts in the design. For example, XY will indicate the top layer to be having artefacts, or air gaps and cogs of the top electrode, that are in the X direction and the bottom layer to be having artefacts that are in the Y direction. The . 'number' mm is the height of the dielectric layer without artefacts that are added between the electrodes. The absence of this segment indicates no layer of dielectric without such artefacts. 'fine' denotes the slicing of the sensor assembly to be done under the setting of fine, which slices each part to 0.1 mm. 'x fine', 'x fine', and 'xtrafine' indicate the slicing software setting to be set to extrafine, which slices each part to 0.06 mm.

Bibliography

[1] J. Yang, J. Mun, S. Kwon, S. Park, Z. Bao, and S. Park, “Electronic skin: Electronic skin: Recent progress and future prospects for skin-attachable devices for health monitoring, robotics, and prosthetics (adv. mater. 48/2019),” *Advanced Materials*, vol. 31, 11 2019.

[2] J. Heikenfeld, A. Jajack, J. Rogers, P. Gutruf, L. Tian, T. Pan, R. Li, M. Khine, J. Kim, J. Wang, and J. Kim, “Wearable sensors: modalities, challenges, and prospects,” *Lab Chip*, vol. 18, pp. 217–248, 2018.

[3] D. J. Lipomi, M. Vosgueritchian, B. C. K. Tee, S. L. Hellstrom, J. A. Lee, C. H. Fox, and Z. Bao, “Skin-like pressure and strain sensors based on transparent elastic films of carbon nanotubes,” *Nature nanotechnology*, vol. 6 12, pp. 788–92, 2011.

[4] R. Li, Q. Zhou, Y. Bi, S. Cao, X. Xia, A. Yang, S. Li, and X. Xiao, “Research progress of flexible capacitive pressure sensor for sensitivity enhancement approaches,” *Sensors and Actuators A: Physical*, vol. 321, p. 112425, 2021.

[5] W.-H. Yeo, Y.-S. Kim, J. Lee, A. Ameen, L. Shi, M. Li, S. Wang, R. Ma, S. H. Jin, Z. Kang, Y. Huang, and J. A. Rogers, “Multifunctional epidermal electronics printed directly onto the skin,” *Advanced Materials*, vol. 25, no. 20, pp. 2773–2778, 2013.

[6] D.-H. Kim, N. Lu, R. Ma, Y.-S. Kim, R.-H. Kim, S. Wang, J. Wu, S. M. Won, H. Tao, A. Islam, K. J. Yu, T. il Kim, R. Chowdhury, M. Ying, L. Xu, M. Li, H.-J. Chung, H. Keum, M. McCormick, P. Liu, Y.-W. Zhang, F. G. Omenetto, Y. Huang, T. Coleman, and J. A. Rogers, “Epidermal electronics,” *Science*, vol. 333, no. 6044, pp. 838–843, 2011.

[7] K. Sanderson, “Electronic skin: from flexibility to a sense of touch,” *Nature*, vol. 591, pp. 685–687, 2021.

[8] J. A. Rogers, T. Someya, and Y. Huang, “Materials and mechanics for stretchable electronics,” *Science*, vol. 327, no. 5973, pp. 1603–1607, 2010.

[9] T. Someya, T. Sekitani, S. Iba, Y. Kato, H. Kawaguchi, and T. Sakurai, “A large-area, flexible pressure sensor matrix with organic field-effect transistors for artificial skin applications,” *Proceedings of the National Academy of Sciences*, vol. 101, no. 27, pp. 9966–9970, 2004.

[10] D.-Y. Khang, H. Jiang, Y. Huang, and J. A. Rogers, “A stretchable form of single-crystal silicon for high-performance electronics on rubber substrates,” *Science*, vol. 311, no. 5758, pp. 208–212, 2006.

[11] M. L. Hammock, A. Chortos, B. C.-K. Tee, J. B.-H. Tok, and Z. Bao, “25th anniversary article: the evolution of electronic skin (e-skin): a brief history, design considerations, and recent progress,” *Advanced materials*, vol. 25, no. 42, pp. 5997–6038, 2013.

[12] G. Buchberger, R. Schwodiauer, N. Arnold, and S. Bauer, “Cellular ferroelectrets for flexible touchpads, keyboards and tactile sensors,” *2008 IEEE Sensors*, pp. 1520–1523, 2008.

[13] S. Rosset, M. Niklaus, P. Dubois, and H. R. Shea, “Metal ion implantation for the fabrication of stretchable electrodes on elastomers,” *Advanced Functional Materials*, vol. 19, no. 3, pp. 470–478, 2009.

[14] S. Rosset and H. R. Shea, “Flexible and stretchable electrodes for dielectric elastomer actuators,” *Applied Physics A*, vol. 110, no. 2, pp. 281–307, 2013.

[15] J. Ulmen and M. R. Cutkosky, “A robust, low-cost and low-noise artificial skin for human-friendly robots,” *2010 IEEE International Conference on Robotics and Automation*, pp. 4836–4841, 2010.

[16] D. P. Cotton, I. M. Graz, and S. P. Lacour, “A multifunctional capacitive sensor for stretchable electronic skins,” *IEEE Sensors Journal*, vol. 9, no. 12, pp. 2008–2009, 2009.

[17] X. Zhao, Q. Hua, R. Yu, Y. Zhang, and C. Pan, “Flexible, stretchable and wearable multifunctional sensor array as artificial electronic skin for static and dynamic strain mapping,” *Advanced Electronic Materials*, vol. 1, no. 7, p. 1500142, 2015.

[18] Y. Khan, A. E. Ostfeld, C. M. Lochner, A. Pierre, and A. C. Arias, “Monitoring of vital signs with flexible and wearable medical devices,” *Advanced Materials*, vol. 28, no. 22, pp. 4373–4395, 2016.

[19] W. Hao, J. Guo, C. Wang, S. Wang, and C. Shi, “A novel capacitive-based flexible pressure sensor based on stretchable composite electrodes and a dielectric elastomer with microstructures,” *IEEE Access*, vol. 8, pp. 142810–142818, 2020.

[20] C. Liu, N. Huang, F. Xu, J. Tong, Z. Chen, X. Gui, Y. Fu, and C. Lao, “3d printing technologies for flexible tactile sensors toward wearable electronics and electronic skin,” *Polymers*, vol. 10, no. 6, p. 629, 2018.

[21] M. Schouten, “3d printed sensors and bio-electronics for robotic applications,” phd thesis, University of Twente, Enschede, The Netherlands, 2023.

[22] D. P. Industry, “3d printing basics: Free beginner’s guide,” 2023. Accessed: 2023-07-15.

[23] top3dshop, 2020. Available at "`https://top3dshop.com/blog/fff-vs-fdm-difference-and-best-printers`".

[24] P. Patel, “3d printed differential force and position sensor based on lossy transmission lines,” msc. thesis, University of Twente, Enschede, The Netherlands, 2021.

[25] S. C. Altıparmak, V. A. Yardley, Z. Shi, and J. Lin, “Extrusion-based additive manufacturing technologies: State of the art and future perspectives,” *Journal of Manufacturing Processes*, vol. 83, pp. 607–636, 2022. https://www.sciencedirect.com/science/article/pii/S1526612522006521.

[26] X. Yu, B. K. Mahajan, W. Shou, and H. Pan, “Materials, mechanics, and patterning techniques for elastomer-based stretchable conductors,” *Micromachines*, vol. 8, no. 1, p. 7, 2016.

[27] M. R. Khosravani and T. Reinicke, “3d-printed sensors: Current progress and future challenges,” *Sensors and Actuators A: Physical*, vol. 305, p. 111916, 2020.

[28] T. Distler and A. R. Boccaccini, “3d printing of electrically conductive hydrogels for tissue engineering and biosensors – a review,” *Acta Biomaterialia*, vol. 101, pp. 1–13, 2020.

[29] B. Zhang, S. Li, H. Hingorani, A. Serjouei, L. Larush, A. A. Pawar, W. H. Goh, A. H. Sakhaei, M. Hashimoto, K. Kowsari, S. Magdassi, and Q. Ge, “Highly stretchable hydrogels for uv curing based high-resolution multimaterial 3d printing,” *J. Mater. Chem. B*, vol. 6, pp. 3246–3253, 2018.

[30] K. Tian, J. Bae, S. E. Bakarich, C. Yang, R. D. Gately, G. M. Spinks, M. in het Panhuis, Z. Suo, and J. J. Vlassak, “3d printing of transparent and conductive heterogeneous hydrogel–elastomer systems,” *Advanced Materials*, vol. 29, no. 10, p. 1604827, 2017.

[31] A. Haines. Available at "`http://www.agihaines.com/`.

[32] S. Printed. Available at "`http://ddw.nl/en/programme/7821/laced`".

[33] D. Shorey. Available at "`https://www.shoreydesigns.com/`".

[34] C. Lou, S. Wang, T. Liang, C. Pang, L. Huang, M. Run, and X. Liu, "A graphene-based flexible pressure sensor with applications to plantar pressure measurement and gait analysis," *Materials*, vol. 10, no. 9, p. 1068, 2017.

[35] Z. Aloqalaa, "Electrically conductive fused deposition modeling filaments: Current status and medical applications," *Crystals*, vol. 12, no. 8, 2022.

[36] W. Jia, Q. Zhang, Y. Cheng, J. Wang, H. Zhang, S. Sang, and J. Ji, "A flexible capacitive paper-based pressure sensor fabricated using 3d printing," *Chemosensors*, vol. 10, no. 10, 2022.

[37] Tekscan, "Tekscan," 2023. Available at "`http://www.tekscan.com/`".

[38] V. Lugade and K. Kaufman, "Dynamic stability margin using a marker based system and tekscan: A comparison of four gait conditions," *Gait & Posture*, vol. 40, no. 1, pp. 252–254, 2014.

[39] Tekscan, "Plantar pressure analysis: Research to frontline clinical practice," 2023. Available at "`http://www.tekscan.com/resources/on-demand-webinar/plantar-pressure-analysis-research-frontline-clinical-practice`".

[40] M. J. Hessert, M. Vyas, J. Leach, K. Hu, L. A. Lipsitz, and V. Novak, "Foot pressure distribution during walking in young and old adults," *BMC geriatrics*, vol. 5, no. 1, pp. 1–8, 2005.

[41] C. Bark, K. Chaccour, R. Darazi, A. H. El Hassani, and E. Andres, "Design and development of a force-sensing shoe for gait analysis and monitoring," in *2017 Fourth International Conference on Advances in Biomedical Engineering (ICABME)*, pp. 1–4, IEEE, 2017.

[42] B. MacWilliams and P. Armstrong, "Clinical applications of plantar pressure measurement in pediatric orthopedics," in *Pediatric gait: a new millennium in clinical care and motion analysis technology*, pp. 143–150, IEEE, 2000.

[43] D. Rosenbaum and H.-P. BECKER, "Plantar pressure distribution measurements. technical background and clinical applications," *Foot and ankle surgery*, vol. 3, no. 1, pp. 1–14, 1997.

[44] E. Westphal, H.-D. Carl, S. Krinner, C. Grim, B. Swoboda, and T. Hotfiel, "Plantar force deviations in dynamic pedobarography–the role of insole and platform based systems as influencing factors," *Sports Orthopaedics and Traumatology*, vol. 32, no. 4, pp. 380–386, 2016.

[45] K. N. Bachus, A. L. DeMarco, K. T. Judd, D. S. Horwitz, and D. S. Brodke, "Measuring contact area, force, and pressure for bioengineering applications: Using fuji film and tekscan systems," *Medical Engineering & Physics*, vol. 28, no. 5, pp. 483–488, 2006.

[46] P. R. Cavanagh and M. Ae, "A technique for the display of pressure distributions beneath the foot," *Journal of biomechanics*, vol. 13, no. 2, pp. 69–75, 1980.

[47] C. Price, D. Parker, and C. Neser, "Validity and repeatability of three in-shoe pressure measurement systems," *Gait & Posture*, vol. 46, pp. 69–74, 2016.

[48] A. H. A. Razak, A. Zayegh, R. K. Begg, and Y. Wahab, “Foot plantar pressure measurement system: A review,” *Sensors*, vol. 12, no. 7, pp. 9884–9912, 2012.

[49] C. Giacomozzi, N. Keijsers, T. Pataky, and D. Rosenbaum, “International scientific consensus on medical plantar pressure measurement devices: technical requirements and performance,” *Annali dell’Istituto superiore di sanita*, vol. 48, pp. 259–271, 2012.

[50] M. Mashagbeh, H. Alzaben, R. Abutair, R. Farrag, L. Sarhan, and M. Alyaman, “Gait cycle monitoring system based on flexiforce sensors,” *Inventions*, vol. 7, p. 51, 06 2022.

[51] L. Shu, T. Hua, Y. Wang, Q. Li, D. D. F. Feng, and X. Tao, “In-shoe plantar pressure measurement and analysis system based on fabric pressure sensing array,” *IEEE transactions on information technology in biomedicine: a publication of the IEEE Engineering in Medicine and Biology Society*, vol. 14, pp. 767–75, 05 2010.

[52] J. Chen, Y. Zhao, J. Lin, Y. Dai, B. Hu, and S. Gao, “A flexible insole gait monitoring technique for the internet of health things,” *IEEE Sensors Journal*, vol. 21, no. 23, pp. 26397–26405, 2021.

[53] M. Schouten, R. Sanders, and G. Krijnen, “3d printed flexible capacitive force sensor with a simple micro-controller based readout,” in *2017 IEEE SENSORS*, pp. 1–3, 2017.

[54] M. Schouten, P. Patel, R. Sanders, and G. Krijnen, “3d printed differential force and position senionisor based on lossy transmission lines,” in *2021 21st International Conference on Solid-State Sensors, Actuators and Microsystems (Transducers)*, pp. 1460–1463, 2021.

[55] G. Wolterink, R. Sanders, and G. Krijnen, “Thin, flexible, capacitive force sensors based on anisotropy in 3d-printed structures,” in *2018 IEEE SENSORS*, pp. 1–4, 2018.

[56] J. Qin, L.-J. Yin, Y. Hao, S.-L. Zhong, D. li Zhang, K. Bi, Y.-X. Zhang, Y. Zhao, and Z. Dang, “Flexible and stretchable capacitive sensors with different microstructures,” *Advanced Materials*, vol. 33, 2021.

[57] S. R. A. Ruth, V. R. Feig, H. Tran, and Z. Bao, “Microengineering pressure sensor active layers for improved performance,” *Advanced Functional Materials*, vol. 30, no. 39, p. 2003491, 2020.

[58] S. R. A. Ruth, L. Beker, H. Tran, V. R. Feig, N. Matsuhisa, and Z. Bao, “Rational design of capacitive pressure sensors based on pyramidal microstructures for specialized monitoring of biosignals,” *Advanced Functional Materials*, vol. 30, no. 29, p. 1903100, 2020.

[59] M. Li, J. Liang, X. Wang, and M. Zhang, “Ultra-sensitive flexible pressure sensor based on microstructured electrode,” *Sensors*, vol. 20, no. 2, 2020.

[60] S. H. Cho, S. W. Lee, S. Yu, H. Kim, S. Chang, D. Kang, I. Hwang, H. S. Kang, B. Jeong, E. H. Kim, S. M. Cho, K. L. Kim, H. Lee, W. Shim, and C. Park, “Micropatterned pyramidal ionic gels for sensing broad-range pressures with high sensitivity,” *ACS Applied Materials & Interfaces*, vol. 9, no. 11, pp. 10128–10135, 2017. PMID: 28244722.

[61] Y. Zhang, S. Liu, Y. Miao, H. Yang, X. Chen, X. Xiao, Z. Jiang, X. Chen, B. Nie, and J. Liu, “Highly stretchable and sensitive pressure sensor array based on icicle-shaped liquid metal film electrodes,” *ACS Applied Materials & Interfaces*, vol. 12, no. 25, pp. 27961–27970, 2020. PMID: 32498505.

[62] Z. Guo, L. Mo, Y. Ding, Q. Zhang, X. Meng, Z. Wu, Y. Chen, M. Cao, W. Wang, and L. Li, “Printed and flexible capacitive pressure sensor with carbon nanotubes based composite dielectric layer,” *Micromachines*, vol. 10, no. 11, 2019.

[63] C.-L. Choong, M.-B. Shim, B.-S. Lee, S. Jeon, D.-S. Ko, T.-H. Kang, J. Bae, S. H. Lee, K.-E. Byun, J. Im, Y. J. Jeong, C. E. Park, J.-J. Park, and U.-I. Chung, "Highly stretchable resistive pressure sensors using a conductive elastomeric composite on a micropyramid array," *Advanced Materials*, vol. 26, no. 21, pp. 3451–3458, 2014.

[64] Y. Luo, J. Shao, S. Chen, X. Chen, H. Tian, X. Li, L. Wang, D. Wang, and B. Lu, "Flexible capacitive pressure sensor enhanced by tilted micropillar arrays," *ACS Applied Materials & Interfaces*, vol. 11, no. 19, pp. 17796–17803, 2019.

[65] S. Mannsfeld, B. Tee, R. Stoltenberg, C. Chen, S. Barman, B. Muir, A. Sokolov, and Z. Bao, "Highly sensitive flexible pressure sensors with microstructured rubber dielectric layers," *Nature Materials*, vol. 9, p. 859–864, 2010.

[66] B. C.-K. Tee, A. Chortos, R. R. Dunn, G. Schwartz, E. Eason, and Z. Bao, "Tunable flexible pressure sensors using microstructured elastomer geometries for intuitive electronics," *Advanced Functional Materials*, vol. 24, no. 34, pp. 5427–5434, 2014.

[67] Y. Xiong, Y. Shen, L. Tian, Y. Hu, P. Zhu, R. Sun, and C.-P. Wong, "A flexible, ultra-highly sensitive and stable capacitive pressure sensor with convex microarrays for motion and health monitoring," *Nano Energy*, vol. 70, p. 104436, 2020.

[68] G. Schwartz, B. C.-K. Tee, J. Mei, A. L. Appleton, D. H. Kim, H. Wang, and Z. Bao, "Flexible polymer transistors with high pressure sensitivity for application in electronic skin and health monitoring," *Nature communications*, vol. 4, no. 1, pp. 1–8, 2013.

[69] S.-W. Kim, G.-Y. Oh, K.-I. Lee, Y.-J. Yang, J.-B. Ko, Y.-W. Kim, and Y.-S. Hong, "A highly sensitive and flexible capacitive pressure sensor based on alignment airgap dielectric," *Sensors*, vol. 22, no. 19, 2022.

[70] G. Stano, F. Bottiglione, and G. Percoco, "Fused filament fabrication for one shot additive manufacturing of capacitive force sensors," *Procedia CIRP*, vol. 110, pp. 168–173, 2022. V CIRP Conference on BioManufacturing.

[71] D. Kwon, T.-I. Lee, J. Shim, S. Ryu, M. S. Kim, S. Kim, T.-S. Kim, and I. Park, "Highly sensitive, flexible, and wearable pressure sensor based on a giant piezocapacitive effect of three-dimensional microporous elastomeric dielectric layer," *ACS Applied Materials & Interfaces*, vol. 8, no. 26, pp. 16922–16931, 2016. PMID: 27286001.

[72] D. Xu, A. Tairych, and I. A. Anderson, "Where the rubber meets the hand: Unlocking the sensing potential of dielectric elastomers," *Journal of Polymer Science Part B: Polymer Physics*, vol. 54, no. 4, pp. 465–472, 2016.

[73] A. Tairych and I. A. Anderson, "A variable R-C transmission line model for resistive stretch sensors," in *Electroactive Polymer Actuators and Devices (EAPAD) XX* (Y. Bar-Cohen, ed.), vol. 10594, p. 105941L, International Society for Optics and Photonics, SPIE, 2018.

[74] C. Graf and J. Maas, "A model of the electrodynamic field distribution for optimized electrode design for dielectric electroactive polymer transducers," *Smart Materials and Structures*, vol. 21, p. 094001, aug 2012.

[75] P. Sommer-Larsen, J. C. Hooker, G. Kofod, K. West, M. Benslimane, and P. Gravesen, "Response of dielectric elastomer actuators," in *Smart Structures and Materials 2001: Electroactive Polymer Actuators and Devices* (Y. Bar-Cohen, ed.), vol. 4329, pp. 157 – 163, International Society for Optics and Photonics, SPIE, 2001.

[76] K. Jung, K. J. Kim, and H. R. Choi, "A self-sensing dielectric elastomer actuator," *Sensors and Actuators A: Physical*, vol. 143, no. 2, pp. 343–351, 2008.

[77] D. Xu, S. Michel, T. McKay, B. O'Brien, T. Gisby, and I. Anderson, "Sensing frequency design for capacitance feedback of dielectric elastomers," *Sensors and Actuators A: Physical*, vol. 232, pp. 195–201, 2015.

[78] D. Xu, A. Tairych, and I. A. Anderson, "Stretch not flex: programmable rubber keyboard," *Smart Materials and Structures*, vol. 25, no. 1, p. 015012, 2015.

[79] M. Schouten, "Towards additively manufactured complex robotic systems," msc. thesis, University of Twente, Enschede, The Netherlands, 2017.

[80] M. Wehner, R. L. Truby, D. J. Fitzgerald, B. Mosadegh, G. M. Whitesides, J. A. Lewis, and R. J. Wood, "An integrated design and fabrication strategy for entirely soft, autonomous robots," *Nature*, vol. 536, no. 7617, pp. 451–455, 2016.

[81] J. Morrow, B. Shin, B. Phillips, T. Wegter, L. Stirling, and R. F. Shepherd, "Printable pneumatics: soft sensors and actuators for robotic systems," *Soft Robotics*, vol. 3, no. 1, pp. 23–33, 2016.

[82] N. W. Bartlett, M. T. Tolley, J. T. Overvelde, J. C. Weaver, B. Mosadegh, K. Bertoldi, G. M. Whitesides, and R. J. Wood, "A 3d-printed, functionally graded soft robot powered by combustion," *Science*, vol. 349, no. 6244, pp. 161–165, 2015.

[83] J. Hiller and H. Lipson, "Design and analysis of digital materials for physical 3d voxel printing," *Rapid Prototyping Journal*, vol. 15, no. 2, pp. 137–149, 2009.

[84] R. L. Truby, M. Wehner, A. K. Grosskopf, D. M. Vogt, S. G. Uzel, R. J. Wood, and J. A. Lewis, "Soft robotics: bioinspired soft robots for fluid manipulation," *Advanced Materials*, vol. 28, no. 19, pp. 3672–3677, 2016.

[85] M. Somireddy, C. V. Singh, and A. Czekanski, "Development of constitutive material model of 3d printed structure via fdm," *Materials Today Communications*, vol. 15, pp. 143–152, 2018.

[86] I. Raguž, M. Berer, M. Fleisch, C. Holzer, J. Brancart, B. Vanderborght, and S. Schlögl, "Soft dielectric actuator produced by multi-material fused filament fabrication 3d printing," *Polymers for Advanced Technologies*, vol. 34, no. 6, pp. 1967–1978, 2023.

[87] Autodesk, "Autodesk inventor," 2023. Accessed: 2023-07-15.

[88] Dassault Systèmes, "Solidworks," 2023. Accessed: 2023-07-15.

[89] M. Schouten, "diabase_cura_post_processor." Available at "`https://github.com/martijnschouten/diabase_cura_post_processor`".

[90] Diabase Engineering, "Flexion extruder." Available at "`https://www.diabasemachines.com/flexion-how-it-works`".

[91] Palmiga Innovation, "85-700+ pi-etpu filament datasheet." `https://palmiga.com/`.

[92] Makeshaper and Diabase, "X60." Availabkle at "`https://3dprint.com/167731/diabase-engineering-x60/`".

[93] Hubs, "How do you design snap-fit joints for 3d printing?." Available at "`https://www.hubs.com/knowledge-base/how-design-snap-fit-joints-3d-printing/`".

[94] Hubs, “How to design interlocking joints for fastening 3d printed parts.” Available at "https://www.hubs.com/knowledge-base/how-design-interlocking-joints-fastening-3d-printed-parts/".

[95] Fiberology, “Bvoh.” Available at "https://fiberlogy.com/en/fiberlogy-filaments/bvoh/".

[96] Simplify3d, “Pva.” Available at "https://www.simplify3d.com/resources/materials-guide/pva/".

[97] BCN3D, “Bvoh v/s pva.” Available at "https://support.bcn3d.com/knowledge/bvoh-vs-pva".

[98] Palmiga Innovation, “Pi-etpu85-700+ carbon black.”

[99] Diabase Engineering, “X60.” Available at "https://flexionextruder.com/shop/x60-ultra-flexible-filament-natural/".

[100] 3D Insider, “Everything you need to know about 3d printing extrusion multiplier,” 2024. Accessed: 2024-07-25.

[101] C. C. Vu, T. T. Nguyen, S. Kim, and J. Kim, “Effects of 3d printing-line directions for stretchable sensor performances,” *Materials*, vol. 14, no. 7, p. 1791, 2021.

[102] Flashforge 3D printer. Available at "https://www.flashforge.com/product-detail/flashforge-creator-pro-3d-printer".

[103] Kickstarter, “Rova3d : The first 5 material/color liquid cooled 3d printer.” Available at ":https://www.kickstarter.com/projects/ordsolutions/rova3d-the-first-5-material-color-liquid-cooled-3d".

[104] Duet3D. Available at "https://www.duet3d.com/".

[105] SMAC, “Linear_actuation_setup.” Available at "https://www.smac-mca.com/lca-series-p-15.html".

[106] E. Dumitru and M. O. Popescu, “Methods of reducing capacitive coupling between five conductors located on a pcb,” in *2013 4th International Youth Conference on Energy (IYCE)*, pp. 1–5, 2013.

[107] ForgeLabs, “agilus30.” Available at "https://forgelabs.ca/agilus-30/".

[108] ForgeLabs, “veroclear.” Available at "https://forgelabs.ca/veroclear/".

[109] Protopasta, “Conductive pla.” Available at "https://www.proto-pasta.com/collections/all/products/conductive-pla".

[110] NinjaTek, “Ninjaflex.” Available at "https://ninjatek.com/ninjaflex/".

[111] TiePie, “The unbeatable usb oscilloscope.” Available at "https://www.tiepie.com/en/usb-oscilloscope/handyscope-hs5".

[112] All3DP, “Understanding common 3d printing problems,” 2024. [Accessed: 18-Jul-2024].

[113] All3DP, “Best Flexible Filament Brands of 2024 (TPU, TPE, TPC).” https://all3dp.com/1/flexible-filament-tpu-tpe-tpc-best-brands/, 2024. [Online; accessed 13-August-2024].

[114] BCN3D, “How to solve print quality issues.” Available at "`https://support.bcn3d.com/knowledge/solve-quality-issues`".

[115] BCN3D, “How to fix underextrusion.” Available at "`https://support.bcn3d.com/knowledge/underextrusion`".

[116] T. Hullette, “3d printer under-extrusion: 8 simple solutions.” `https://all3dp.com/2/under-extrusion-3d-printing-all-you-need-to-know/`, 2023. Accessed: 2024-08-20.

[117] G. Stano, A. D. Nisio, A. M. Lanzolla, M. Ragolia, and G. Percoco, “A digital twin for the assessment and optimization of battery pack design,” *The International Journal of Advanced Manufacturing Technology*, vol. 110, no. 9-10, pp. 2587–2602, 2020.

[118] BCN3D, “Printing issues related to filament affected by humidity.” Available at "`https://support.bcn3d.com/knowledge/humid-filament-bcn3d`".

[119] G. Murugesan, “How to dry petg, pc, tpu, nylon, abs, pla filament like an expert.” Available at "`https://electroloom.com/how-to-dry-filaments-petg-pc-tpu-nylon-abs-pla/`".

[120] C. Tools, “Palmiga - pi-etpu 95-250 carbon black - 1.75 mm.” Available at "`https://www.creativetools.se/hardware/3d-printers-and-accessories/filaments/flexible-filaments/pi-etpu-95-250-carbon-black`".

[121] J. Hertz, “New technique enables intermixing materials in sla 3d printing.” `https://3dprint.com/301106/new-technique-enables-intermixing-materials-in-sla-3d-printing/`, 2024. Accessed: 2024-08-24.

[122] R. Ltd., “Multi-material sla 3d printing.” `https://rerapltd.com/multi-material-sla-3d-printing/`, 2024. Accessed: 2024-08-24.

[123] Sinterit, “Multi-material with sls 3d printer.” `https://sinterit.com/blog/sls-technology/multi-material-with-sls-3d-printer/`, 2024. Accessed: 2024-08-24.

[124] All3DP, “The unbeatable usb oscilloscope.” Available at "`https://all3dp.com/1/types-of-3d-printers-3d-printing-technology`".

[125] All3DP, “Types of 3D Printers: The Complete Guide (2024).” `https://all3dp.com/1/types-of-3d-printers-3d-printing-technology/#section-micro-3d-printing`, 2024. [Online; accessed 13-August-2024].

[126] S.-J. Woo, J.-H. Kong, D.-G. Kim, and J.-M. Kim, “A thin all-elastomeric capacitive pressure sensor array based on micro-contact printed elastic conductors,” *J. Mater. Chem. C*, vol. 2, pp. 4415–4422, 2014.

[127] Y. Zhu, T. Giffney, and K. Aw, “A dielectric elastomer-based multimodal capacitive sensor,” *Sensors*, vol. 22, no. 2, p. 622, 2022.

[128] S. Yao and Y. Zhu, “Wearable multifunctional sensors using printed stretchable conductors made of silver nanowires,” *Nanoscale*, vol. 6, no. 4, pp. 2345–2352, 2014.

[129] Z. Luo, J. Chen, Z. Zhu, L. Li, Y. Su, W. Tang, O. M. Omisore, L. Wang, and H. Li, “High-resolution and high-sensitivity flexible capacitive pressure sensors enhanced by a transferable electrode array and a micropillar–pvdf film,” *ACS Applied Materials & Interfaces*, vol. 13, no. 6, pp. 7635–7649, 2021. PMID: 33539065.

[130] R. Munroe, "XKCD 2708." `https://xkcd.com/2708`. [Online; sorry, enjoy].

[131] A. Dijkshoorn, P. Werkman, M. Welleweerd, G. Wolterink, B. Eijking, J. Delamare, R. Sanders, and G. Krijnen, "Embedded sensing: Integrating sensors in 3-d printed structures," *Journal of Sensors and Sensor Systems*, vol. 7, pp. 169–181, 03 2018.